7-1-2011

A Thermally actuated microelectromechanical (MEMS) device for measuring viscosity

Ivan Puchades

A THERMALLY ACTUATED MICROELECTROMECHANICAL (MEMS) DEVICE FOR MEASURING VISCOSITY

by

Ivan Puchades

A DISSERTATION

Submitted in partial fulfillment of the requirements
For the degree of Doctor of Philosophy
in
Microsystems Engineering
at the
Rochester Institute of Technology

July 2011

Author:_____
Microsystems Engineering Program

Certified by:_____
Lynn F. Fuller
Professor of Electrical and Microelectronic Engineering

Approved by:_____
Bruce W. Smith
Director of Microsystems Engineering Program

Certified by: _____
Harvey J. Palmer
Dean Kate Gleason College of Engineering

NOTICE OF COPYRIGHT

REPRODUCTION PERMISSION STATEMENT

Permission Granted

TITLE: "A Thermally Actuated Microelectromechanical (MEMS) Device for Measuring Viscosity"

I, *Ivan Puchades*, hereby grant permission to the Wallace Library of the Rochester Institute of Technology to reproduce my dissertation in whole or in part. Any reproduction will not be for commercial use or profit.

Signature of Author: _____ Date:_____

A Thermally Actuated Microelectromechanical (MEMS) Device for Measuring Viscosity

By

Ivan Puchades

Submitted by Ivan Puchades in partial fulfillment of the requirements for the degree of Doctor of Philosophy in Microsystems Engineering and accepted on behalf of the Rochester Institute of Technology by the dissertation committee.

We, the undersigned members of the Faculty of the Rochester Institute of Technology, certify that we have advised and/or supervised the candidate on the work described in this dissertation. We further certify that we have reviewed the dissertation manuscript and approve it in partial fulfillment of the requirements of the degree of Doctor of Philosophy in Microsystems Engineering.

Approved by:

Dr. Robert Pearson _____
(Committee Chair) Date

Dr. Lynn F.Fuller _____
(Dissertation Advisor)

Dr. David Borkholder _____

Dr. Sergey E. Lyshevski _____

Dr. Risa Robinson _____

MICROSYSTEMS ENGINEERING PROGRAM
ROCHESTER INSTITUTE OF TECHNOLOGY
July 2011

ABSTRACT

Kate Gleason College of Engineering
Rochester Institute of Technology

Degree Doctor of Philosophy **Program** Microsystems Engineering

Name of Candidate : Ivan Puchades

Title : A Thermally Actuated Microelectromechanical (MEMS) Device for Measuring Viscosity

A thermally actuated non-cantilever-beam micro-electro-mechanical viscosity sensor is presented. The proposed device is based on thermally induced vibrations of a silicon-based membrane and its damping due to the surrounding fluid. This vibration viscometer device utilizes thermal actuation through an in-situ resistive heater and piezoresistive sensing, both of which utilize CMOS compatible materials leading to an inexpensive and reliable system. Due to the nature of the actuation, thermal analysis was performed utilizing PN diodes embedded in the silicon membrane to monitor its temperature. This analysis determined the minimum heater voltage pulse amplitude and time in order to prevent heat loss to the oil under test that would lead to local viscosity changes. In order to study the natural vibration behavior of the complex multilayer membrane that is needed for the proposed sensor, a designed experiment was carried out. In this experiment, the effects of the material composition of the membrane and the size of the actuation heater were studied in detail with respect to their effects on the natural frequency of vibration. To confirm the validity of these measurements, Finite Element Analysis and white-light interferometry were utilized. Further characterization of the natural frequency of vibration of the membranes was carried out at elevated temperatures to explore the effects of temperature. Complex interactions take place among the different layers that compose the membrane structures. Finally, viscosity measurements were performed and compared to standard calibrated oils as well as to motor oils measured on a commercial cone-and-plate viscometer. The experimentally obtained data is compared to theoretical predictions and an empirically-derived model to predict viscosity from vibration measurements is proposed. Frequency correlation to viscosity was shown to be the best indicator for the range of viscosities tested with lower error (+/- 5%), than that of quality factor (+/- 20%). Further viscosity measurements were taken at elevated temperatures and over long periods of time to explore the device reliability and drift. Finally, further size reduction of the device was explored.

Abstract Approval: Committee Chair _____

Program Director _____

Dean KGCOE _____

ACKNOWLEDGMENTS

I would like to thank the following people for their support and guidance:

My wife Chelse and our children; Claire and Lucas. While I learned about microsystems and microelectronics, Chelse has established a successful photography business of which I'm very proud of. Claire is now 6 years old and Lucas was born at the mid-point of my studies. Both of them have learned so many more things than I have during these 6 years! It has always been great to come home to a happy and rambunctious bunch.

My parents Juan y Mónica and my brother Jason.

Dr. Lynn Fuller, my advisor and mentor for many years. Thank you for giving me the freedom to explore many subjects and supporting me during all these years.

I would also like to thank the faculty and staff in the Microelectronic Engineering department for their advice and help and the SMFL staff, for keeping the lab running.

My fellow students in both the Microsystems Engineering and Microelectronic Engineering department who have helped me keep in track: Vee-Chee, Gianni, Burak, Marie, Dave, Dean, Germain, Rob, Archana, Karthik, Sankha, Dan, Murat, Jakob, Heidi, Ellen, Mark, Sphend and others.

The micro-nano-bio systems group at the Centre Nacional de Microelectronica in Barcelona. Especialment gracies a en Paco-Xavi i en Roger!

Finally, the sensor group at Impact Technologies deserves recognition for providing me with standard viscosity samples and also performing calibration measurements.

TABLE OF CONTENTS

LIST OF TABLES

LIST OF FIGURES

Chapter 1.

INTRODUCTION

In the fields of rheology (study of the flow of matter) and tribiology (study and application of the principles of friction, lubrication and wear), viscosity is one of the most important factors used to characterize fluid properties. In the automotive industry oil is used as an engine lubricant and it is imperative that the integrity of the oil is kept within a specific range to provide the needed functionality. Viscosity is defined as the resistance of a fluid to flow. The higher the viscosity, the more resistance the liquid creates and the harder the engine has to work, which leads to an increase in temperature, lower fuel economy and eventually premature engine breakdown. If the oil is too thin, it will not provide enough protection and will allow contact between the moving parts leading to engine wear out. Among other parameters, such as acidity, water content and soot content, viscosity must be monitored as the lubricating oil degrades over its lifetime of storage or use. The main causes of this degradation are typically oxidation, hydrolysis and thermal degradation. Viscosity measurements are carried out with complex machines that required constant calibration and long wait times. Changes in oil viscosity in vehicles operated in extreme conditions result in major breakdowns and repairs. Preventive maintenance schedules may not be enough to prevent these breakdowns. As such, in-field viscosity monitoring is needed. Micro-electro-mechanical (MEMS) devices present the ideal solution by providing a small, reliable and inexpensive platform in which a viscometer can be developed and fabricated.

Current MEMS based viscosity sensors utilize changes in resonant frequencies of cantilever beams, plates, membranes or quartz crystals to correlate viscosity changes. These devices are considered vibration viscometers in which the damping of an oscillating electromechanical resonator immersed in the test liquid is measured. Complex actuation and sensing methods, which are usually non-CMOS compatible, make these devices quite challenging to fabricate and integrate. References [1], [2] and [3], utilize an electromagnetic driven cantilever beam or plate, which require the use of a strong external magnet, and an optical readout method, both of which are not easily integrated in a CMOS platform. Reference [4] uses ZnO to achieve ultrasonic piezoelectric actuation of a very long microprobe with a piezoresistor read out. ZnO is not a standard CMOS material and the length of the vibrating microprobe raises material reliability questions. Reference [5] also proposes the use of a ZnO piezoelectric membrane, which improves the reliability although not the CMOS compatibility, with an optical read out. Piezoelectric quartz crystal and ZnO are also used by [6] and [7] to correlate changes in the transmitted surface acoustic wave frequency to density and viscosity changes.

The proposed device looks to solve the CMOS compatibility issue and avoid the use of any external components for actuation and read out. It is based on thermally induced vibrations of a simple silicon plate and its damping due to the surrounding fluid. This MEMS viscometer would provide a device with thermal actuation and electrical output, both of which utilize CMOS compatible materials leading to an inexpensive and reliable system.

Chapter 2.

LITERATURE REVIEW

2.1 General oil viscosity considerations

Viscosity is a measure of the internal friction of a fluid. It is defined as the resistance of a fluid to flow. Newton in 1687 defined viscosity as "the resistance which arises from the lack of slipperiness of the parts of the liquid, other things being equal, is proportional to the velocity with which the parts of the liquid are separated from one another" [8]. In the classical parallel plane Couette flow-analogy shown in Figure 1 with two parallel planes with fluid between them. The upper plane moves with velocity U. The lengths of the arrows between the planes are proportional to the local velocity v_x.. The force per unit area (shear stress) required to produce motion is proportional to the velocity gradient *(U/d)*. The constant of proportionality is called the coefficient of viscosity such that:

$$\frac{F}{A} = \eta \frac{U}{d} \qquad (1)$$

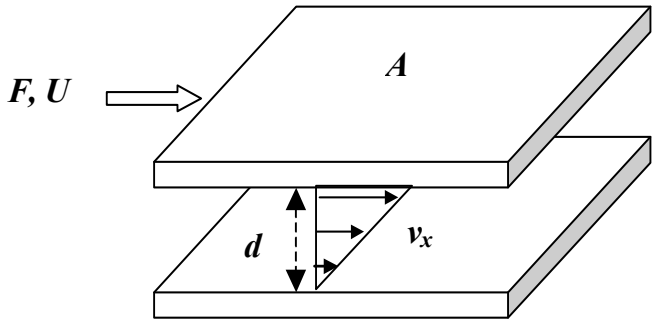

Figure 1. Liquid between two parallel plates and viscosity.

The SI units of viscosity, also called dynamic or absolute viscosity, are Pascal-second [Pa.s]. It is common to see units of Poise, which is a unit 10 times smaller than the Pa.s. As such 1 cP (centipoise) = 1 mPa.s (milli-Pascal second). This is a convenient unit to use as the viscosity of water at room temperature is approximately 1 cP = 1 x 10-3 Pa.s. Viscosity can also be presented as kinematic viscosity, which is the ratio of dynamic viscosity to the density of the fluid, $\upsilon=\eta/\rho$. Kinematic viscosity is what is actually measured by the more simple viscometers, which utilize gravity as a constant force to move the fluid.

When the liquid viscosity remains constant independently of the rate of the shear stress, the liquid is said to be a Newtonian viscous liquid. Oils and lubricants are usually considered Newtonian. When the viscosity of the liquid varies depending on the rate of shear stress, is known as non-Newtonian behavior. Blood is a typical non-Newtonian liquid. Non-Newtonian liquids can still be studied as Newtonian if they present a range of values where the rate of shear stress has little effect on viscosity.

Different methods and apparatus exist to measure the value of the coefficient of viscosity η of Newtonian liquids. These apparatus utilize the basic equation (1) in relation with other physical elements of the system and calibration factors to obtain a value for absolute viscosity. These devices include capillary, rotational, falling ball, vibrational and ultrasonic viscometers. Rotational viscometers are one of the most common. Such instruments rely on rotational motion to achieve a shearing flow of a liquid between two members or plates. By driving and measuring the coupling of one member to the other one can measure the amount of shear viscosity using equation 1.

More convenient is the use of calibrated samples of known kinematic viscosity to obtain values for υ of the liquid under test. This is the case for the standard by the Society of Automovie Engineers (SAE), which uses a Saybolt viscometer. This viscometer measures kinematic viscosity and is based on the time that it takes for 60 milliliters of oil to flow out of a container with a known orifice diameter at either 40 °C or 100 °C.

It is important to note the very strong correlation of oil viscosity with temperature. It follows the following approximate Arrhenius relationship:

$$\eta = Ae^{-B/T} \tag{2}$$

where A and B are constants of the liquid that can be solved if the viscosity values are known at two different temperatures as described in the preceding paragraph. Most manufacturers publish spec-sheets for their oil stating these two values. With this information it is possible to predict the viscosity of the oil at any temperature – even below 40 °C where the viscosity will be significantly higher and will not require very sensitive instrumentation. This strong dependence on temperature needs to be taken into account when designing and operating viscosity measurement tools.

The SAE viscosity grade classification corresponds to a range of viscosity values at the engine operating temperature of 100 °C, which will provide the needed lubrication as determined by the engine manufacturer. Table 1 shows the specification values of SAE Viscosity Grades for engine oils. With this information the chemical companies can manufacture their lubricating oil to meet these standards.

Table 1 SAE VISCOSITY GRADE CLASSIFICATION FOR ENGINE OILS AT 100°C.

SAE Viscosity Grade	Low Shear Rate Kinematic Viscosity (cSt) at 100 °C Min.	Low Shear Rate Kinematic Viscosity (cSt) at 100 °C Max.
20	5.6	< 9.3
30	9.3	<12.5
40	12.5	<16.3
40	12.5	<16.3
50	16.3	<21.9
60	21.9	<26.1

This information also gives us a range of values for which our sensor has to be able to detect changes in viscosity. At 100 °C, our sensor must be able to sense a difference of 4 cSt to be able to determine when the oil integrity is no longer within the safe limits.

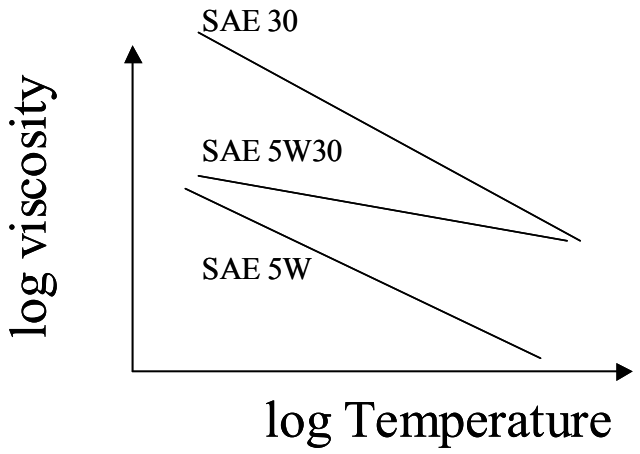

Figure 2. Comparison of monograde and multigrade oils.

For multi-grade oils, the prefix number before the W indicates the viscosity grade in cold conditions as shown in Table 2 . The number after the W indicates the high temperature viscosity as in Table 1 . Multi-grade oils usually contain a base-oil and viscosity improvers. The base oil allows the liquid to flow at low temperatures as described by the W classification. The viscosity improvers prevent excessive thinning at high temperatures and give the oil the high-temperature classification. For examples a

SAE 5W30 oil is a SAE 5W base oil with viscosity improvers that make it act like a SAE 30 at high temperatures. The behavior of multi-grade oils can be seen in Figure 2 where oils classified as SAE 5W and SAE 30 are plotted against a SAE 5W30. The slope of the SAE 5W30 is much less steep as the viscosity improvers prevent the oil classified as SAE 5W to thin down excessively, as it would without the additives.

Table 2 SAE VISCOSITY GRADE CLASSIFICATION FOR ENGINE OILS AT COLD TEMPERATURES

SAE Viscosity Grade	Low-Temperature (°C) Cranking Viscosity (cSt) Max	Low Shear Rate Kinematic Viscosity (cSt) at 100°C Min.
0W	6200 at 35	3.8
5W	6600 at- 30	3.8
10W	7000 at -25	4.1
15W	7000 at -20	5.6
20W	9500 at -15	5.6
25W	13000 at -10	9.3

2.2 Viscometers

Viscometers can either measure absolute viscosity or kinematic viscosity depending on the method employed. Kinematic viscosity is measured when a fixed resistance to flow is applied to the fluid, such as in a Saybolt viscometer where a fixed orifice is used to constrict the flow. The kinematic viscosity of the fluid determines how fast the liquid will flow. On the other hand, absolute or dynamic viscosity is measured when an object is moved through a fluid. In this case, the internal resistance of the fluid opposes the motion of this object and more force is needed to move the object if the fluid is more viscous. On

doing so, the absolute viscosity is measured. Viscometers can be generally classified in four types: rotational, constricted flow, falling ball and vibrational.

Rotational viscometers can operate in two ways. The first method is based on measuring the rate of rotation of a solid shape immersed in a viscous fluid. A known force or torque can be applied to rotate the solid shape and the resulting angular velocity can be measured to obtain a measure of dynamic or absolute viscosity. The second method is to measure the force or torque that needs to be applied in order to obtain a certain rate of rotation. Rotational viscometers include different geometrical shapes such as the coaxial-cylinder, cone and plate, coni-cylinder viscometer or parallel plate.

Constricted flow viscometers include capillary and orifice viscometers. The Saybolt viscometer, used by the SAE standards to classify motor oil viscosity grades, is an orifice viscometer. These are the simplest and the most widely used for measuring viscosity of Newtonian liquids [11]. In these types of viscometers the volumetric flow rate of the liquid is measured by timing how long it takes for a known volume of liquid to pass through either two graduation marks or an orifice of known dimensions. The liquid flows under the influence of gravity or an external force such a pneumatic pump. The kinematic viscosity of the liquid can be determined based on the volumetric flow, pressure and other dimensions of the instrument. Calibration to liquids of known viscosities is needed. For orifice viscometer, the kinematic viscosity is calculated using the general formula

$$\upsilon = \frac{\eta}{\rho} = kt - \frac{K}{t} \qquad (3)$$

where ***t*** is the time that takes for the known volume of liquid to pass through the orifice and ***k*** and ***K*** are instruments constant that must be determined with calibration fluids.

Falling ball viscometers are based on the drag and buoyancy forces generated as an object falls inside a viscous medium. The solid body can be of any shape and size but generally a sphere is used for simplicity. The general solution of absolute viscosity is given by the following equation:

$$\eta = \frac{2}{9}\frac{\rho_S - \rho_F}{V_S} gR^2 \qquad (4)$$

where ρ_S and ρ_F are the densities of the solid and the fluid, V_s is the terminal velocity of the solid sphere, R the radius and g the gravitational acceleration.

Vibrational viscometers are widely used by the petrochemical industry due to the fact that only need small samples of fluids and can be integrated on-line for continuous measurements [11]. Vibrational viscometer measures the damping of an oscillating resonator immersed in the test liquid. The electromechanical resonator can be a cantilever beam, a cantilever plate, an oscillating sphere or a vibrating wire. The damping can be measured by a feedback loop controlling the power needed to maintain constant amplitude of vibration, measuring the peak of resonance and the quality factor Q or by stopping the resonance and measuring the decay of the oscillation. Methods of actuation are generally electromagnetic or piezoelectric. The vibration is sensed by electromagnetic methods, optically or with the use of piezoresistive strain gages.

2.3 MEMS Viscometers

There are many references in the literature to MEMS viscometers. Currently, the majority of these are based on vibrating micro cantilever structures. The miniaturization of bulky viscometers started with the micromachined application of acoustic wave-based

quartz crystal resonators. Less common methods to measure viscosity of fluids utilize pressure differentials or image processing on capillary micro fluidic systems.

2.3.1 Quartz crystal resonators

Quartz crystal resonators were originally used through the 1980's as a microbalance [12]. The piezoelectric properties of quartz crystals allow these structures to resonate at an acoustic frequency of a few MHz's when an electrical potential is applied on a set of electrodes. The acoustic wave generated travels on the surface generating a mechanical vibration that is picked up by another set of electrodes some distance away. Differences between the send and received signal are very sensitive to the mass on the surface of the structure. As microbalances, these devices have been used by the microelectronic industry for in-situ monitoring of thin film deposition as the added mass results in resonant frequency changes. When these devices interact with fluids the surface vibrations generates a shear oscillation that couples with the fluid and generates a frequency change in resonance that is proportional to the square root of the viscosity-density product of the fluid in question. As depicted in Figure 3, this fluid-mechanical coupling happens near the surface of the quartz resonator [13]. The accepted equation to describe the resonant frequency changes is presented below, where η_L and ρ_L are the viscosity and density of the liquid, μ_Q and ρ_Q are the elastic modulus and the density of quartz and f_o is the natural frequency of the free crystal [14].

$$\Delta f = -f_o^{3/2}\left(\frac{\eta_L \rho_L}{\pi \mu_Q \rho_Q}\right)^{1/2} \tag{5}$$

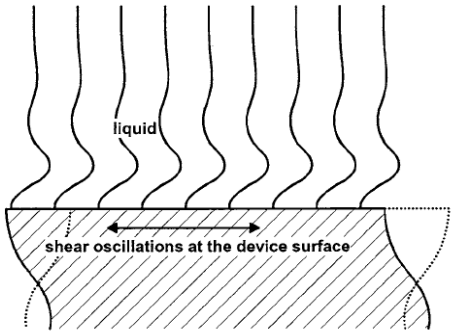

Figure 3. Representaion of fluid-mechancial coupling of transversal surface acoustic wave resonators [14].

Although models have been generated that separate the viscosity-density product [15], the generally accepted practice with respect to motor oil monitoring is that during oil degradation, the change in density will be insignificant when compared to the change in viscosity. Recent developments such as surface corrugation and roughing have allowed for liquid trapping to take place on the surface of the sensor, which leads to a better differentiation between density and viscosity changes [16], [17]. Due to the simplicity of these devices, they have been commercialized and some auto manufacturers include such sensors in their vehicles. SenGenuity in New Hampshire [18] and Bosch in Germany [16] each have their own version. Several field studies have been reported and the general consensus is that these devices do a good job at predicting the viscosity of motor oil [9], [13], [19], [20], [21]. Two major drawbacks for this sensor are its high frequency of oscillation and small vibration amplitude. During comparative studies this sensor has failed to detect oil degradation due to polymer additives, which are present on most common multi-grade oils [20]. These polymers are long chain molecules that affect the viscosity of the oil on a macroscopic scale. Due to the shallow nature of the fluid-mechanical coupling only the properties of the mineral base oil can be reliably measured.

To avoid such problems it has been suggested that the vibration should be of lower frequency and larger amplitude [15].

The MEMS adaptation of this device seems to favor its application as a microbalance for biological applications [22], [23], [24]. The use of this device as a fluid viscosity/density rheometer has been undertaken by different groups [25], [7]. One of the disadvantages of this approach is that quartz crystals can be made relatively small and the size advantage of MEMS devices is diminished. Another reason is the difficulty of integrating piezoelectric films on MEMS fabrication. The MEMS version of this device fabricated on a silicon substrate contains a piezoelectric membrane suspended on a silicon frame with metal electrodes used to send and receive the surface acoustic wave. This piezoelectric membrane can be either self-standing or deposited on top of a thin Si or Si_3N_4 [25] membrane. Materials such as ZnO and $PbO\text{-}ZrO_2\text{-}TiO_2$ (PZT) are used for their piezoelectric properties but are not easily integrated into a semiconductor facility due to CMOS contamination issues [26]. A schematic view of such a MEMS sensor is shown in Figure 4.

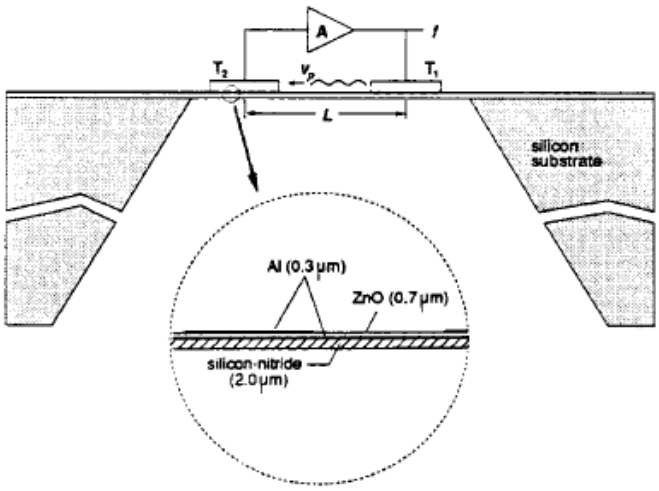

Figure 4. Schematic view of a MEMS SAW sensor [22].

2.3.2 Capillary type MEMS viscometers

Capillary type MEMS viscometers are far less common than both SAW and vibration types. They require the fabrication of micro fluidic channels and an external pump actuation to obtain liquid flow. The most typical implementation includes a micro fluidic system, which can simultaneously detect the flow rate, the pressure drop and the temperature of a fluid through a known distance to measure the viscosity of a fluid [27]. Previous attempts have used optical techniques to measure flow rate in a micro channel for comparative measurements [24, 25].

2.3.3 Vibrating cantilever beams and plates

Vibrating cantilever beams or plates are the most common type of MEMS viscometers. Some of the first studies on viscous damping are found in relation to vibrating MEMS accelerometer diaphragms and the effect on acceleration measurements [30], [31]. It was observed that sufficiently viscous oil could effectively reduce the amplitude of the natural frequency of vibration. This reduction on amplitude is due to an increase virtual mass on the structure. The strong dependence of oil viscosity with temperature was also observed and reported in this early paper. Cantilever beams fabricated for Atomic Force Microscope (AFM) applications were then used on different studies to quantify density and viscosity of liquids [32]. This AFM tips were actuated photo-thermically or with the use of a piezoelectric material. Their movement was analyzed optically [28, 29]. Theoretical equations were derived to couple the mechanical oscillations of the cantilever beam and the fluid interaction via the Navier-Stokes equations assuming non-compressible Newtonian fluids [28, 31]. It is not until the turn of

the century that we start seeing cantilever beams exclusively fabricated for rheology measurements that incorporate piezoelectric materials for actuation [15], [36], [37], [4], [38]. We also start seeing the use of electromagnetic forces to move cantilever plates either by interacting with beams composed of magnetic material [39] or with cantilever plates carrying alternating current (AC) [40], [2], [41], [42], [2]. The majority of these devices utilize optical means to interrogate the amplitude and frequency of the vibrations. Most of the theoretical analysis and models are carried out to show that resonant frequency shifts determine the shift in density and Q changes determine the viscosity. On the other hand, a group led by Belmiloud, out of the University of Bordeaux has shown that sweeping the frequencies will also relay information on the rheological properties of the fluid, especially on those that are viscous enough to completely dampen resonance.

Larger plates, instead of long beams, are used in devices that use AC-carrying metal lines in order to generate a sufficiently large Lorentz force to move the structure significantly. The main contributor to this type of devices is the group from the Schulemberger Limited Company in Germany and England as they are trying to develop a rugged and reliable sensor to be used in their oil-field-exploration efforts [1, 3, 23, 39 - 48]. Over the last five years (2005-2009) they have published numerous papers studying both theoretical and experimental factors of their patented technology. On a more recent adaptation of their device they have develop a device called “The Spider”. This device utilizes AC current flowing transversally across a series of silicon supporting legs to produce a sharing motion on the liquid. The resonant frequency and amplitude of this device is detected through a series of piezoresistive elements also incorporated on the many legs of “The Spider” [38, 44, 49].

The main disadvantages of these types of devices are the use of non-CMOS materials for the piezoelectric-actuated beams and the need of an external magnet for the cantilever plates. Piezoelectric materials are not part of a standard CMOS manufacturing process and are not welcomed in a semiconductor manufacturing lab due to their potential for contamination as deep traps of carrier which leads to diminish performance of CMOS devices [26]. On the other hand, magnetically-actuated plates utilize CMOS-compatible processing but require the use of an external magnet – or electromagnet – which increases the overall size and price of the system and lessens the advantage that micro-machining offers.

Another obvious limitation of the vibrating cantilever and plates mentioned above which does not seem to have been studied yet is their reliability. In the case of cantilever beams, the structures tend to be long and thin in order to maximize sensitivity. In the case of cantilever plates, the element connecting to the main substrate needs to be small and flexible enough to allow enough vertical motion due to the Lorentz force. Either configuration leads to weak points which are under large strain/stress conditions potentially leading to significant material fatigue and shifts in resonant frequencies or q-factors, which are the key measurements of the technology.

Vibrating membranes are a less common type of MEMS viscometers but provide an opportunity for a much rugged structure. Most of the vibrating devices have been designed with shearing surfaces in contact with the liquid as it has been accepted that shearing forces are needed in order to determine the viscosity of a liquid. The classical theoretical model of vibrating membranes in liquid only takes into account the value of the density of the liquid to determine the vibrating characteristics. Lamb's model

proposed the use of a virtual added mass, which would change the vibrating characteristics of the membrane due to density, ignoring the viscosity of the fluid. Oliver Brand et al. presented in a 1997 paper a thermal actuated silicon membrane with piezoresistive sensing – similar to the subject of this study – for viscosity measurements [54]. Density was kept relatively constant as viscosity was changed by several orders of magnitude. Q was measured in relation to viscosity both as the amplitude transfer characteristic around the natural resonance and as the time decay after a burst excitation. No theoretical proposal is given for the observed effect and no further work on this structure was undertaken. Instead this group extensively pursued an ultrasonic proximity sensor application of thermally actuated silicon resonators [33 - 40]. In 2006 a paper by Ayela and Nicu explored Lamb's model on MEMS piezoelectric membranes confirming its validity up to liquids with a viscosity of 10 cP. Beyond that point the vibrating characteristics of the membranes started to deviate from Lamb's model significantly [5]. It has been recently proposed by Kozlovsky that this deviation is due to the fact that the viscosity of the liquid can no longer be ignored when the thickness of the vibrating plate is thin enough, as it is the case with MEMS structures [63]. Kozlovsky confirms the observation made by Brand et al and Ayela and Nico and proposes a modification to Lamb's model in which the viscosity is added to the virtual added mass of the plate when the plate thickness is made thin enough. The development of this theory on plate-fluid interaction will be explored in detail in the next sections.

Table 3 below summarizes some of the work that has been done on MEMS viscometers over the last few years. This list is not all-inclusive, many more studies have been carried out but it should give the reader an idea of what the main trends are. As can

be seen from this Table the great majority of sensors utilize micro-cantilever structures. Electromagnetic or piezoelectric actuation with optical sensing is the most common configuration.

Table 3 MEMS VISCOMETERS.

Year	Authors	Type	Actuation	Sensing	Size	Material	Ref.
1991	Tschan - ASCOM Microelectronics	50g Si membrane accelerometer	Accelerometer/ vibrating table	Piezoresistive	NA	Si membrane with mass	[30]
1993	Meyer-Fraunhofer	Flexural pate-waves-acoustic	Electrostatic IDT	Capacitive	5mmx1.5mmx1.5um	Si, Si3N4	[64]
1995	Andrews-New Zealand	Squeeze flow	Electrostatic	Capacitive	NA	Si plates squeezing liquid	[31]
1995	Enoksson-Sweden	Vibrating tube	Electrostatic	Electrostatic	NA	bonded Si wafers	[65]
1996	Oden-TN	AFM Cantilever	Piezoelectric	Optical	225x27x2.4um	Si, PZT	[34]
1996	Weigert - Switzerland	AFM Cantilever	Piezoelectric	Optical	mm's	Si, PZT	[33]
1997	O. Brand - Georgia	Si membrane	Thermal	Piezoresistive	3mmx3mm	Si	[54]
Year	Authors	Type	Actuation	Sensing	Size	Material	Ref.
1998	Hirai-Japan	Cantilever beam	Photothermal	Optical	0.3x200x200um	0.2um of Si3N4 with 20nm Au	[66]
1998	Galambos	Capillary	Micro fluidic channel	Optical	cm's	Si	[28]
1998	Martin-Sandia Labs	Magnetic flexural plate	Magnetic	Impedance	mm's	Si3N4	[17]
2001	Shih-Drexel PA	Stainless-steel and PZT - Not mems	Piezoelectric	Piezoelectric	cm's	Stainless steel and PZT	[36]
2002	Boskovic	AFM Cantilever	Piezoelectric	Optical	397x29x2um	Si, PZT	[67]
2003	Naik-U of MI	PZT Bimorph	Piezoelectric	Optical	10.5x1x0.5mm	Plastics,PZT	[37]

Year	Authors	Type	Actuation	Sensing	Size	Material	Ref.
2005	Agoston-AC2T Resrch, Austria	U-shape micro cantilever	Electromagnetic	Optical	1500x100x15um -	Au conductor and Si frame	[40]
2005	Zhao-Carnegie Mellon	SU8-Nickel Cantilever	Electro-magnetic	Laser	600x500x7.5um.	SU8, Nickel	[68]
2005	Blom-MESA, Netherlands	Capillary	Fluidic	Pressure differential on bridge sensor	mm's	Si	[29]
2006	Ramkumar-Cornell	Cantilever beam	Piezoelectric	Piezoresistive	100x140x5000um	PZT glued on Si	[4]
2007	Reichel-Kepler U., Austria	Flexural pate-waves-structural	Electro-magnetic	Electro-magnetic	5.6mmx12mmx1.5mm	Polyester based foil-not mems	[69]
2008	Belmiloud - IXL, France	Cantilever beam	Electro-magnetic	Optical	23x600x4000um	NA	[2,70,71]
2008	Angelescu - Schlumberger	Capillary	Microfluidic channel	pressure, flow rate	cm's	Si	[27]
2008	Ebisui-Japan	Capillary	Laser Induced Capillary Wave	Optical	mm's	Si	[72]
2009	Huang-Columbia U, NY	Permalloy on catilever	Electro-magnetic	Optical	250x250x2um	parylene cantilever, permalloy on tip	[39]
2009	Rezazadeh - Iran	Cantilever plate	Piezoelectric	Capacitive	NA	Si	[38]
2009	Zeng - Ohio State	Capillary	Fluidic	Resistivity	NA	Si	[73]
2009	Sparks - ISS-MI	Resonating tube	Electrostatic	Capacitive	NA	Si	[74]
1985 - 2009	Several	SAW-BAW-Ultrasonic plate waves	Piezoelectric	Piezoelectric	mm's	quartz-crystal, metal	[6,7,12,14,17,18,25,75-82]
2004 - 2009	Schulemberger	Vertical moving plate	Electro-magnetic	Optical, piezoeletric	2mmx1.5mmx25um	Si	[1,3,27,43-52,83]
2006 - 2009	Schulemberger (Spider)	Horizontal moving plate	Electro-magnetic	Optical, piezoeletric	2.4mmx1.6mmx25um	Si	[42,48,53]

2.4 Analysis of cantilever beam viscometers

The studies presented above use different models to solve the analytical problem of a vibrating cantilever beam in a viscous liquid. The exact solution is too complex and most of these models assume certain conditions and approximations. Two major approaches can be found: one takes the beam as a unit and approximates its vibration to a simple harmonic oscillation with an added mass to account for density changes and an added damping coefficient to account for the viscous fluid, the second approximation models the beam as a continuous system and solves the fluid hydrodynamic function using either the Navier-Stokes and continuity equations or other physical models and couples it to the equation of the vibrating beam. This second approximation leads to a fluid force that is either modeled again as an additional mass and damping coefficient or as an external force.

2.4.1 Simple Harmonic Oscillator (SHO) model

The simplest model of a viscous damped free vibrating object is that of a mass-spring-damper system. The equation to describe the motion of this object is derived from Figure 5 by balancing the spring and damping forces of an effective mass $\boldsymbol{m}$ with a initial displacement $\boldsymbol{x}$ and can be written as follows:

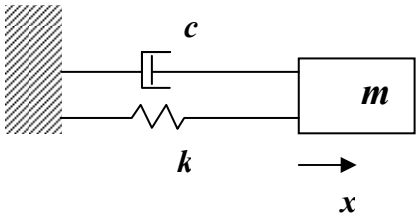

$$m\frac{\partial^2 x}{\partial t^2} + c\frac{\partial x}{\partial t} + kx = 0 \qquad (6)$$

Figure 5. Simple harmonic oscillator model.

Where ***k*** is the spring constant of the beam, which can be approximated by knowing its geometry – width ***b***, thickness ***h*** and Length ***L*** – and its young's modulus ***E***.

$$k = \frac{Ebh^3}{4L^3} \qquad (7)$$

c is the spring and damping constant of the system and its magnitude will determine whether the system is underdamped, critically damped or overdamped.

When forced vibrations are considered, the equation can be rewritten to include a harmonic force following the general form below.

$$m\frac{\partial^2 x}{\partial t^2} + c\frac{\partial x}{\partial t} + kx = F_o e^{-i\omega t} \qquad (8)$$

When modeling the behavior of a vibrating cantilever in a fluid using the above equation the shape of the cantilever is usually approximated to be that of a sphere as detailed in Landau and Lifshitz [84]. The analysis is carried out by assuming that the vibration amplitude is smaller than the size of the vibrating object. The drag force of the cantilever can be approximated by considering that a fixed determinable volume of fluid mass will be carried along with the lever thought its oscillation cycle as. This added mass will decrease the resonance peak frequency as well as the qualify factor. This drag force can be expressed as follows:

$$F_{drag} = m_i \frac{\partial^2 x}{\partial t^2} + c_i \frac{\partial x}{\partial t} \qquad (9)$$

The induced mass modeled by the sphere of radius R vibrating at a high frequency can be approximated by decomposing the mass ***m*** into two terms to account for the mass of the cantilever m_e and the fluid induced mass m_i, which depends on the fluid density [34], [36]and [85].

$$m = m_e + m_i = m_e + \frac{2\pi R^3}{3}\rho \tag{10}$$

Similarly, the dampening of the motion of the sphere also takes into account the density of the fluid as well as its viscosity and can be modeled as follows:

$$c = c_e + c_i = c_e + \frac{6\pi\eta R^2}{\sqrt{\frac{2\eta}{\rho\omega}}} \tag{11}$$

By measuring the frequency response of the cantilever in air or vacuum one can determine the effective mass and dampening coefficient m_e and c_e. When the same measurement is taking in a liquid the resonant frequency will change according to the next equation:

$$\omega_l^2 = \omega_o^2 - \frac{1}{2}\gamma^2 \tag{12}$$

where ω_o depend on the added induced mass and is the defined as:

$$\omega_o = \sqrt{\frac{k}{m_e + m_i}} \tag{13}$$

and γ take into account the dampening as:

$$\gamma = \frac{c_e + c_i}{m_e + m_i} \tag{14}$$

From equations (12)-(14) it can be seen the both the density and viscosity will have an effect at lowering the frequency of the oscillator in the liquid. This model does not

differentiate between the density and viscosity as it only gives us information about the variation on resonance frequency.

2.4.2 Continuous system model

The continuous system does not only rely on the behavior of the beam around the region of its natural frequency of vibration but it analyzes the motion of the beam as a function of frequencies. This allow for the analysis of its dampening behavior away from its resonance, which helps to determine the quality factor Q.

The equation that describes the motion of a vibrating cantilever beam, according to the coordinate system of Figure 6, is well-known and is presented below:

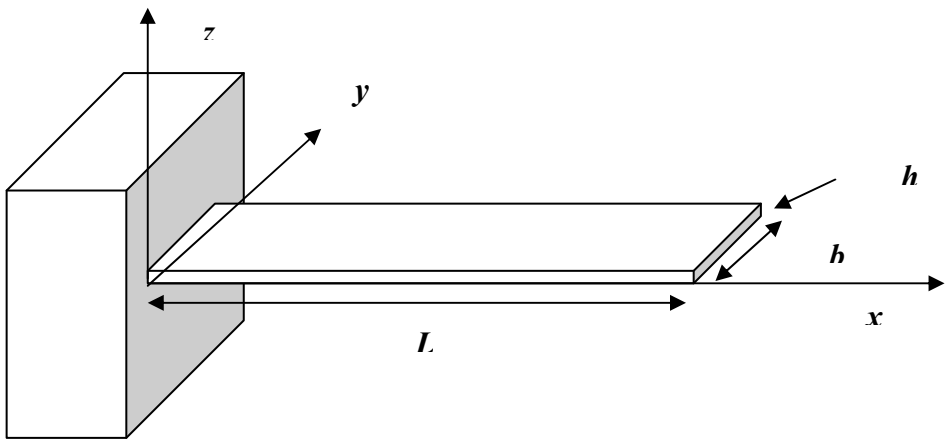

Figure 6. Coordinate system of cantilever beam.

$$EI\frac{\partial^4 z(x,t)}{\partial x^4}+\rho A\frac{\partial^2 z(x,t)}{\partial t^2}=F(x,t) \qquad (15)$$

This equation describes the vertical movement of the beam z(x,t) as a function of position ***x*** and time ***t***. ***E*** is the Young's modulus of the beam, ρ its density and ***A*** its area. This function also depends on the external forces which are described by ***F(x,t).***

Similarly, if the width ***b*** of the beam is comparable to its length L, the plate equation can be used:

$$\frac{Eh^3}{12(1-\nu^2)}\frac{\partial^4 z(x,t)}{\partial x^4}+\rho h\frac{\partial^2 z(x,t)}{\partial t^2}=F(x,t) \qquad (16)$$

For both equations 15 and 16 the value ***F(x,t)*** will determine the amplitude and frequency of the vibrations. ***F(x,t)*** is usually defined as the sum of the driving force and the fluid force that opposes this motion:

$$F(x,t)=F_{DRIVE}(x,t)+F_{FLUID}(x,t) \qquad (17)$$

$\boldsymbol{F_{DRIVE}(x,t)}$ is often defined as a harmonic function of the form of $\boldsymbol{e^{-i\omega t}}$ to simplify some of the calculations when the driving force is electromagnetic of piezoelectric. When the driving mechanism is thermal then it is replaced by the thermal moment and complicate the fourth order differential equation even further. For the cantilever beam equation, it takes the following form:

$$EI\frac{\partial^4 z(x,t)}{\partial x^4}+\rho A\frac{\partial^2 z(x,t)}{\partial t^2}=\frac{\partial^2 M_T}{\partial x^2}+F_{FLUID}(x,t) \qquad (18)$$

where $\boldsymbol{M_T}$ is the thermal moment and needs to be solved depending on the thermal input that is applied to the structure.

To solve the $\boldsymbol{F_{FLUID}}$ equation several approaches have been taken. Weigert [33] and Hirai [66] approximated the fluid reaction by describing a string of beads model distributed along the length of the cantilever beam. This method is similar to the applied for the simple harmonic oscillator described above and is based on the fact that a cantilever beam vibrating in a liquid will experience a virtual added mass that will lower the frequency of vibration and a viscosity that will also dampen it. Weigert used a string

of cylinders while Hirai used a string of spheres. Weigert does not solve the fourth order differential equation but obtains a relationship to account for the natural frequency shifts due to density similar to the results of the SHO method above.

The more complete approximation seems to be the one done by Sader in 1998 where he solved the Navier Stokes equations for an AFM cantilever beam vibrating in a liquid with the appropriate boundary conditions using Rosenhead's vibrating cylindrical beam solution. The solutions lead to a fluid force that is dependent on a hydrodynamic function that depends on the geometry of the cross section of the cantilever and the viscosity and the density of the fluid. This hydrodynamic function is used together with the SHO model around a resonant peak where the amplitude A of the vibration is defined as:

$$A(\omega) = \frac{A_0 \omega_R^2}{\sqrt{(\omega^2 - \omega_R^2)^2 + \frac{\omega^2 \omega_R^2}{Q^2}}}, \tag{19}$$

where A_0 is the zero-frequency amplitude of the response, ω the radial frequency, ω_R the radial resonant frequency and Q the quality factor. The formulas for Q and ω_R incorporate the hydrodynamic function $\Gamma(\omega)$ as follows:

$$\omega_R = \frac{\omega_{vac}}{\sqrt{1 + \frac{\pi \rho b^2}{4\mu} \Gamma_r(\omega_R)}} \tag{20}$$

and

$$Q = \frac{\frac{4\mu}{\pi \rho b^2} + \Gamma_r(\omega_R)}{\Gamma_i(\omega_R)}, \tag{21}$$

where μ is the mass per unit length of the cantilever and the hydrodynamic function has a real and imaginary component as described in detail in Sader [32].

Using these equations the density and the viscosity of a liquid can be determined if measurements of the natural frequency and the quality factor of the cantilever beam can be performed by solving the simultaneous equations where they are the only unknowns. This method has been verified to be adequate by [67] and [86].

Belmiloud in 2006 went a step further by modifying Sader's hydrodynamic function in order to include the viscoelastic effects of non-Newtonian fluids. He included the complex shear modulus characteristic of the long-chained-polymer Maxwellian fluids in the hydrodynamic functions [8]. By computationally solving the resultant fourth order differential equation he was able to produce the full vibration frequency spectra of a cantilever beam to show that the viscosity of a liquid did not only affect the shape of the resonant peak but also the amplitude of lower frequency components [2,70,71].

Chapter 3.

THERMAL VIBRATION OF PLATES

The objective of this work is to develop a vibrating viscosity sensor that is fully compatible with CMOS technology. This is going to be accomplished by using a thermally actuated vibrating silicon diaphragm using impulse excitation.

The analysis of the thermal vibrations of a plate was extensively developed around the 1950's when the aerospace industry was developing rocket-powered high-speed flight. The extremely high temperatures and temperature gradients that resulted from power generation required the analysis of the thermal stresses of the materials [87].

Following the derivation presented during a series of papers during the 1950's and compiled later on a book by Boley and Weiner [88] the analysis of the following plate is carried on:

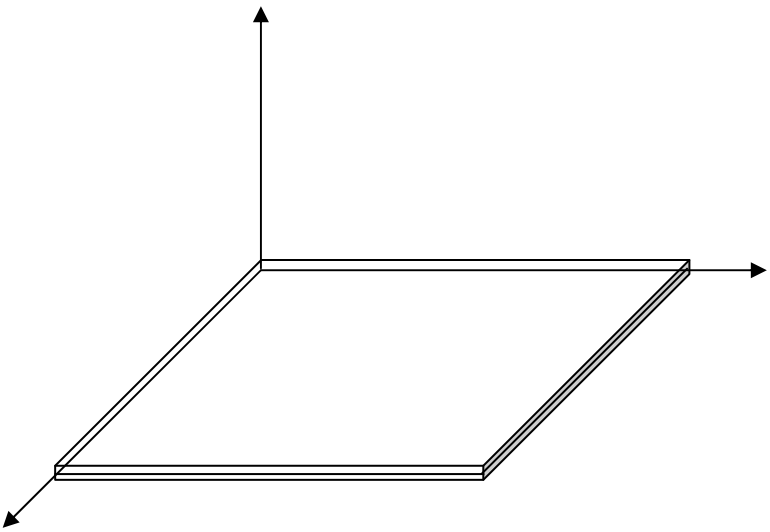

Figure 7. Coordinate system of a thin plate or diaphragm.

This plate in Figure 7 occupies the space $0 \le x \le a$; $0 \le x \le$; $-(h/2) \le z \le (h/2)$. The displacements in the x, y and z directions are denoted by u, v and w respectively. A uniform step heat input applied at ($z=h/2$) and results in a $T(z)$ distribution [89]:

$$T(z,\tau) = \frac{hQ}{k}\left[\begin{array}{l}\tau + \frac{1}{2}\left(\frac{z}{h}+\frac{1}{2}\right)^2 - \frac{1}{6} - \\ \frac{2}{\pi^2}\sum_{j=1}^{\infty}\frac{(-1)^j e^{-j^2\pi^2\tau}}{j^2}\cos j\pi\left(\frac{z}{h}+\frac{1}{2}\right)\end{array}\right] \tag{22}$$

with the non-dimensional time parameter τ defined as the ratio of the thermal diffusivity κ, time t and the thickness of the plate h.

$$\tau = \frac{\kappa t}{h^2} \tag{23}$$

The general equation that describes the thermal vibration of plates is based on the assumption that the slopes and deflections of the pate are small when compared to any of the geometrical lengths of the plate. This assumes that the plane cross-section which are initially perpendicular to the axis of the plate, remain plane and perpendicular to the neutral axis during bending [90].

$$\frac{Eh^3}{12(1-\nu^2)}\frac{\partial^4 w(x,y,t)}{\partial x^4} + \rho h\frac{\partial^2 w(x,y,t)}{\partial t^2} = -\frac{1}{1-\nu}\nabla^2 M_T \tag{24}$$

The solution of this equation for a simply supported plate contains static and dynamic solutions and depends on the step heat input that is applied to the plate. The thermal moment M_T as a function of τ is found to be:

$$M_T = \frac{2\alpha E}{1-\upsilon^2}\int_{-t/2}^{t/2} Tz\,dz = \frac{4\alpha QEh^3}{\pi^4 k}\left(\frac{\pi^4}{96} - \sum_{j=1,3,5}^{\infty}\frac{e^{-j^2\pi^2\tau}}{j^4}\right) \tag{25}$$

The solution in the vertical direction w is found to be

$$w(x,y,t) = w_{st} - w_{dyn} \tag{26}$$

The solution has two components: a static term w_{st} that is not dependent on time and is solved by ignoring the second order time-dependent differential equation, also called the inertia term, and a dynamic term. The inertia term can be ignored when the time rate of change of the temperature is slow enough so that these terms should not be significant [91]. This is not the case in our study when the temperature is rapidly increased. The dynamic term comes from the solution of the inertia term.

The static solution is [84]:

$$w_{st} = \frac{16M_T}{(1-\upsilon)D\pi^4} \sum_{m=1,3,5}^{\infty} \sum_{n=1,3,5}^{\infty} \frac{\sin\left(\frac{m\pi x}{a}\right)\sin\left(\frac{n\pi y}{b}\right)}{mn\left[\left(\frac{m}{a}\right)^2 + \left(\frac{n}{b}\right)^2\right]} \tag{27}$$

where,

$$D = \frac{Eh^3}{12(1-\nu^2)} \tag{28}$$

The dynamic solution w_{dyn} is :

$$w_{dyn} = -\frac{768Q\alpha a^2(1+\upsilon)}{k\pi^8} \sum_{m=1,3,5}^{\infty} \sum_{n=1,3,5}^{\infty} \frac{\sin\left(\frac{m\pi x}{a}\right)\sin\left(\frac{n\pi y}{b}\right)}{mn\left[m^2 + \frac{a^2}{b^2}n^2\right]}$$

$$\times \left[\frac{\pi^2}{8B^2(m^2 + \frac{a^2}{b^2}n^2)} \sin\left[B^2\pi^2(m^2 + \frac{a^2}{b^2}n^2)\tau\right] \right.$$

$$\left. - \sum_{j=1,3,5}^{\infty} \left[\frac{e^{-j^2\pi^2\tau} - \cos\left[B^2\pi^2(m^2 + \frac{a^2}{b^2}n^2)\tau\right]}{j^4 + B^4(m^2 + \frac{a^2}{b^2}n^2)^2} \right.\right.$$

$$\left.\left. + \frac{j^4 \sin\left[B^2\pi^2(m^2 + \frac{a^2}{b^2}n^2)\tau\right]}{\left[j^4 + B^4(m^2 + \frac{a^2}{b^2}n^2)^2\right]\left[B^2(m^2 + \frac{a^2}{b^2}n^2)\right]} \right] \right] \tag{29}$$

where the dominant non-dimensional parameter is introduced as

$$B = \frac{h}{a\sqrt{\kappa}}\left(\frac{D}{h\rho}\right)^{1/4} \tag{30}$$

The frequency of oscillation of the diaphragm will be determined by the time-dependent term. Substituting the values for ***B*** and ***τ***, the first mode of vibration – natural frequency, ***m=n=1*** – for a square diaphragm is reduced to the typical:

$$\omega_n = \frac{B^2\pi^2(m^2 + \frac{a^2}{b^2}n^2)\tau}{t} = \frac{\left(\frac{h}{a\sqrt{\kappa}}\left(\frac{D}{h\rho}\right)^{1/4}\right)^2 2\pi^2 \frac{\kappa t}{h^2}}{t} = \frac{2\pi^2}{a^2}\sqrt{\frac{D}{h\rho}} \tag{31}$$

Substituting typical values for MEMS silicon diaphragms – listed in Table 4 - we can produce the following plots of the center deflection of the diaphragm (***x=a/2***, ***y=b/2***) in which the dependence of the frequency of vibration on the thickness of the diaphragm ***h*** is clearly observed. The calculated natural frequencies of vibration of diaphragms of a = b = 3mm and h = 10 μm, h = 15 μm and h = 30 μm are f_{10um} = 9750 Hz, f_{15um} = 14626 Hz, f_{30um} = 29,251 Hz. The static deflection is of about 1.3 μm and the amplitude of the vibration varies from about 100 nm for h = 10 μm to less than 20 nm for h = 30μm. These values are similar to those measured experimentally and presented in the next sections.

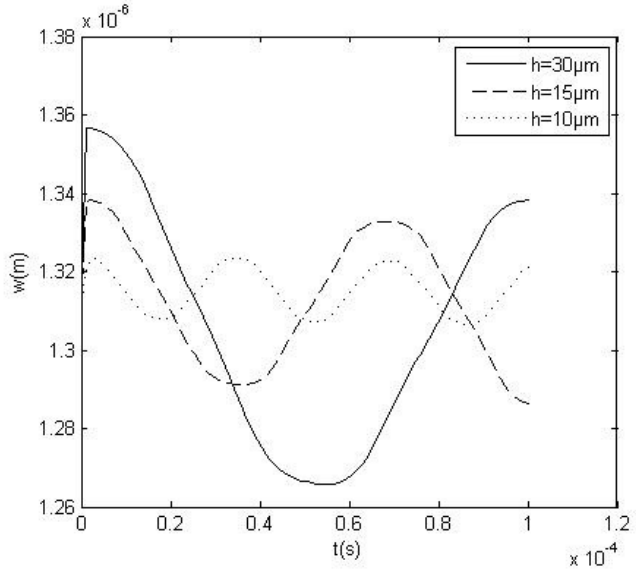

Figure 8. Natural frequency response of thin membranes with a = 3 mm and h = 10, 15 and 30 μm.

To visualize the effect of the diaphragm size on thermal vibrations the thickness of the diaphragm is kept constant at 15 μm and the size varied from $a = b$ = 3 mm to $a = b$ = 2 mm and $a = b$ = 1 mm. As expected the frequency of the vibrations is dependent on the size and it increases as the size is reduced.

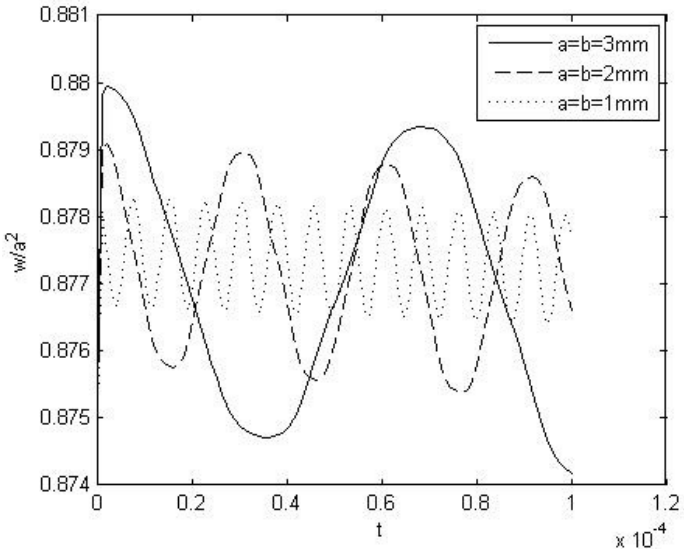

Figure 9. Natural frequency response of thin membranes with *h=15 μm* and a=1, 2 and 3 mm.

Table 4 TYPICAL PARAMETERS FOR MEMS SI SQUARE DIAPHRAGM

Material	Silicon
Density ρ	2230 kg/m^3
Young's modulus E	1.4x10^{11} N/m
Poisson's ratio υ	0.3
Coefficient of thermal expansion α	2.6x10^{-6}/°C
Thermal conductivity k	150 W/m °C
Heat capacity c_p	0.7 J/gc
Thermal diffusivity $\kappa=k/\rho c_p$	0.8x10^{-4} m^2/s

This analysis is valid as long as the structure is rapidly heated. The thermal properties of the system only affect the amplitude of the vibration and have no effect on the frequency of oscillation. When the rate of heat is slower the solution does depend on the thermal characteristics of the system and the solution, as shown in [92]. As such the rate of heat has to be faster than the characteristic thermal time of the structure which is defined as $t_0=h^2/\kappa$. For our typical silicon structure with h = 15 μm, this value is of 1.25 μs.

With the preceding analysis we can start to define the dimensions of thermally actuated silicon resonator. It seems possible to realize a thin and large diaphragm in order to increase the amplitude of vibration. Brand et al. in 1994 studied the dynamic behavior of thermally actuated diaphragms [54], [62]. They concluded that there is a critical thickness to length ratio for which the diaphragm will suffer of non-linearity and buckling effects and will not properly vibrate at its natural frequency.

3.1 Fluid plate interactions

In 1920 Lamb solved the problem of a circular plate vibrating in water and found that the modes of vibrations remain approximately the same but varied in frequency by a

factor called the added virtual mass. Assuming the fluid to be incompressible and inviscid he was able to find the fluid velocity potential. By matching the plate velocity to that of the fluid at the boundary with the plate he then determined their kinetic energies and their ratio. The result is depended on the density of the fluid ρ_{fluid} and plate material ρ_{plate}, the radius of the circular plate a and its thickness h, as follow:

$$\omega_{fluid} = \frac{\omega_{vacuum}}{\sqrt{1+\beta}} \tag{32}$$

where β

$$\beta = 0.669 \frac{\rho_{fluid} a}{\rho_{plate} h} \tag{33}$$

These results are based on assuming a circular plate fixed along its boundary and placed in the aperture of an infinitely rigid wall in contact with water [93]. Different authors have experimentally demonstrated the validity of this equation and proposed different methods to more accurately predict the value of the added virtual mass β [94]. Kwak and Kim in 1996 reformulated the problem adapting the boundary conditions to a simply supported rectangular plate and found modified values for β [95]. In 2000, Chang and Liu calculated the natural frequencies of vibrations of rectangular isotropic plates in contact with fluid for general boundary conditions and geometries [96]. All of these analyses deal with the frequency of vibrations and its changes but do not take into account the viscosity of the fluid. It also does not analyze the quality factor of the resonant frequency and any other energy dissipation effects that could be present due to viscous forces.

The viscous effect is found to be negligible for macroscopic plates but when the thickness of the plate is reduced to the levels found of MEMS devices it must be taken into account. Ayela and Nicu observed this effect in 2007 when they reported the results of micromachined piezoelectric circular membranes vibrating in liquid media [5]. They found that Lamb's model matches well for viscosities of less than 10 cP. Beyond this value the shift in the natural frequencies is larger than that predicted by Lamb. They also report that the Q value of the resonance also degrades as the viscosity increases and more rapidly as the viscosity is greater than 10 cP.

Kozlovsky in 2009 picked up on Ayela and Nicu's report and revisied Lamb's analysis to take the viscosity of the liquid into consideration as an energy dissipative element [63]. He proposed that through the "no-slip" boundary condition, which implies that the tangential velocity vanishes, the viscosity of the fluid actually couples the plate vibration to the tangential velocity of the fluid. This increases the fluid's movement and kinetic energy. Still using a linear form of the Navier-Stokes equations he analyzes the system finding the fluid velocity, its kinetic energy and the added virtual mass taking the effect of the energy dissipated by viscosity.

Kozlovsky's analysis modifies the added virtual mass factor to be:

$$\beta = 0.6538 \frac{\rho_{fluid} a}{\rho_{plate} h}(1 + 1.082\xi) \tag{34}$$

where the energy dissipation of the system is characterized by ξ such that the Q factor, which is defined as the ratio between the energy stored and dissipated per cycle, becomes

$$Q = 2\pi \frac{energy\_stored}{energy\_dissipated\_per\_cycle} \approx \frac{0.95}{\xi} \tag{35}$$

and

$$\xi = \sqrt{\frac{\upsilon}{\omega a^2}} \tag{36}$$

Therefore, knowing both the resonance frequency and the quality factor in the liquid we can calculate the density and the viscosity of the liquid.

Chapter 4.

THERMAL ACTUATOR DESIGN AND FABRICATION

Two major studies were carried out. The first one focused on the silicon membrane thickness and the bimetallic effect. The second study focused on the heater size and thermal isolation with the addition of an extra layer of passivation.

The first study was used to determine the static behavior of the membrane to heat. The main purpose was to optimize the membrane thickness, the amount of metal needed for optimum bimetallic effect and avoid buckling which plays and important part during the vibration of the membranes. The second study was based on the results of the first. The thickness of the membrane was set with respect to its size. The size of the heater was varied and the effect of an additional passivation layer was studied.

The fabrication process for these two major studies was very similar. The only difference being the starting substrate. To reduce variation and obtain a fix membrane thickness, we used SOI wafers with the targeted silicon thickness.

The basic configuration of the proposed thermal resonator is presented in Figure 10, which shows the device layout and graphical representation of the thin silicon diaphragm with the p+-diffused heater actuator, the aluminum bimetal area and piezoresistor Wheatstone bridge sensing element.

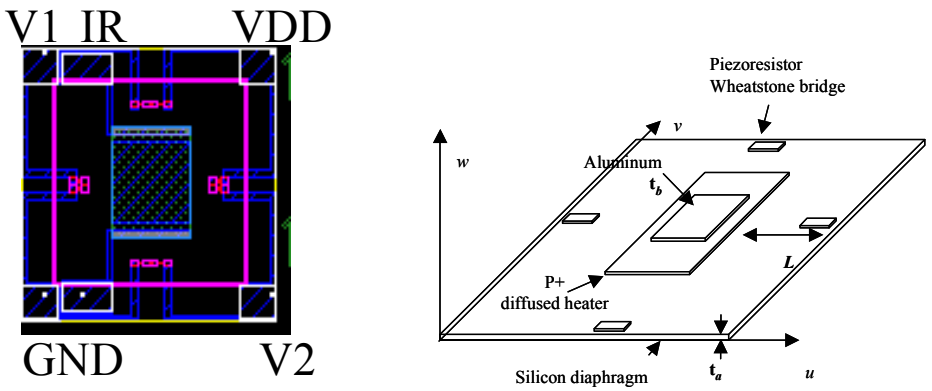

Figure 10. Device layout and graphical representation.

As mentioned in the previous chapters the material of the membrane is mainly silicon but it also includes other layers that are needed to realize an in-situ heater and sensor. Several device variations were fabricated in order to study the effects of these layers on the static deflection as well as on the vibration characteristics.

The membrane was chosen to be square to simplify processing by using a well-established anisotropic KOH etch of silicon. The thickness of the silicon membrane was varied to study the behavior of the actuation.

The in-situ heater was built as either a p-type diffused resistor with a junction depth of approximately 5 µm or a 0.5 µm polysilicon layer sandwiched between two 0.5-µm SiO_2 layers. The effect of the material and size of the heater in relation to the size of the membrane was studied.

Aluminum metal was placed on the center of the diaphragm in order to enhance the deflection of the membrane via the bimetallic effect. The bimetallic effect is based on the difference in thermal expansion coefficient of the membrane and the top aluminum layer. It has been shown through finite element analysis by Zou et al. [97] that placing aluminum on the center of a thin silicon membrane will deflect the diaphragm up. On the other hand, placing aluminum around the edge of the silicon membrane will deflect the

diaphragm down as shown by Puers [98]. The effect of the size of the aluminum pad was studied with respect to the size of the membrane and its thickness. The effect of the aluminum on the vibration characteristic of the actuator was also studied

Additional SiO_2 passivation was used to further isolate the actuation heat from the fluid under test. The effect of the passivation thickness on the vibration characteristic of the actuator was studied.

The amount of vertical movement due to heating is measured via the integrated piezoresistive diffused silicon or polysilicon Wheatstone bridge.

4.1 Device fabrication

A bulk MEMS microfabrication process was used to fabricate the actuator/sensor structure. The fabrication process starts with double-side-polished n-type silicon on oxide (SOI) wafers. The top silicon layer is 15 μm thick and the buried oxide is 1 μm thick. A silicon oxide is grown and used as a masking layer for the P+ spin-on-dopant process, which acts as the heating element of the membrane. After this, a pad silicon oxide is thermally grown and silicon nitride is deposited using a low-pressure chemical vapor deposition (LPCVD) process. Even though the silicon nitride and oxide are patterned on the backside of the wafer by plasma etch with SF_6 and buffered oxide etch (BOE) respectively, the diaphragms are not etched yet. Polysilicon is then deposited via LPCVD on both front and back of the wafer on top of a 0.5-μm insulating oxide layer. The polysilicon on top of the wafer is doped with phosphorous to form the Wheatstone piezoresistor sensor bridge. The polysilicon on the back of the wafer will protect the patterned nitride until the backside etch is performed at the end of the process. A 10,000

Å low temperature oxide layer is then deposited and contact openings to poly and P+ silicon are etched out in a BOE solution. After the contacts are etched, a metal layer of 10,000 Å of aluminum is deposited and then patterned to make the electrical connections and to act as the bimetallic layer. An additional passivation oxide of 1 μm is deposited on the front of the diaphragm in order to provide another layer of temperature isolation and prevent heat loss to the fluid under test. The front of the wafer is then protected with Brewer Science's PROTEK^{TM} and the diaphragms are formed by etching from the back of the wafers. The patterned silicon nitride is used as a protection layer during the silicon KOH-etch. The 1-μm-thick buried oxide of the SOI wafers serves both as an etch-stop layer and as a thermal isolation layer on the back of the diaphragm. Figure 11 shows a final cross-section of the fabricated device. The top version with the polysilicon heater, piezoresistive polysilicon bridge, aluminum plate for enhancement bimetal actuation and an additional SiO_2 passivation layer. The bottom version with a P+ diffused silicon heater, piezoresistive polysilicon bridge and an aluminum plate without the additional thermal passivation. Appendix A includes a process flow with enough detail to replicate the fabrication of these devices.

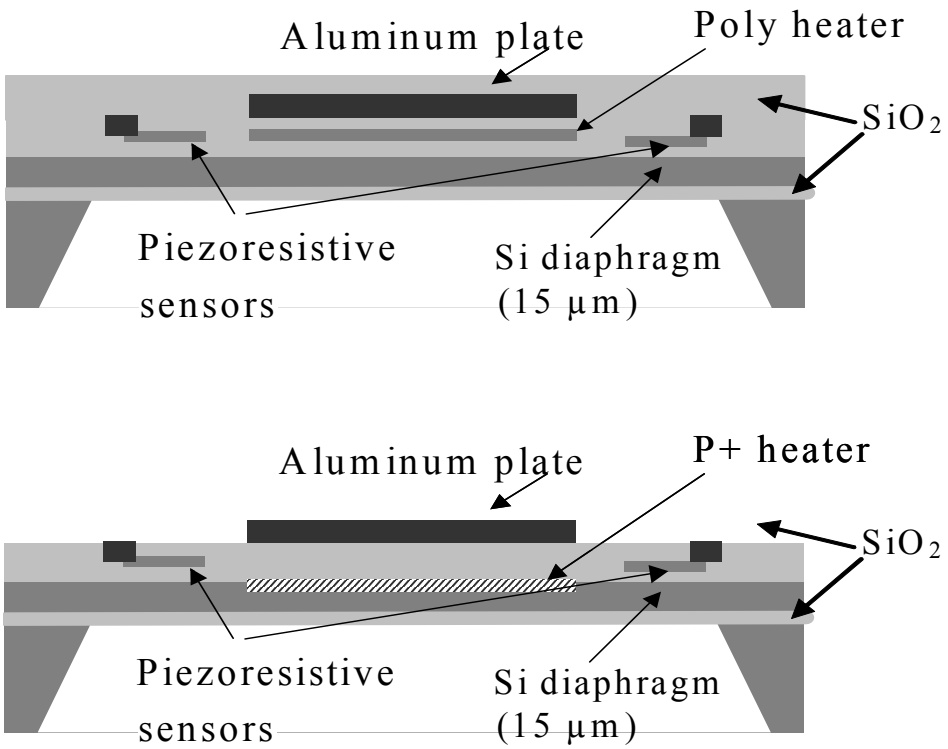

Figure 11. Cross-sectional view of the fabricated thermal actuators.

Chapter 5.

STATIC ACTUATION CHARACTERIZATION

The static behavior of the membrane to heat was fully characterized. The main purpose was to optimize the membrane thickness, the amount of metal needed for optimum bimetallic enhancement and avoid buckling which plays and important role during the vibration of the membranes. The devices studied in this chapter were all actuated with a diffused resistor and had polysilicon as the sensing elements. Other factors established during this analysis include the sensitivity calibration of the Wheatsone Bridge sensor and the analysis of the membrane temperature.

5.1 Static deflection

The static vertical displacement of the fabricated devices was measured with a Veeco Wyko NT-1100 real-time dynamic optical surface profiler. The vertical movement is first calibrated to the voltage output of the polysilicon Wheatstone bridge by increasing the applied current through the resistor and measuring the vertical movement after a settling time. The schematic representation of the test used for these measurements is shown in Figure 12. The typical output data can be seen in Figure 13. The diaphragm seems to take a parabolic shape as it deflects up from its rest position. This observation matches the temperature simulation results presented in the next section and must be taken into

account when analyzing the temperature and vertical movement of the structure experimentally.

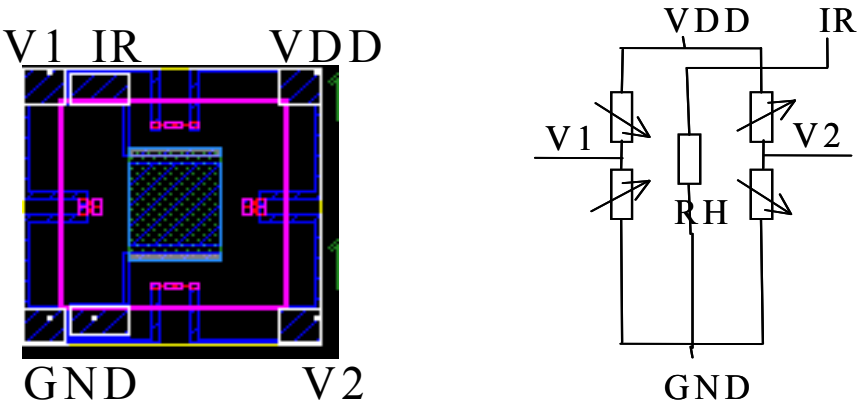

Figure 12. Schematic representation of the device circuit.

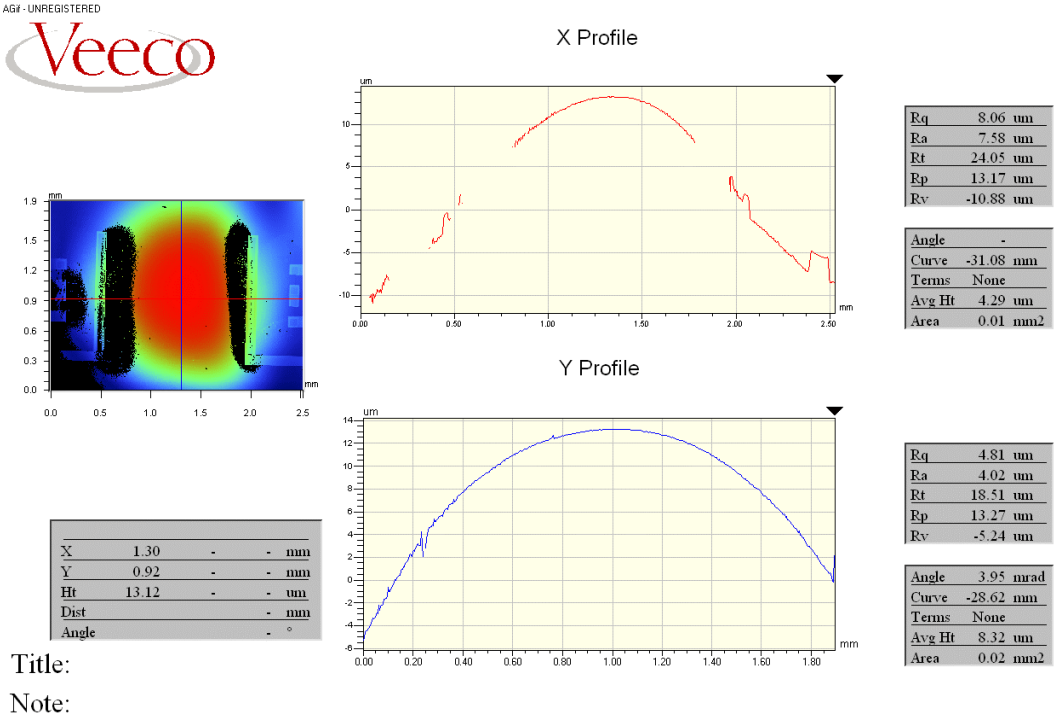

Figure 13. Typical Veeco Wyko Optical Profilometer measurement output.

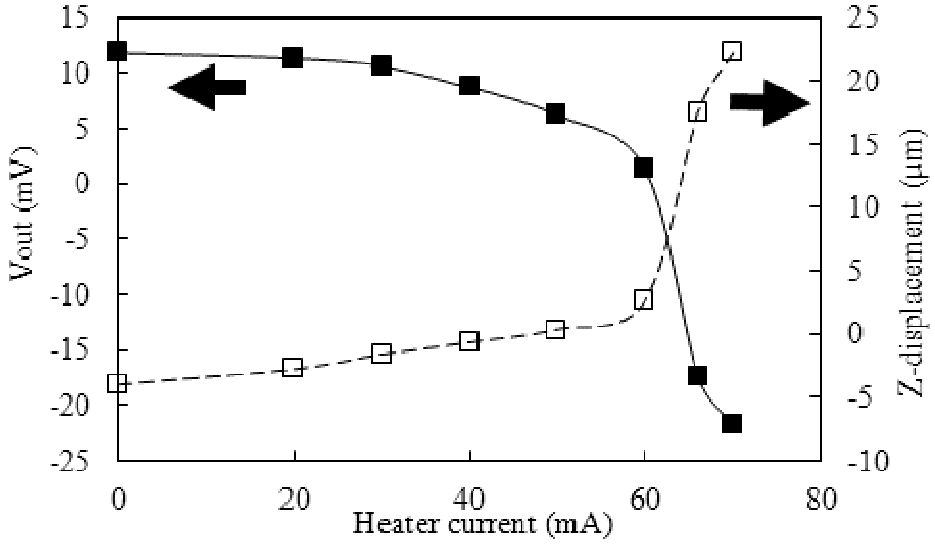

Figure 14. Calibration Results of the sensor vertical displacement with theVeeco Wyko Optical Profilometer.

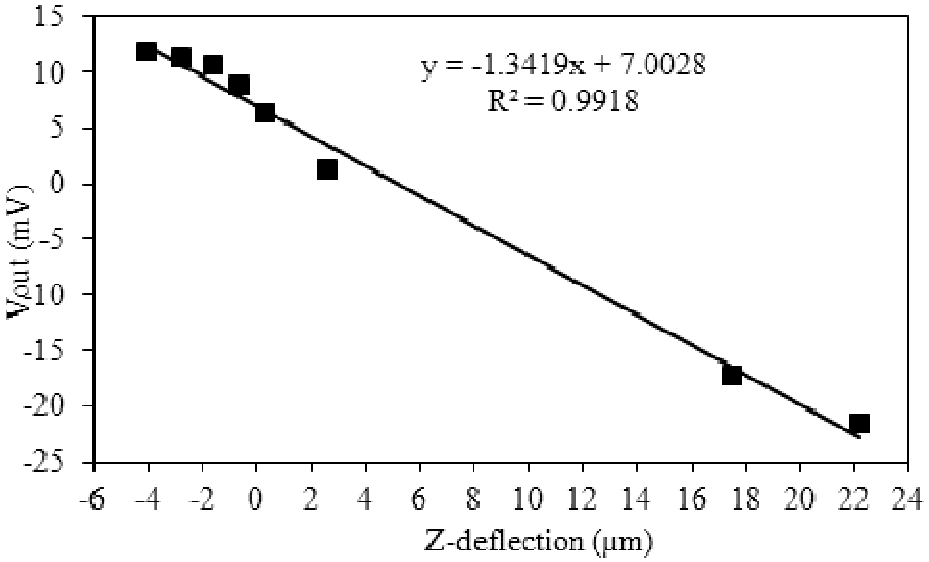

Figure 15. Sensitivity of the polysilicon Wheatsone Bridge output to the vertical movement of the diaphragm.

Figure 14 and Figure 15 show the correlation between the deflection and the voltage output. A good linear fit is obtained for a linear relationship of 1.341 mV/μm with and Rsq value of >0.9 with V_{Bridge}=5V. This sensitivity correlation allows us to measure the

vertical movement of the actuators without the need of complex and expensive optical measuring tools.

Three different Si/Al bimetal structures were fabricated with bimetallic areas of 0%, 5% and 25% in order to study the effects of the bimetal area on enhancing the vertical movement. The diaphragm thickness was also varied in order to determine the minimum thickness needed for large displacement without non-linearity or buckling effects such as those described in [62] by Brand.

The differential equation that describes the vertical motion of a thin diaphragm is presented above and repeated here:

$$D\nabla^4 w + \rho h \frac{\partial^2 w}{\partial t^2} = -\frac{\nabla^2 M_T}{1-\nu} \tag{37}$$

The closed form solution for the vertical movement y_c at the center of a simply supported thin circular plate due to a temperature differential ΔT between the bottom and the top surfaces can be approximated by the following equation given as [99]:

$$y_c = \frac{-\gamma \Delta T}{2h}\left(a^2 - r_o^2 - r_o^2(1+\upsilon)\ln\frac{a}{r_o}\right) \tag{38}$$

where γ is the temperature coefficient of expansion, υ is the Poisson's ratio of the material, h is the thickness of the plate, a is the radius of the membrane and r_o is the radius of the heating element.

The same solution can be modified to determine the vertical movement of a bimetal plate in which the thermal expansion coefficient of the two materials plays and important effect. The approximate solution is

$$y_c = \frac{6(\alpha_b - \alpha_a)(T - T_0)(h_b + h_a)(1+\nu_e)}{2t_b^2 K_{1p}}\left(a^2 - r_o^2 - r_o^2(1+\upsilon)\ln\frac{a}{r_o}\right) \quad (39)$$

where

$$K_{1p} = 4 + 6\frac{h_a}{h_b} + 4\left(\frac{h_a}{h_b}\right)^2 + \frac{E_a h_a^3(1-\nu_b)}{E_b h_b^3(1-\nu_a)} + \frac{E_b h_b(1-\nu_a)}{E_a h_a(1-\nu_b)} \quad (40)$$

and T is the temperature; T_0 is the temperature at which the diaphragm is flat; α_a and α_b are the thermal coefficient expansions of the materials (22 ppm/ºC for aluminum and 2.33 ppm/ºC for silicon), h_a and h_b are the thickness; υ_e the effective Poisson's ratio of the composite membrane ($\upsilon_e \sim \upsilon_a \sim \upsilon_b \sim 0.3$); r_o in this case is taken as the radius of the bimetal area; a is the membrane radius.

A first order approximation to the Joule heating obtained with the P+ silicon heater can be obtained by calculating the thermal resistance of the silicon diaphragm with the dimension presented in Figure 10. To simplify the analysis of this structure the temperature is assumed to be maximum and uniform across the volume of the heater. It is also assumed to be uniform across the z-axis and to decrease linearly from the edge of the resistor to the bulk silicon, which is assumed to be an ideal heat sink at room temperature. Equation 41 is used to predict the temperature of the membrane. We use the thermal conductivity of silicon k_{Si} = 1.5 W/cm°K, since the main component of the diaphragm is silicon. The length to ambient is the distance from the edge of the heating resistor to the bulk silicon, L = 500 μm and $A = W h$ varies with the cross-sectional area of the silicon membrane. Considering that the heat will dissipate in all directions at the same rate we can determine the width of this path to be the perimeter of our heater W = 4 mm. The thickness h is varied as the effect of the silicon diaphragm thickness is studied. For this approximation we did not take into account the resistance dependence on temperature of

the P+ diffused resistor. The predicted temperature is calculated for 50 mA of current through a 200 Ω resistor.

$$T = T_0 + I^2 R \frac{L}{k_{Si} A} \tag{41}$$

Table 5 TEMPERATURE INCREASE WITH A BIAS OF 0.5 WATTS ACCORDING TO EQUATION 41 AND DIMENSIONS OF FIGURE 10.

h	ΔT (0.5 W)
10 μm	41.7 °K
20 μm	20.8 °K
30 μm	13.9 °K

These temperature values are used to compute the expected vertical movement at the center of the membrane according to (38), (39) and (40) with varying bimetallic areas. The results are presented in Table 6.

Table 6 PREDICTED VERTICAL MOVEMENT WITH TEMPERATURES OF TABLE 5 AND EQUATIONS (38), (39) AND (40).

	Bimetal Area		
h	0%	5%	25%
10 μm	17 μm	30 μm	70 μm
20 μm	4.4 μm	4.1 μm	9.3 μm
30 μm	2.0 μm	1.2 μm	2.8 μm

Figure 16 shows the results of the device with 5% of bimetal area. Three distinct groups are identified with membrane thickness of <15 μm (snap-back), 15-20 μm (linear) and >20 μm (buckling). It can be observed that for devices with thinner membranes of 5 μm to 15 μm, there seems to be a rapid increase in deflection at low power levels. This buckling was observed to be a snapping effect, which is characteristic of bimetal structures and has to do with the different equilibrium shapes that develop when the

transverse loading is increased as an effect of the temperature. When the temperature is increased the first snapping action occurs, when the temperature is reduced the snap-back action takes place [100]. This effect is efficiently used in thermostats and in some MEMS applications to sense temperature changes [101]. The devices with membrane thickness between 15 µm and 20 µm show a linear relation to power at a rate of 25.5 µm / W. As the membrane thickness increases the actuator shows a similar behavior to the previous device, seemingly buckling at about 1.25 W before saturating at about 2 W. A snap-back effect is not observed for these devices with thicker membranes. These results were similar for diaphragms with no bimetal area and with a 25% of bimetal area.

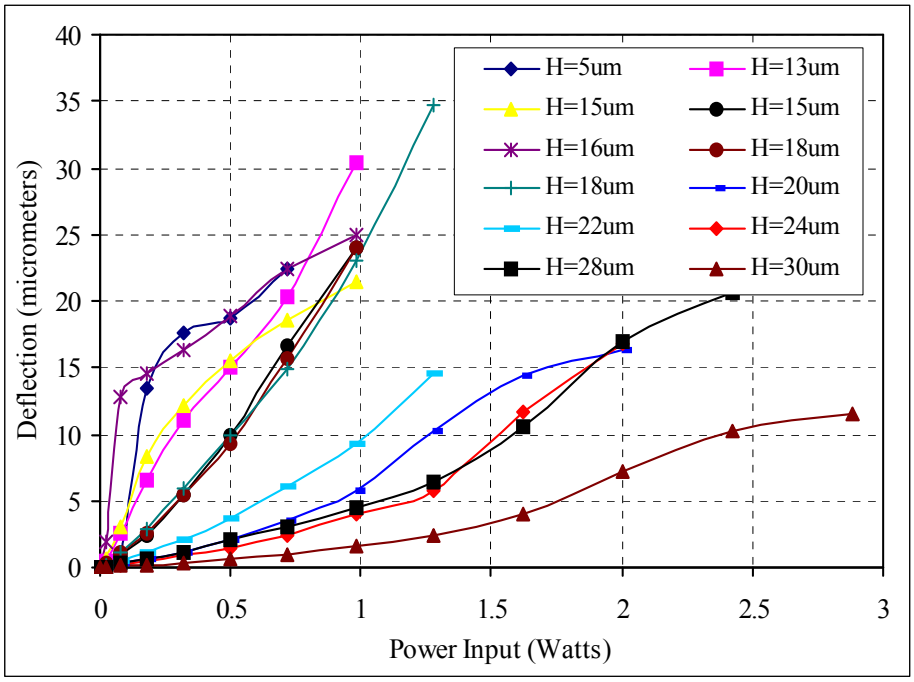

Figure 16. Thermal displacement with increasing power of devices with 5% bimetal area.

The values obtained during experimental testing match those predicted analytically in Table 6 . Table 7 presents the comparison of deflection data for a 0.5-Watt bias. Discrepancies are found for the thinner devices, which show a deflection in the same order of magnitude as the thickness of the diaphragm. This seems reasonable, as the

initial assumptions used to derive the equations are no longer valid and the device has also shown buckling and snap-back effects. Overall, the preceding equations offer good approximations to the observed experimental results.

Table 7 COMPARISON OF ANALYTICAL PREDICTION AND EXPERIMENTAL DEFLECTION DATA FOR 0.5 W BIAS.

	Bimetal Area					
	0%		5%		25%	
t	Theory	Exp	Theory	Exp	Theory	Exp
10 μm	17 μm	12 μm	30 μm	>20 μm	70 μm	<20 μm
20 μm	4.4 μm	5 μm	4.1 μm	3 μm	9.3 μm	8 μm
30 μm	2.0 μm	1 μm	1.2 μm	1 μm	2.8 μm	<1 μm

In order to choose a reliable actuator it is necessary to stay away from thin diaphragms that for the chosen temperature ranges would lead to instabilities in the structures, such as buckling or snap-back. Thus, actuators with a membrane range of 15 to 20 μm are chosen. For a square plate of dimensions 2.5 mm x 2.5 mm, this represents an ***a/h*** ratio of 166 to 125. These results coincide with the observations presented by Baltes et al in 1994 when studying the vibration behavior of thermally actuated silicon plates . For a square plate of dimensions 1 mm x 1 mm they determined that for h<6.2 μm the membranes would significantly buckle, the vibration amplitude would decrease and the resonance frequency increase. This represents an ***a/h*** ratio of 161. The bias of operation will also be kept relatively low at 0.5 Watts. According to the calculations presented above this corresponds to a temperature increase of only 15 °C to 30 °C. At this temperature range, buckling of the membrane is not expected thus preventing material fatigue and premature failure.

5.2 Membrane temperature

Since the actuation mechanism is heat it is important to monitor and understand the temperature of the diaphragm during operation. It is also important to understand the heat dissipation characteristics of the structure and the effect of the fluid on the temperature of the diaphragm. Three different types of structures have been used to monitor temperature on the diaphragm and have been compared to simulations to confirm their validity. The most appropriate monitoring structure has been used to determine the effect of fluid cooling. Using these results we have determined operating conditions where the cooling effect of the fluid is minimal and where the temperature of the membrane is raised to the same level independently of the thermal dissipation of the fluid under test.

Simulations were also performed to predict the temperature of the diaphragm for this structure. COMSOL's Multiphysics electrostatic-DC and heat conduction modules were selected. The edge of the diaphragm was set to room temperature T_0=300 K and the conduction heat generated by 50 mA of current on a 200-ohm silicon resistor was analyzed. The results of a typical simulation are shown in Figure 17. From this Figure we can observe the radial distribution of the temperature, which matches the parabolic shape of vertical displacement observed in the previous section and shown in Figure 18. Even though the heating resistor is rectangular, the shape of the temperature distribution is radial. It is also important to notice that this temperature shape also exist inside the heating resistor. Our previous assumption was that the whole heating resistor would be at a same temperature but this does not seem to hold true based on this simulation. The areas near the center of the diaphragm and further away from the heat sink are at a higher temperature even though these areas are inside the resistor.

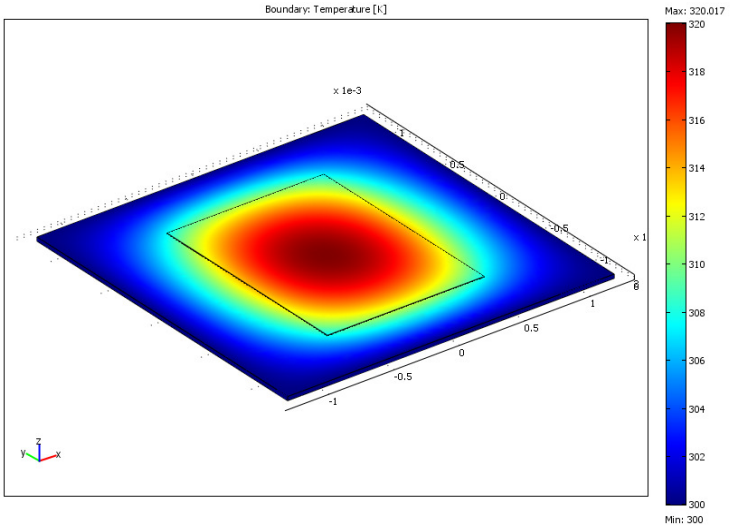

Figure 17. Temperature simulation output of a 15µm membrane with a 0.5 W bias.

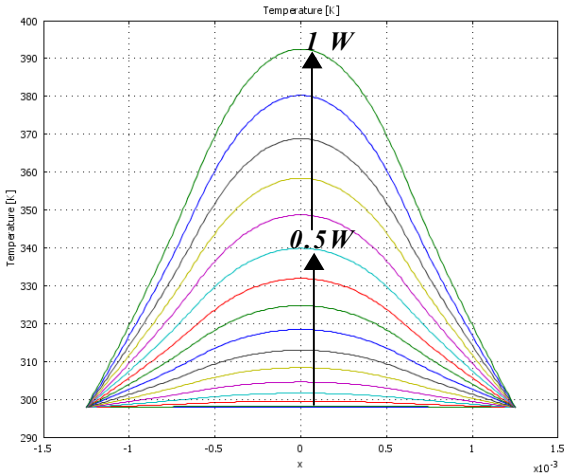

Figure 18. Temperature simulation output of 15µm membranewith increasing heater bias.

The temperature values on the surface of the membrane through x=0 is shown in Figure 18 as the power applied to the resistor is increased up to 1 Watt. The temperature increase for a 0.5 W bias is of 40 K. Using Equation 41 for a bias of 0.5 W of a 15-µm membrane the expected temperature increase would have been of 27.8 K. The discrepancy of these two predictions is due to the fact that whole resistor does not remain at the same temperature and there is actually a temperature gradient inside the resistor

itself. This temperature gradient indicates the length of the path to ambient is underestimated if we took it as the distance from the edge of the resistor to the frame of the membrane.

To experimentally determine the actual membrane temperature a forward bias PN silicon diode is used. Figure 19 shows the layout of a diaphragm with four different diodes located at different radial locations from the center of the membrane. The temperature at the center of the diaphragm cannot be measured with a diode structure. The voltage drop across the diode is temperature dependent with a negative coefficient. As temperature increases the voltage across the diode will decrease by approximately 2.2 mV / °C.

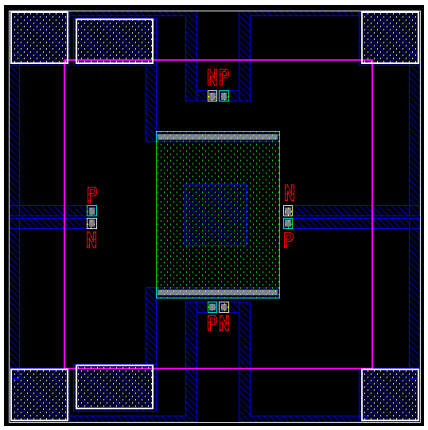

Figure 19. Temperature Diode locations on the heated membrane.

The Si diodes were calibrated using a convection oven as shown in Figure 20. The voltage drop through diode is monitored with a current bias of 0.1 mA as the temperature in the oven is increased. The results indicate a voltage drop of 2.48 mV / °C which is close to the theoretical value of 2.2 mV / °C. The differences can be attributed to the series resistance of our diodes.

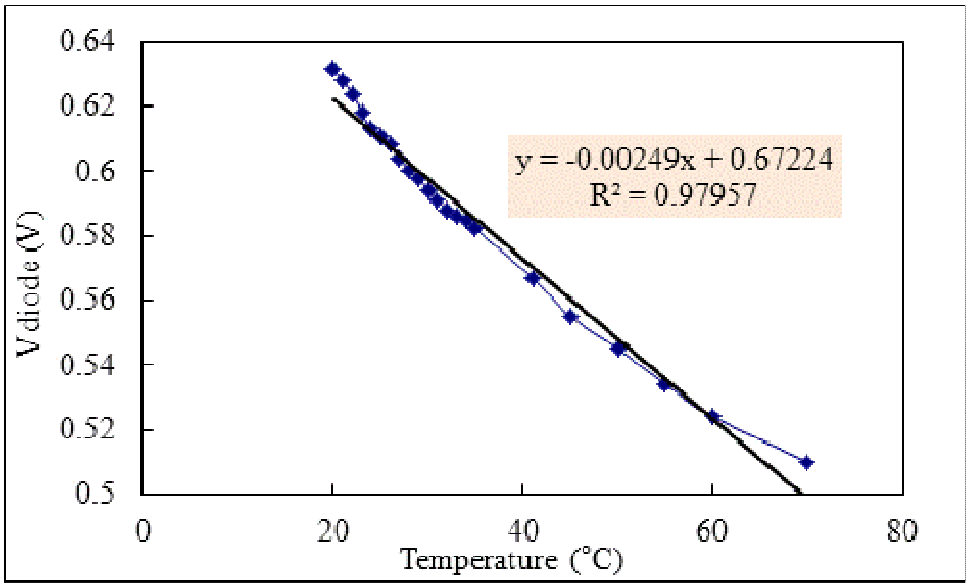

Figure 20. Calibration results of PN diode in convection oven.

Figure 21 was generated while biasing the heating resistor and monitoring the voltage of the forward bias diodes. The voltage drop was converted to temperature using the calibration shown in Figure 20. The results seem to match well those obtained during simulations if we compare the values obtained at x = 0.5 mm. We cannot compare the temperature of the center of the diaphragms, as we cannot build a PN diode in this area. With a bias of 0.5 Watt, the diodes indicate a temperature increase of 35 K at the edge of the heater (TempNEAR) while the simulations indicated a temperature increase of 30 K. On the other hand, the values obtained at the edge of the diaphragm do not seem to drop to room temperature as we expected when we set up the boundary conditions for our simulations. This assumption leads to the difference between the simulations and the measured data. It seems clear that the silicon bulk does not act as a perfect heat sink and the overall temperature of the device is higher than room temperature during operation. This is even more significant when the chip is glued to a PCB substrate for packaging, as

it will act as a heat insulator. In any case, the temperature diodes seem to be a good predictor of the temperature of the diaphragm at the locations where it is placed.

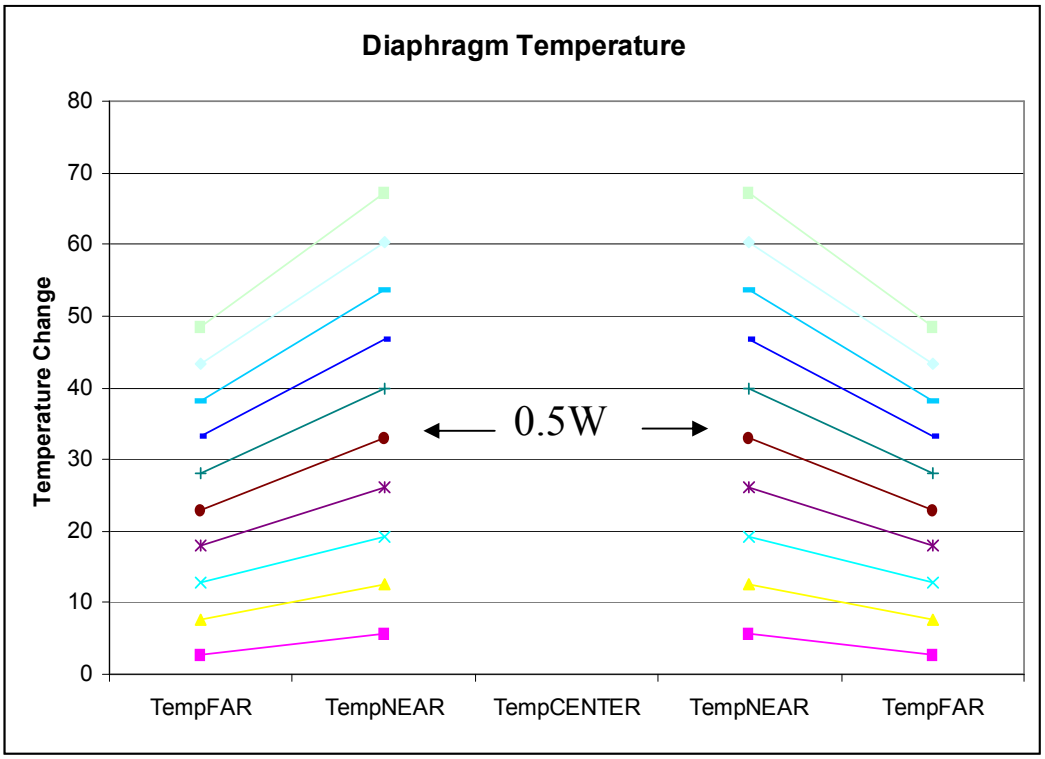

Figure 21. Measured temperature on a 15um membrane with resistive heating.

In order to quantify the effect of liquid cooling we monitored the temperature of the devices while actuating the membrane in both air and liquid. For these measurements we packaged the device by gluing and wire-bonding the chip to a PCB. This PCB is about 5cm long so that we can immerse the device into the liquid. The device PCB is connected to a signal processing PCB that contains an instrumentation amplifier with a set gain of 45 for the output of the Wheatsone Bridge and a power NMOS to control the voltage supplied to the heating resistor through a waveform generator. The schematic representation of this circuit is shown in Figure 22. A picture of the complete system inserted into the test container is shown in Figure 23. The viscosity sensor is placed at the

end of the first PCB. The second PCB is used for signal processing and amplification. The total length of the system is about 10cm.

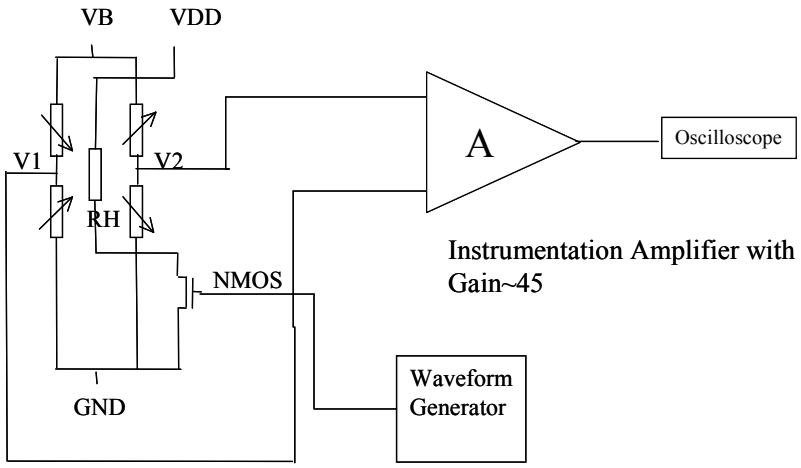

Figure 22. Test circuit for packaged devices with amplification.

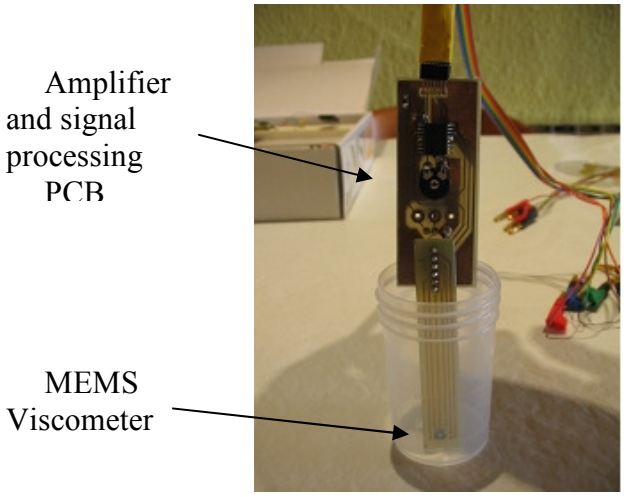

Figure 23. Picture of complete system.

The applied power to the heating resistor is controlled by the waveform generator and the VDD supply as shown in Figure 22. To avoid device damage due to excessive heating the applied power is only pulsed for a short time. To monitor the diaphragm temperature we monitor the voltage drop through the Si diodes with a 1mA bias while be pulse the heating resistor. Figure 24 shows the diode temperatures using the calibration results of Figure 21 when the device is in air and when it is immersed in oil. In this case the applied

instantaneous power to the heater is of ~ 1 Watt to maximize the signal without damaging the device. A 5 Hz signal is used. The results indicate that in air the average temperature of the diaphragm is increased to ~150 °C while in oil this temperature only increases to about 75 °C. The maximum temperature in air is ~210 °C while in oil is of only ~100 °C. This is of course going to affect the displacement of the diaphragm. The hottest the diaphragm gets, the more it will deflect. Figure 25 shows the displacement at the center of the diaphragm with the same bias conditions used when measuring the temperature. The displacement follows the temperature profiles when in air and when in the oil as expected. It is clear that the difference in displacement is due to the difference in membrane temperature and not to the viscosity or density of the fluid.

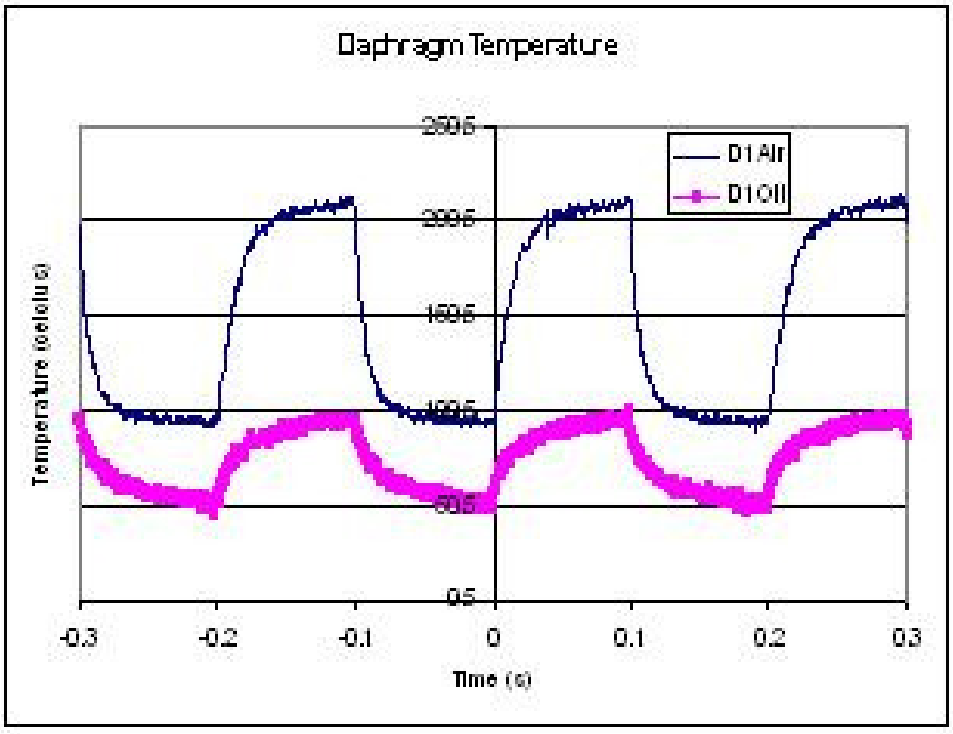

Figure 24. Temperature of diaphragm when actuated at 5Hz.

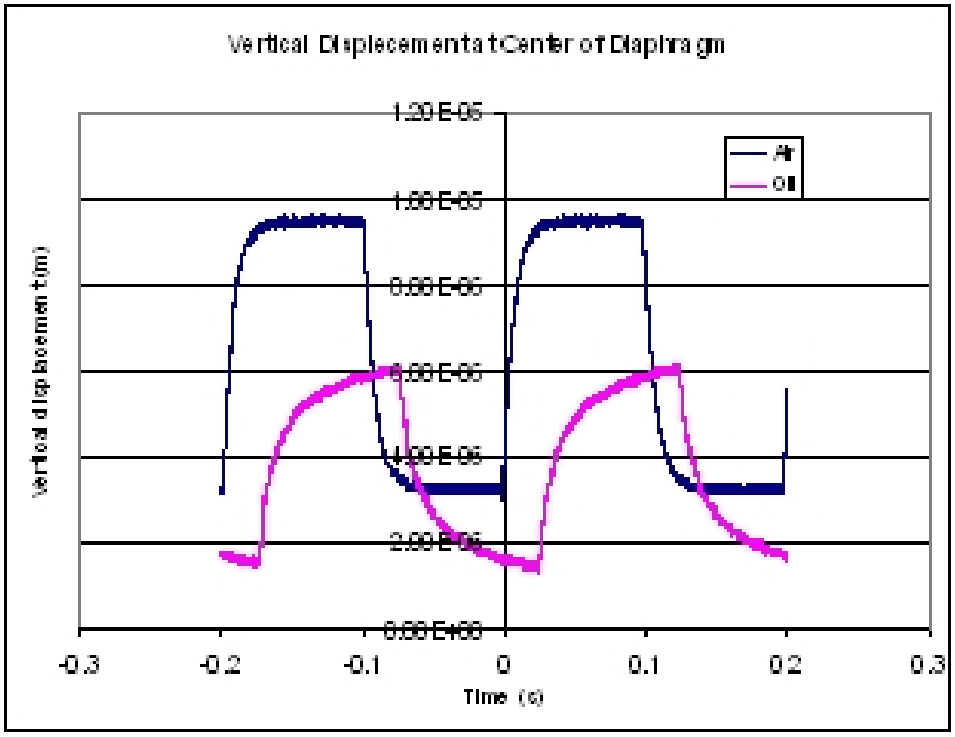

Figure 25. Vertical displacement at center of diaphragm at 5Hz.

From this analysis it becomes clear that the liquid thermal properties will affect the movement of the membrane by driving the heat away. To avoid this, the heat pulse must to be short enough so that it is not influence by the heat dissipation characteristics of the liquid [102]. Theoretically we can get an idea of the time that it takes for a heat step input to travel through the 2.5 μm of insulation SiO_2 that is on top of the Si heater. Using the one dimensional transient temperature equation – with K_{SiO2} = 0.009 cm^2/s being the thermal diffusivity of SiO_2 – for a semi-infinitely long body $x \geq 0$ [103]*:*

$$\frac{\partial T}{\partial t} = \kappa \frac{\partial^2 T}{\partial x^2} \tag{42}$$

The solution with boundary condition of $T=Ta$ on $x=0$ and $T=0$ at $t=0$ is:

$$T = T_a erfc\left(\frac{x}{2\sqrt{\kappa t}}\right) \tag{43}$$

The results are plotted on Figure 26. When the time source goes beyond 1 μsecond the temperature at the location x=2.5μm will be influenced by the heat source. This influence will be more significant when the time is beyond 10 μseconds.

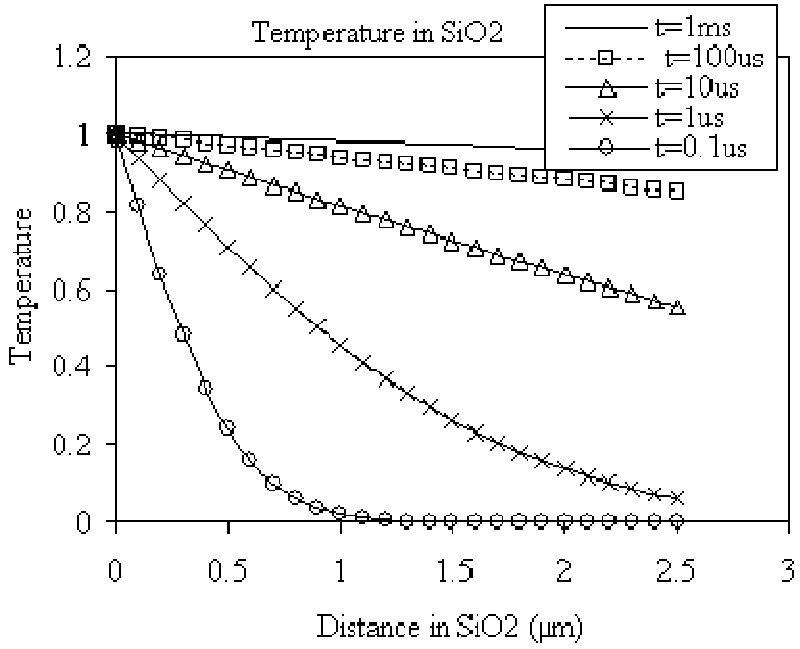

Figure 26. Temperature distribution vs. time and length for an infinitely long SiO_2 body.

Experimentally we determined the maximum pulse width value by monitoring the temperature of the diaphragm for pulses of different length. The pulse width was reduced until the difference in diaphragm temperature when immersed in air and oil becomes insignificant. The pulse amplitude voltage was increased to 30 V in order to provide enough energy to the system to results in a significant diaphragm displacement. Energy is defined as the product of power and time. As such, as we reduce time, we increase the power applied in order to keep a constant energy supplied to the system.

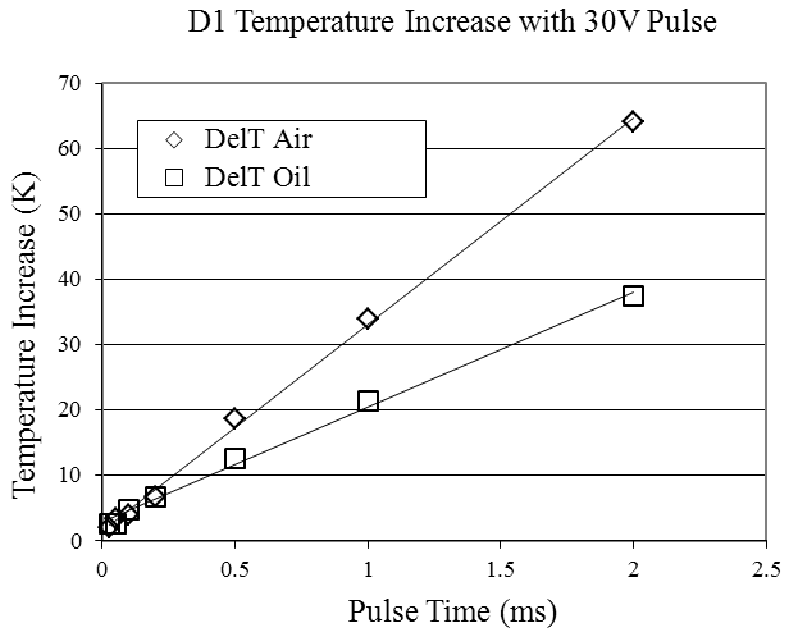

Figure 27. Temperature increase of membrane in air and oil for pulsed heating.

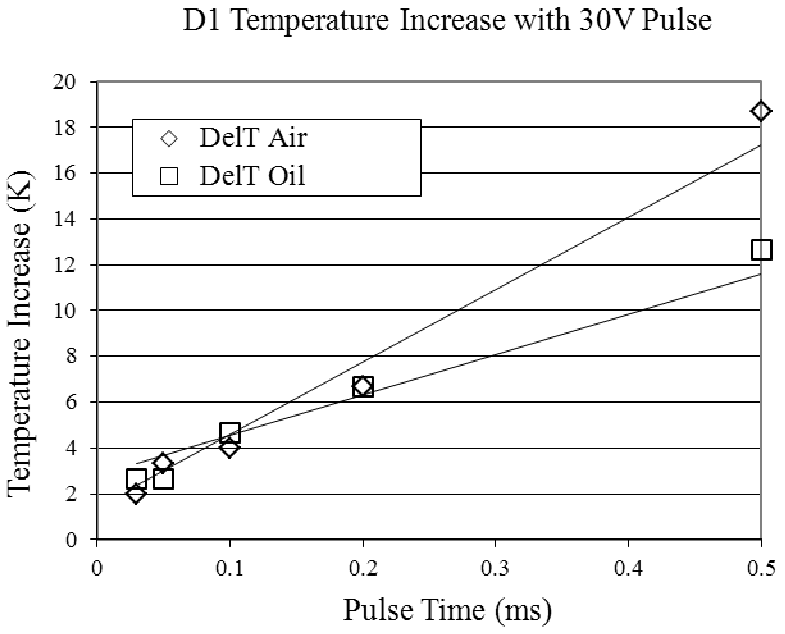

Figure 28. Detail of temperature increase of membrane in air and oil for pulsed heating < 0.5msec.

From Figure 27 and Figure 28 we observed that for a pulse of < 0.2 ms the temperature increase on the diaphragm does not seem to be influenced by the surrounding

oil when compared to air. As such, we determined that the duration of the heat pulse needed to be less than 100 μs during the testing of our devices

Chapter 6.

DYNAMIC ACTUATION CHARACTERIZATION

Based on the data obtained in the previous chapter it can be concluded that the thermal actuation needs to be less than 100 μs in duration in order to prevent heating the surrounding liquid. Within this constraint the excitation time is flexible but the excitation power needs to be adjusted so that enough energy is delivered to the membrane. Too little energy would results in no vibration. Typically, a power of 4.5 Watts was needed to produce measurable membrane displacement with polysilicon strain gauges. For p+ piezoresistors, lower actuation power was used. Typical excitation times of 20-30 microseconds resulted in the best measurable results. As such, for a 5 Hz actuation frequency, the average consumed power is 450 μW. Finite element analysis was carried out with these conditions to understand and visualize the movement of the membrane due to this sudden heat load. Finally, the vibrational movement of particular device was analyzed and characterized.

6.1 Determining pulse duration

As shown in the previous section the actuation time was kept under 100 μs to prevent heating the surrounding liquid and also to prevent structural damage. With such a short excitation time the excitation power was increased until a measurable displacement was obtained. As described in the theoretical section above the excitation energy should not

have an effect on the frequency of vibration but it will affect the amplitude and the Q value. Experimentally this was confirmed with the results of D11 presented in Figure 29. Device D11 was tested in air according to the set up presented in Figure 22. Figure 29 shows the vibration behavior obtained as the power is kept constant and the excitation time is modified. It can be observed that the most significant effect is seen on the static displacement of the membrane. The vibration amplitude increases and also the number of measurable cycles, which affects Q. The excitation time can be increased up to the 100 us limit but the effect on the static displacement is such that is difficult to measure with and oscilloscope.

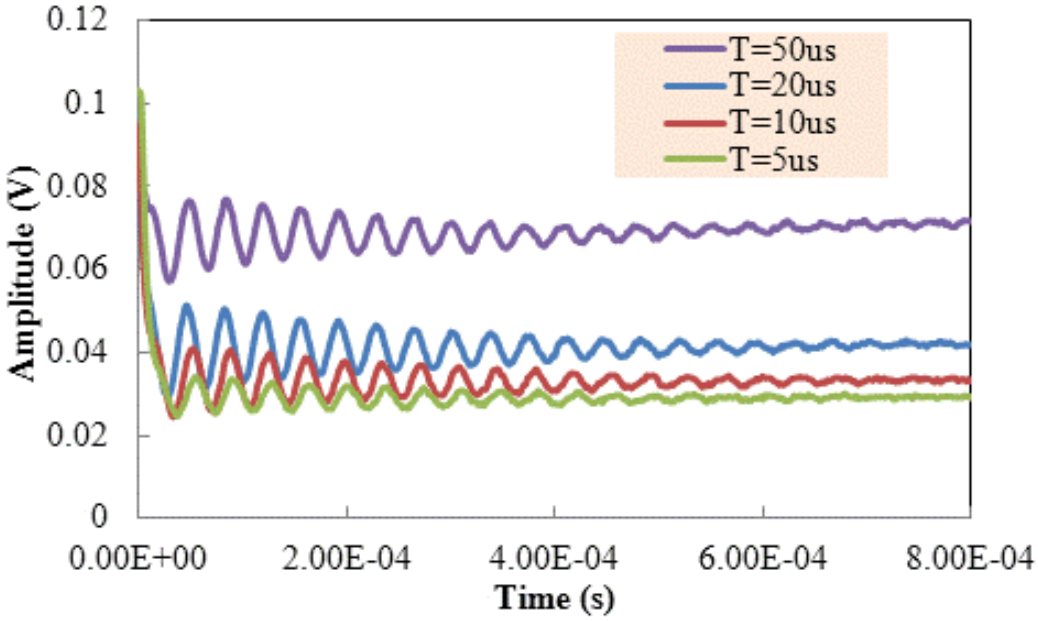

Figure 29. D11 in air with constant pulse power and increasing pulse time.

As such, the excitation energy was kept constant at 4.5 W for 20 µs for comparison purposes among devices but was changed and optimized as needed when individual devices were tested as viscosity sensors.

6.2 Finite element analysis – transient membrane dynamics

COMSOL's Multiphysics software was used to investigate the behavior of the membranes under sudden heat loads. COMSOL's Multiphysics 3D electrostatic-DC, heat conduction and stress-strain modules were selected for these simulations under a transient analysis. The results match those predicted by the theory presented in Section 2.4.2 indicating that the sudden thermal load sets the membrane in motion to vibrate at its natural frequency. Damping was not included in this simulation analysis but it is expected that intrinsic thermal damping will lead to a quick decay of the oscillations [104]. The typical energy bias applied to the membrane shows only a slight increase in temperature of the membrane, matching the measurements shown in Section 5.2. The initial response is to move either up or down, depending on the layers of materials on the membrane, and oscillate around this static displacement location. This correlates with the theory developed by Boley [92] as well as with our electrical measurements. As the heat dissipates away from the center of the membrane the membrane will tend to relax back to the starting position.

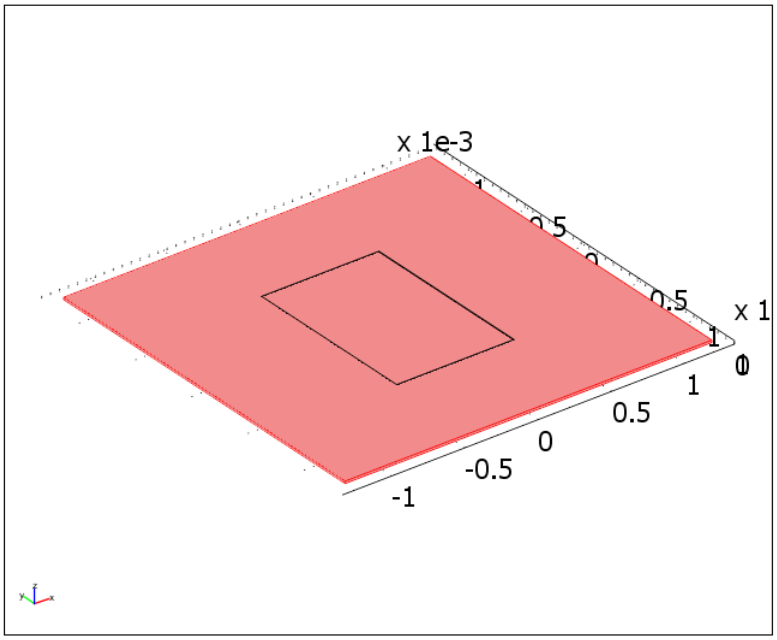

Figure 30. Silicon membrane structure simulated in COMSOL.

Figure 30 shows the simulated structure. To simplify the analysis only the silicon membrane is simulated. The simulation requires vast computing resources as the aspect ratio of the layers leads to mesh elements of the same range as those layers. As such, we were not able to simulate the oxide layers or the aluminum layers. Figure 31 shows a typical mesh of the simulated structure with over 76,000 elements. The silicon membrane is simply supported at all edges. Typical bulk properties of silicon, as those listed in Table 4 are used.

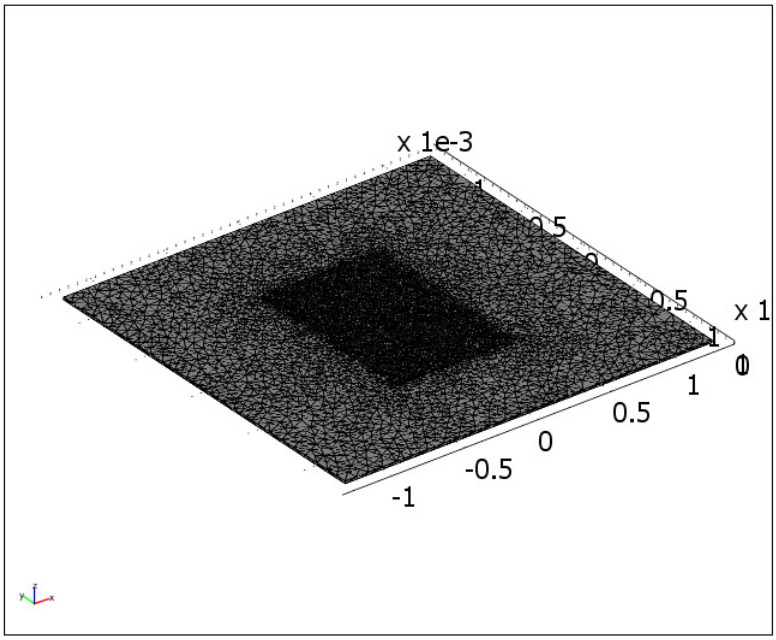

Figure 31. Meshed silicon membrane structure simulated in COMSOL.

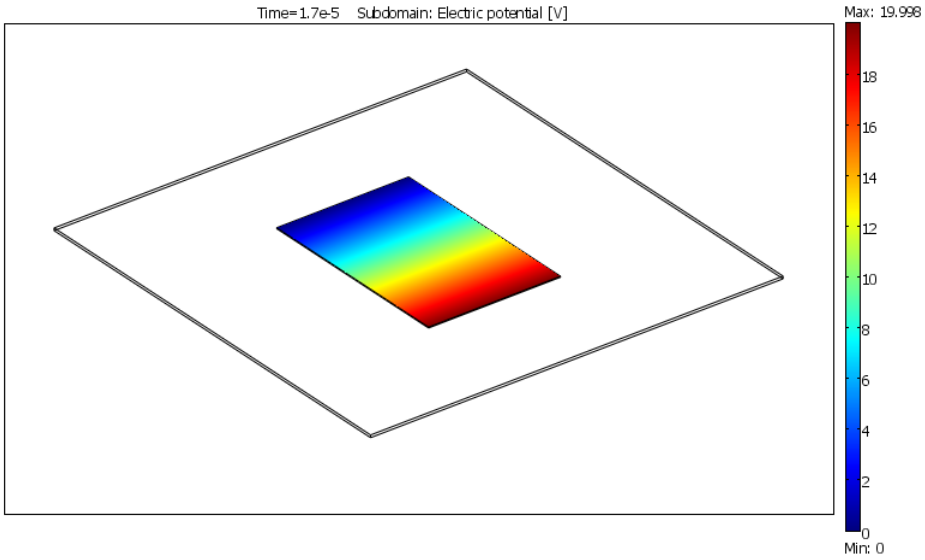

Figure 32. DC simulation output at 17.5 microseconds showing a 20V potential difference across the heating resistor.

The electrostatic-DC simulation is performed by defining a silicon heating resistor in the middle of the membrane as the outlined rectangle in Figure 30. This region is

embedded in the 15 µm silicon membrane occupying a volume of 1.2 mm x 0.8 mm x 5 µm and is defined as having a sheet resistance of 100 ohms/sq. The remaining silicon region excluded from this part of the simulation so as to confine the current flow to the heater volume. A 20 V bias is ramped at one end of the resistor in 5 microseconds and left on for 20 microseconds before it is removed. The results shown in Figure 32 are taken at t = 17.5 microseconds and it shows the 20V potential across the heating resistor. Solutions are obtained at 0.5 microsecond increments.

The heat conduction section of the simulation is then performed at each of the transient step solutions. Joule heating results in a temperature increase at the center of the membrane as shown in Figure 33. The temperature increase due to the current bias conditions, 20 V for 20 µs, is of only 3.5 ºC. This confirms the measurements taken with the in-situ diodes presented in Section 5.2. This peak temperature is reached in 35 microseconds, 10 microseconds after the heating bias has been removed. The temperature will then decay slowly down to room temperature.

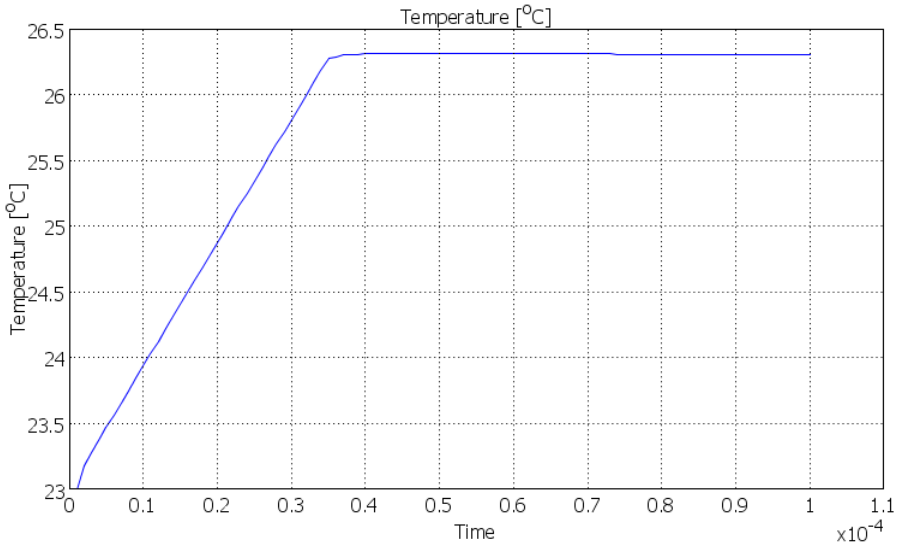

Figure 33. Temperature increase over time at the center of the membrane.

The temperature distribution of the membrane near its peak temperature is show in Figure 34. It can be observed that the temperature distribution is highest at the center of the membrane and follows approximately the same shape of the heating resistor and becoming more circular in shape as the heat leaves this region.

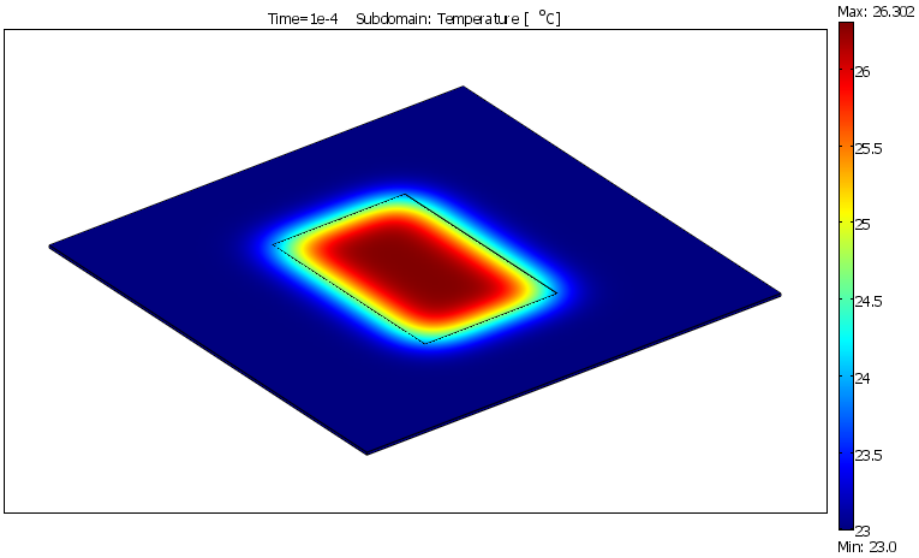

Figure 34. Temperature distribution of the membrane.

The last part of the simulation is to perform the stress-strain analysis of the membrane with the results obtained at each of the transient steps. Figure 35 shows the transient displacement of the center of the membrane. As predicted by the theory and observed in the experimental data, the membrane will experience a static displacement and a dynamic displacement. The static displacement is lower than that predicted by the theory presented in Section 2.4.2 but matches what is observed experimentally. This dynamic displacement value of ~ 100 nm around the static displacement matches both the theoretical and experimental results. The period of the oscillation is 46 μs, a frequency of 21,739 Hz, which is the natural frequency of vibration of this membrane structure. Thus,

confirming that the inertia given to the membrane through the burst of heat will set the membrane to mechanically oscillate at its natural frequency.

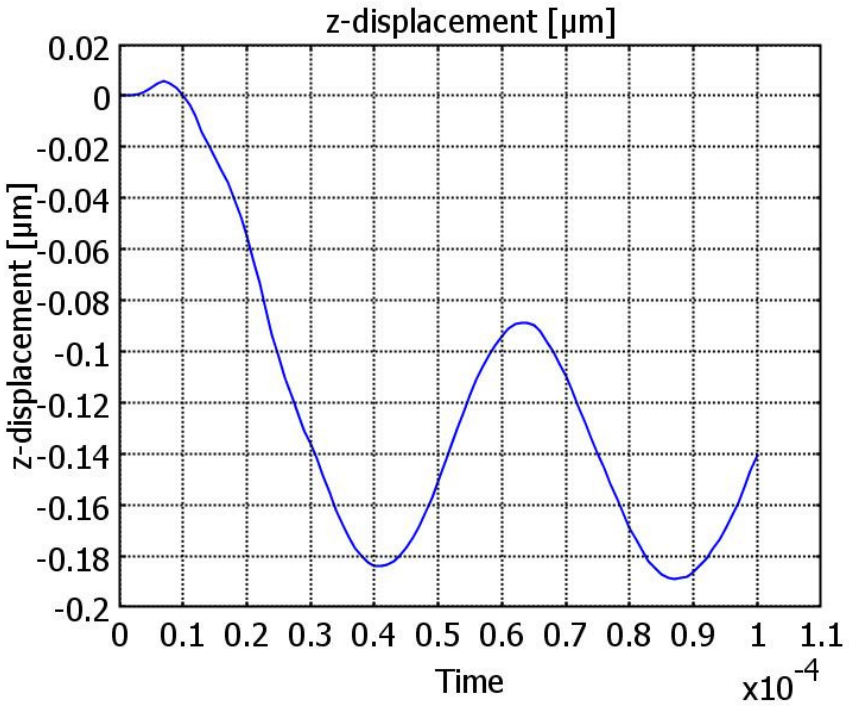

Figure 35. Membrane response to a 20 V – 20 µs pulse of a 2.5 mm silicon membrane with a p+-diffused heater.

The shape of the membrane during this oscillation is important in order to determine its coupling with the fluid being tested. As seen in Figure 36, the deformation shape does not follow the shape of the heater. Instead, it takes a circular shape due to the boundary constraints of the simply supported square diaphragm. As such, it is important to conclude that the shape of the membrane will be assumed to be the same independently of the size and shape of the heater.

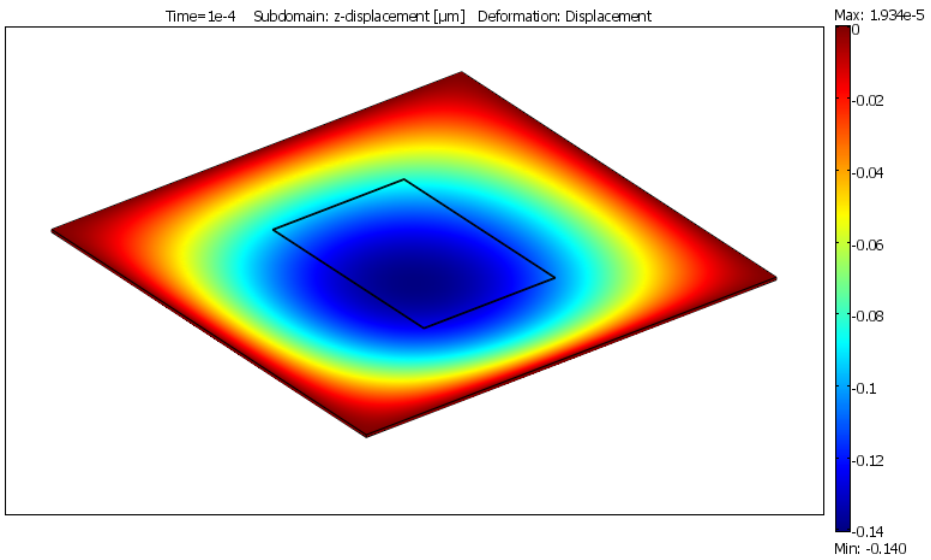

Figure 36. Membrane deformation in response to a 20 V – 20 µs pulse of a 2.5 mm silicon membrane with a p+-diffused heater.

6.3 Dynamic Measurements

The natural frequency of vibration of a simply supported square thin plate can be calculated using the following well-known equation [105]:

$$f = \frac{19.74}{2\pi a^2}\left[\frac{Eh^3}{12\rho h\left(1-\nu^2\right)}\right]^{1/2} \tag{44}$$

where $\boldsymbol{E}$ is the Young's modulus of the material, $\boldsymbol{a}$ is the length of plate, $\boldsymbol{h}$ its thickness, $\boldsymbol{\rho}$ its density and $\boldsymbol{\nu}$ its Poisson's ratio.

The typical silicon diaphragm structures used in this study have a selected diaphragm thickness of $\boldsymbol{h}$ = 15 µm and a side length $\boldsymbol{a}$ = 2.5 mm. These dimensions have been chosen to ensure linear behavior as explained in the sections above. The expected natural frequency using the nominal values listed in Table 8 is $\boldsymbol{f_{vacuum}}$ = 20,604 Hz.

Table 8 NOMINAL VALUES FOR CALCULATING NATURAL FREQUENCY OF PLATE [106].

Si Young's Modulus ***E***	Si Poisson's ratio ν	Si density ρ	Height of plate ***h***	Length of plate ***a***
190 GPa	0.3	2330 kg/m^3	$15x10^{-6}$ m	$2.5x10^{-3}$ m

This theoretical value for the natural vibration will vary significantly due to important uncertainties found in these devices. The mechanical properties will vary due to the fact that our devices contain a 1 μm of SiO_2 for electrical and thermal isolation as well as 1-μm aluminum traces for electrical connections. Furthermore, certain degree of uncertainty already exists when using bulk material values in MEMS structures [102, 103]. There is also uncertainty of the fabricated geometrical characteristics of the device. The thickness of the plate could very across its length depending on the smoothness of surface crated by the KOH etch, which will depend on the temperature and concentration of the chemistry. The thickness of the plate cannot be measured without destroying the device, and even then its uniformity is difficult to measure throughout the area of the plate. The length of the plate will also vary slightly depending on the etch time and the thickness of the starting substrate. All these uncertainty leads to a large range of expected values for natural frequencies. The effect and possible causes for the variation in natural frequencies are summarized in Table 9 .

Table 9 VARIATION OF CHARACTERISTIC PARAMETERS AFFECTING THE NATURAL FREQUENCY [107], [108].

	Si Young's Modulus E	Si Poisson's ratio ν	Si density ρ	Height of plate h	Length of plate a
Range	62 – 202 GPa	0.22-0.3	2330 kg/m^3	14-15 μm	2.4-2.6 mm
% to nominal	6% to 60%	25 %	-	6 %	5 %
Source of Variation	Crystal orientation Doping Materials	Crystal orientation Doping Materials	-	KOH etch time	Substrate thickness
Scaling effect	$K^{1/2}$	$(1-K^2)^{-1/2}$	$K^{-1/2}$	K	K^{-2}

Three different devices were experimentally measured using the test circuit configuration shown in Figure 22. The estimated diaphragm thickness for all three devices is of 15 μm. As described in the previous sections a 30 μs pulse is applied to the plate heater in order to set the membrane to vibrate at its natural frequency. The deflection of the membrane is measured with the Wheatstone bridge and amplified through an instrumentation amplifier. The output of device 1P is shown in Figure 29. The natural frequency of vibration can be directly extracted from this output by measuring the period of the oscillations. The measured natural frequencies of three different devices are presented in Table 10 . These values fall within the expected theoretical range.

Table 10 NATURAL FREQUENCIES OF THREE DEVICES.

Device	Natural frequency	Variation
1P	19200 Hz	0.6mm Al plate on top
2	15640 Hz	1.2mm Al plate on top
2H	14000 Hz	Si only

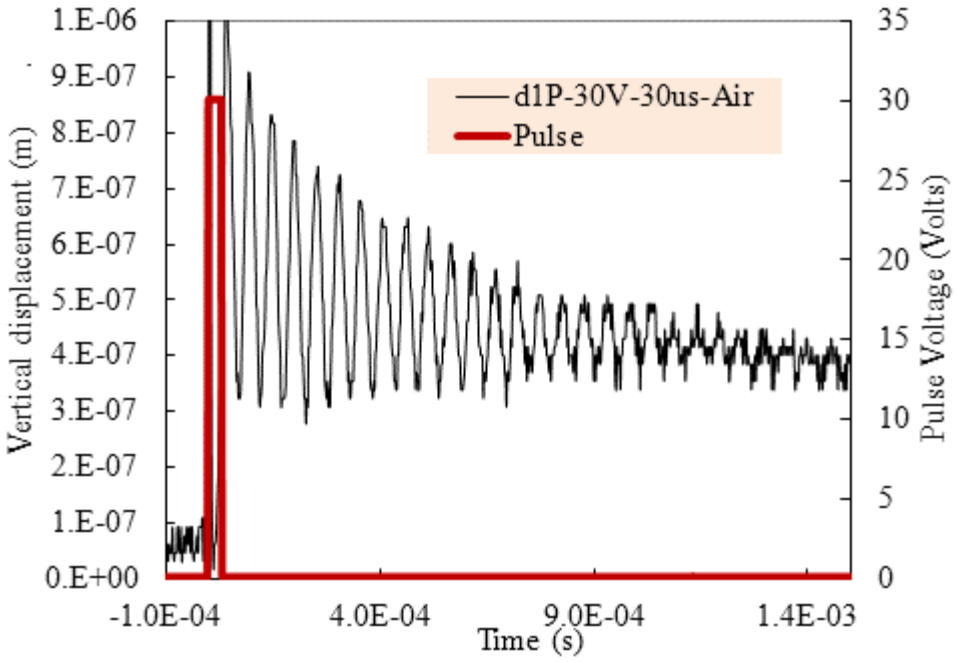

Figure 37. Natural frequency vibration in air of device 1P with a 30V-30µs pulse.

The vibrations and decay of Figure 37 can be analyzed using the damped free vibration model of a simple harmonic oscillator. The equation used to describe this model is

$$y(t) = Ae^{-\zeta\omega_n t}\cos(\omega_d t - \phi_c) \tag{45}$$

where ω_n is the circular natural frequency, ω_d is the damped natural circular frequency and ζ is the damping ratio. The damped natural circular frequency and the damping ratio are defined as

$$\omega_d = \omega_n\sqrt{1-\zeta^2} \tag{46}$$

$$\zeta = \frac{\delta}{\sqrt{(2\pi)^2 + \delta^2}} \tag{47}$$

where δ is the logarithmic decrement and can be measured from plot 31 by taking the displacement values y_1 and y_2 at two successive peaks.

$$\delta = \ln\left(\frac{y_1}{y_2}\right) \tag{48}$$

Device 1P can be fitted to the following model equation:

$$y(t) = 3\times10^{-7} e^{-9.25\times10^{-3}*122527t} \cos(122522t - 0.2\pi) \tag{49}$$

The quality factor Q of an oscillator is defined to be the energy stored in the oscillator divided by the energy lost in a single oscillation period. The simplest method to obtain this value is to measure the number of oscillations before its amplitude becomes insignificant. From Figure 29, Q~20 for device P1. Another method, which will be used from here on, is to perform a Fast Fourier Transform of the signal and fitting a normal distribution curve. Q is then calculated as the ratio of the peak frequency and the width at ½ of maximum as shown in Figure 38 for device 1P.

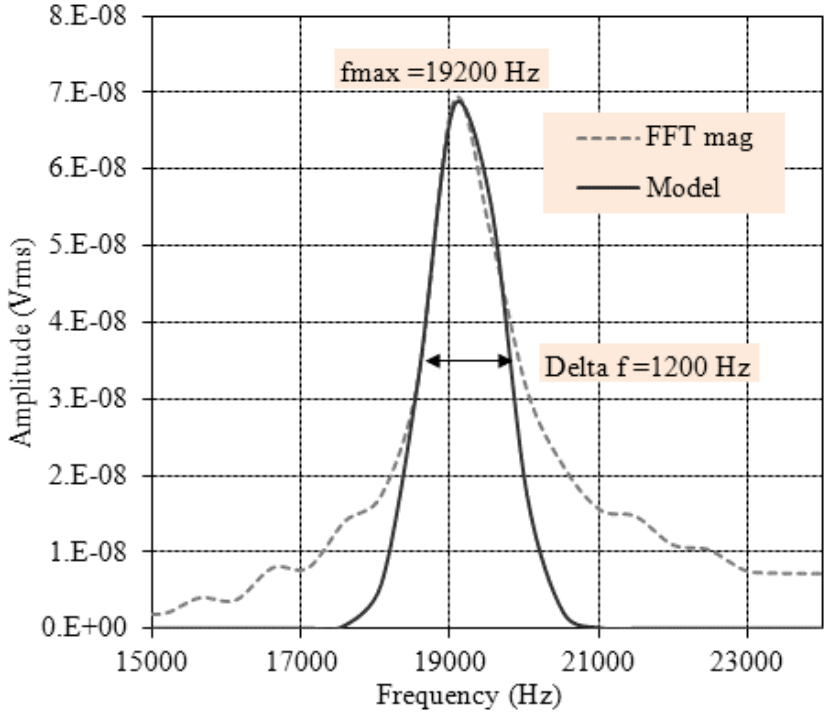

Figure 38. FFT for device 1P. Calculating Q.

The Q values of the three devices tested are presented in Table 11 . It is important to note that device 2H shows a much lower Q value due to the fact that a top aluminum metal is not utilized and the amplitude of vibration seems to be smaller and dissipate faster.

Table 11 NATURAL FREQUENCY AND Q OF RESONATORS.

Device	Natural frequency	Q	Variation
1P	19200 Hz	16	5 % Al plate on top
2	15640 Hz	18.4	25% Al plate on top
2H	17500 Hz	3.5	Si only

Chapter 8.

DEVICE OPTIMIZATION

Based on the result from the previous section and keeping the ***a/h*** ratio consistent at 166, we studied the reduction of both the thickness and the length of the diaphragm in order to obtain a much-compacted device that will suffer from less uniformity issues. With the objective to more effectively actuate the device, we studied the type of heater, the reduction of its size and power while maintaining a similar temperature of actuation.

Simulations were performed that showed that a smaller size resistor will result in a higher temperature gradient for a given power of actuation.

The use of aluminum for bimetal actuation enhancement was also evaluated by direct comparison. An additional layer of SiO_2 passivation was also be added to the final structure in order to further isolate the device from the liquid temperature.

The fabrication variables were designed using a full factorial method and analyzed for the dynamic behavior including frequency, amplitude and Q. The results indicate that the addition of materials results in a higher frequency of vibration, the polysilicon resistor enhances the amplitude of vibration but decreases the quality factor and the addition of a bimetal layer has only a minimal effect

7.1 Experimental design

Table 1 presents the design of experiment (DOE) performed for this study. SOI wafers with silicon thicknesses of 15 μm, 10 μm and 7 μm were purchased in order to

accurately obtain the desired membrane thickness. Only the devices with the targeted membrane thickness and length were targeted to be tested in each wafer (ie. ***h*** = 15 μm and ***a*** = 2.5 mm, ***h*** = 10 μm and ***a*** = 1.75 mm, ***h*** = 6 μm and ***a*** = 1 mm.)The variables are: silicon thickness ***h***, length of membrane ***a***, heater material Heater, resistor size Rsize, passivation Pass and bimetal Metal. All these variations can be effectively accomplished with just 3 wafers. By designing the proposed device geometry and material variations on each wafer we only need to vary the diaphragm thickness. This is shown in Figure 39 where the length of the membrane, the resistor type and its size is varied through the 5x5 matrix. Figure 40 shows how the passivation and metal options are included to the wafer design. The factors to study are vibration frequency Fo, quality factor Q and maximum amplitude of the oscillation Amp.

TABLE 13 DOE INCLUDED IN EACH TARGETED A/H COMBINATION.

Heater	Rsize	Pass	Metal
P+	36%	NO	NO
P+	36%	NO	YES
P+	36%	YES	NO
P+	36%	YES	YES
P+	16%	NO	NO
P+	16%	NO	YES
P+	16%	YES	NO
P+	16%	YES	YES
P+	2%	NO	NO
P+	2%	NO	YES
P+	2%	YES	NO
P+	2%	YES	YES
POLY	36%	NO	NO
POLY	36%	NO	YES
POLY	36%	YES	NO
POLY	36%	YES	YES
POLY	16%	NO	NO
POLY	16%	NO	YES
POLY	16%	YES	NO
POLY	16%	YES	YES
POLY	2%	NO	NO
POLY	2%	NO	YES
POLY	2%	YES	NO
POLY	2%	YES	YES

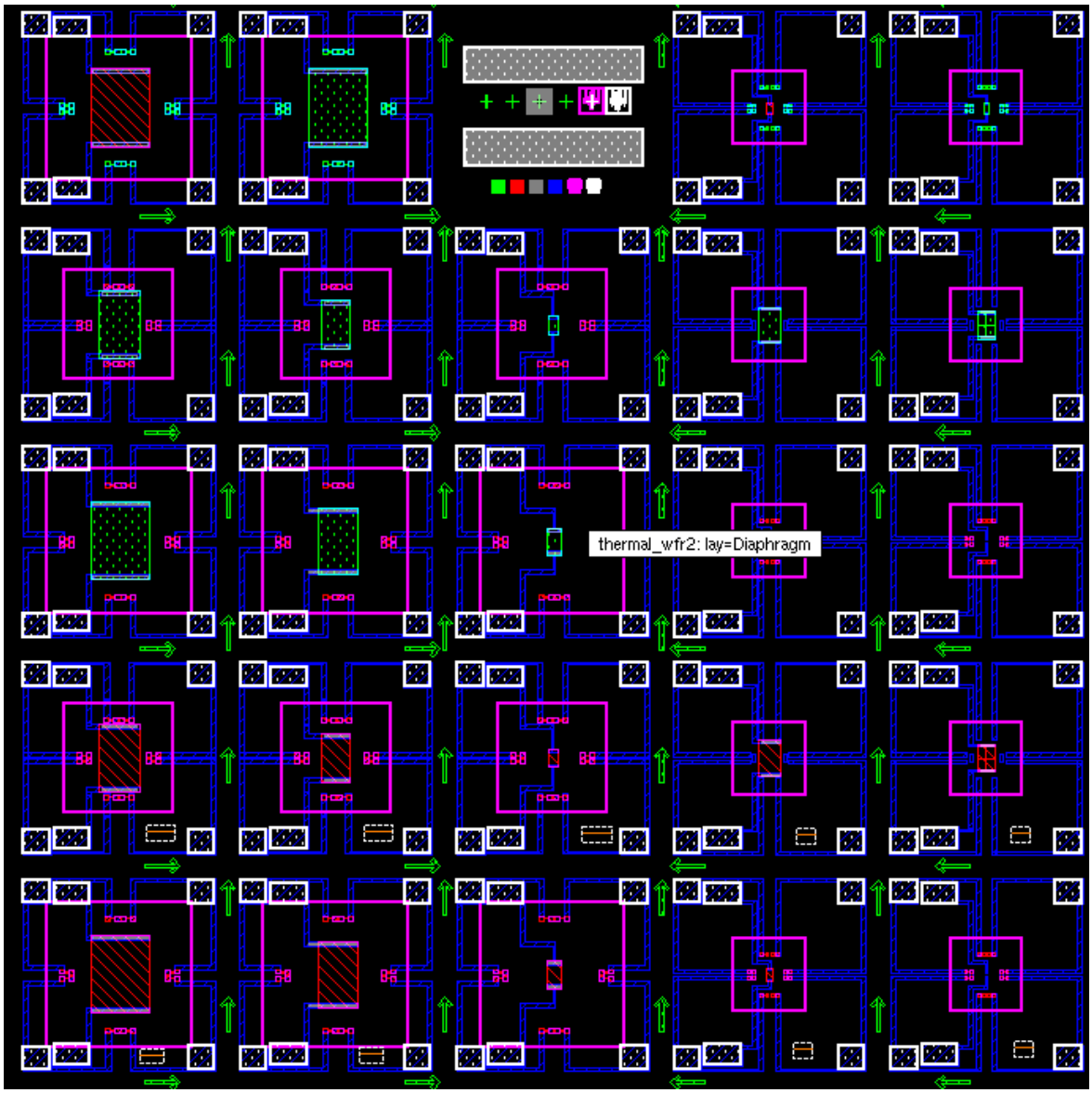

Figure 39. 5 x 5 die matrix showing variations in membrane (pink) length ***a*** **(**2.5 mm, 1.75 mm and 1mm), heater material (Poly (red) or P+ (green)) and size of heater (2%, 16% or 35% of membrane area).

Most of the analysis was carried out with the 15-µm-wafers and the devices with a membrane length of 2.5 mm. Even though these devices are the largest they are the easiest to handle during fabrication and test. Wafers with thinner membranes result in very weak membranes that are prone to breakage. The results obtained with these 2.5 mm

devices correlated to the thinner ones. A smaller number of devices with thinner membranes were tested to confirm the results obtained with the larger ones.

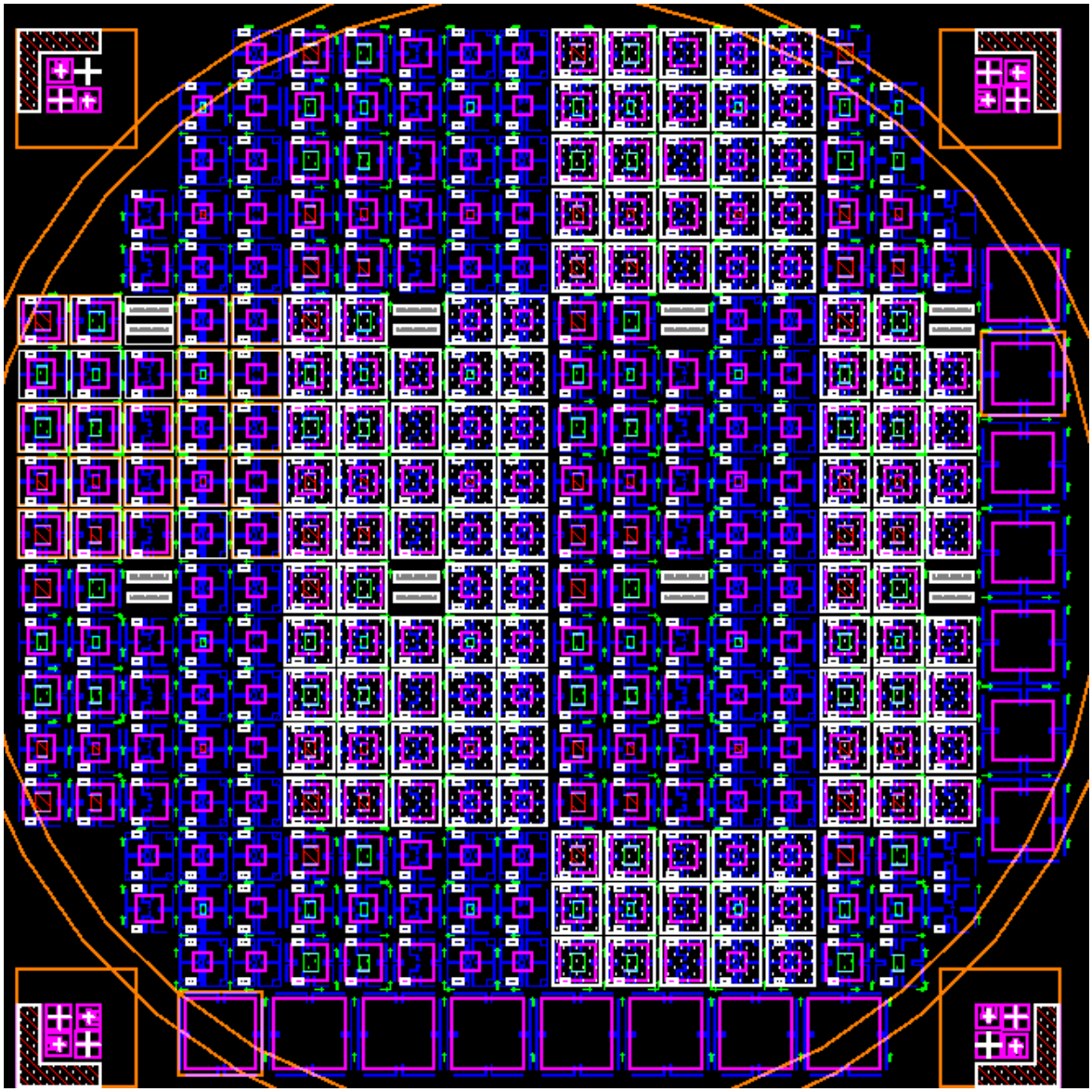

Figure 40. Wafer layout showing the 5x5 die matrix repeated with varitions on passivation and metal.

7.2 Static measurements

The fabrication details have been presented in Section 5.1 and the Appendix. Fabrication was undertaken in the Semiconductor and Microsystems Fabrication

Laboratory at Rochester Institute of Technology. The most significant devices were inspected as fabricated to have an understanding of their as-fabricated characteristics. The most significant differences were expected to be seen between the design with a p+-diffused heater and the designs with the poly heater. This determined the intrinsic stress of the membrane and was used when analyzing the dynamic behavior of the devices when immersed in fluid during the viscosity measurements. Veeco's Wyko NT-1100 real-time dynamic optical surface profiler was used for this purpose.

Figure 41 shows the 3D representation of the shows the surface profile of a device with a p+-diffused heater. 4D14 is a device with a 35% p+-diffused heater, no passivation and 5% metal plate. Figure 42 shows that the intrinsic fabrication stress leads to an initial deformation of -12 µm at the center of the 2.5 mm membrane.

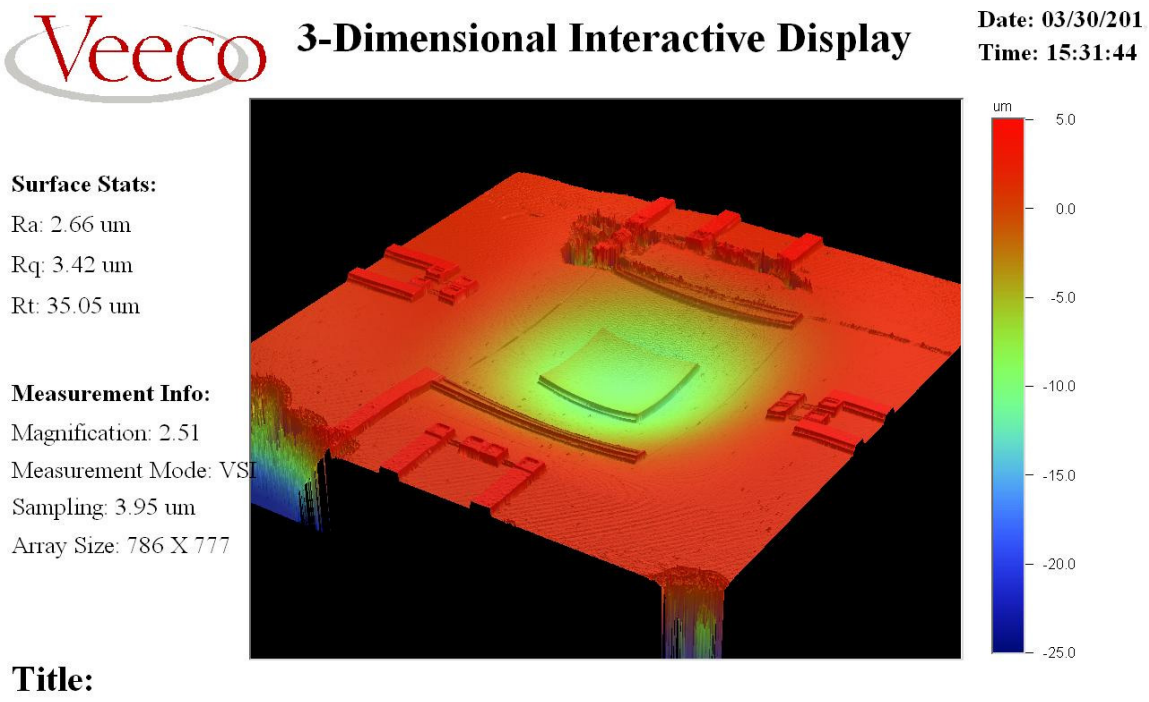

Figure 41. Veeco's 3D ouput of the surface profile of device 4D14 with a p+-diffussed heater, no passivaiton and a metal plate.

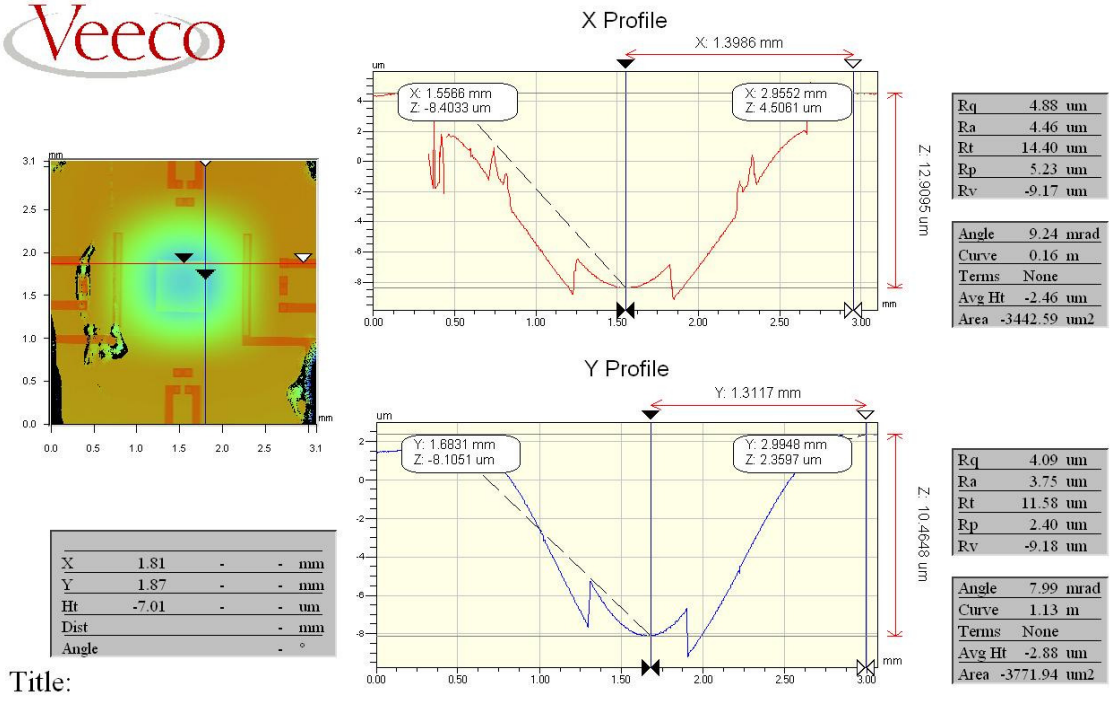

Figure 42. Veeco's 2D ouput of the surface profile of device 4D14 with a p+-diffussed heater, no passivaiton and a metal plate. The intrinsic fabrication stress leads to a -12 µm deformation at the center of the 2.5 mm membrane.

Figure 43 and Figure 44 shows the contrasting results of a device with a 35% poly heater, no passivation and a 5% metal plate. In this case, the intrinsic stress results on the membrane bending up by +10 µm. This is mainly due to the presence of polysilicon. The presence of metal seems to have little effect on the intrinsic stress.

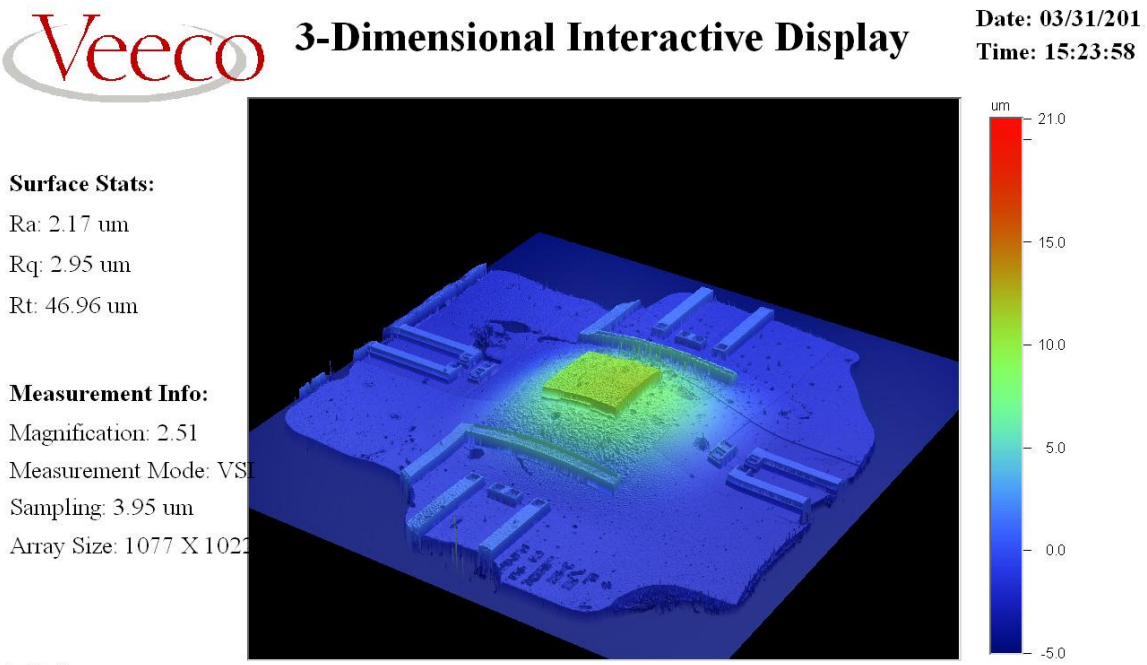

Figure 43. Veeco's 3D ouput of the surface profile of device 4D6 with a polysilicon ater, no passivaiton and a metal plate.

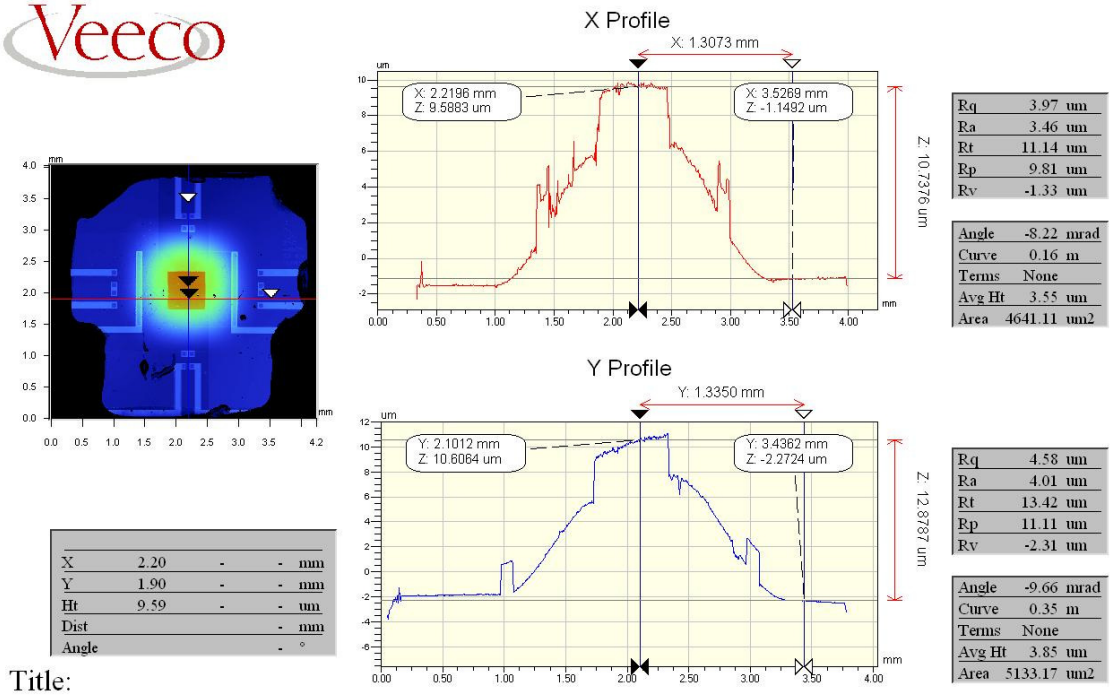

Figure 44. Veeco's 2D ouput of the surface profile of device 4D6 with a polysilicon heater, no passivaiton and a metal plate. The intrinsic fabrication stress leads to a +10 µm deformation at the center of the 2.5 mm membrane.

Table 13 summarizes the type of device inspected and the amount of center deflection as fabricated. It can be concluded from this data that the main factor affecting the intrinsic stress is the heater material and size. P+-diffused heaters bend the membrane down by approximately 10 μm. On the other hand, polysilicon heaters bent the diaphragms upwards by about the same amount. When this polysilicon heater is small, the diaphragm will remain down as with the devices with the p+-diffused heater. The presence of passivation and metal seem to have a slight effect but much less important than that of the heater material and size.

Table 13 INSTRINSIC CENTER DEFLECTION OF 2.5 MM DIAPHRAGMS WITH VARIED HEATER MATERIALS AND SIZES.

Device	Heater	Size	Passivation	Metal	Deflection (μm)
4D14	P+	35%	Yes	Yes	-12.9
D22	Poly	2%	Yes	Yes	-9
D11	P+	16%	Yes	Yes	-7.6
4D24	Poly	35%	No	No	7.3
D51	Poly	35%	No	No	10
4D16	Poly	16%	Yes	No	10.7
4D6	Poly	35%	Yes	Yes	11

7.3 Heating the membrane

This section examines the behavior of the membrane with reference to their intrinsic stress as it is heated. The two devices presented in the previous section were heated using the in-situ heater while the surface profile was obtained. The deflections obtained indicate that the membrane that is originally bent down will bent downwards even more as heated. When the membrane is originally up, it will bent upwards when heated.

Figure 45 shows a composite of images depicting the membrane of device 4D14 as it is heated. With no bias through the heater the membrane shows a center deflection of -12.9 µm. As the membrane is heated it starts to bend downwards even further. For a bias of 50 mA on the 200 ohm (0.5 W) resistor the membrane's total deflection is 19 µm. As the bias is increased to 60 mA (0.72 W), the maximum deflection of the center of the membrane is of 23 µm.

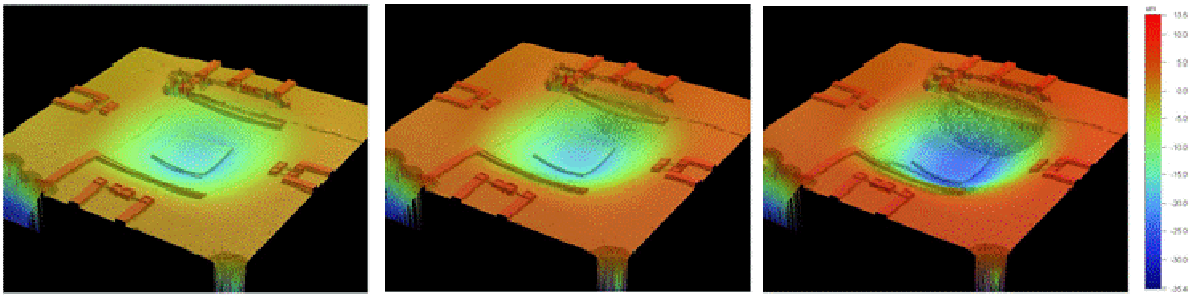

Figure 45. Device 4D14 heated with the in-situ p+-diffused resistor. The 3D surface profiles are for biases of the 200 ohm resistor with current of 0 mA, 50 mA and 60 mA from left to right.

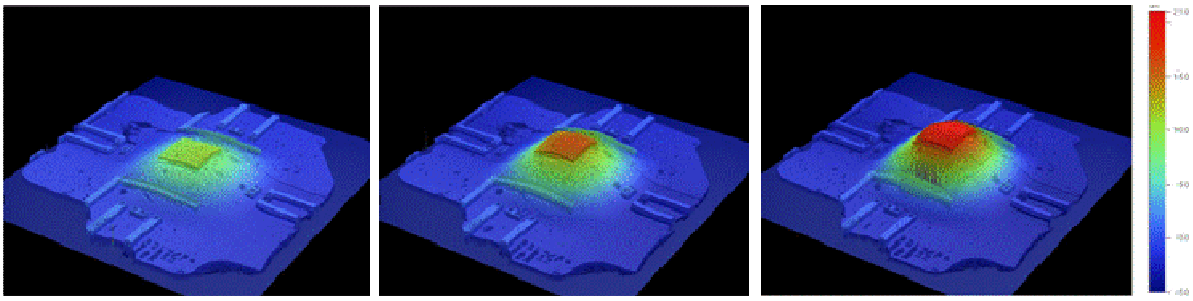

Figure 46. Device 4D6 heated with the in-situ polysilicon resistor. The 3D surface profiles are for biases of the 40 ohm resistor with current of 0 mA, 100 mA and 130 mA from left to right.

Figure 46 shows the results of heating the membrane with the polysilicon in-situ heater with a bias of 0.4 Watt and 0.676 Watts. The membrane continues to deflect upwards from the original 10.7 µm to a maximum of 25 µm.

It is important to understand that during dynamic oscillations the membrane will be set in motion by the burst of heat. The initial displacement set by this burst of heat will

determine whether the membrane displaces up or down. Based on the measurements presented here it will move further down when the membrane is originally down and farther up when it is originally up. After this original displacement, it will oscillate up and down around this new position but it will slowly return to its starting position. As such, the oscillations will be very similar in nature independently of the fabrication stress of the structures. We are interested in the behavior of these oscillations as they interact with fluid

7.4 Membrane modes of vibration

In order to observe the mode of vibration of the membranes we analyzed the shape of the membrane using two different excitation schemes. First we used a piezoelectric actuator to find the resonant frequency of the membranes and observed the vibration mode shape. This allowed us to verify the frequency and mode of vibration. Secondly, we used a burst heat excitation through the in-situ membrane heaters to set the membrane to free vibrate and then we tried to capture one full cycle of the vibration. Both this measurements were performed using the Dynamic MEMS (DMEMS) option of Veeco's Wyko NT-1100 real-time dynamic optical surface profiler. The DMEMS option allows the user to synchronize the actuator signal with profilometer measurements to obtain very accurate measurements of the surface of the sample.

7.4.1 Membrane resonance

Two devices were epoxied to a piezoelectric actuator as shown in Figure 47. This piezoelectric actuator was biased with a high voltage by the DMEMS system and moved

up and down. This movement also affected the devices glued to its surface. The membrane of the devices being tested was monitored by performing a surface profile measurement at a synchronized time interval. The frequency of the signal was increased until the surface profile indicated a resonant condition of the membrane. This happens when the deflection of the membrane dramatically increases. Once the frequency of resonance was determined, additional surface profiles were taken during one full cycle of resonance.

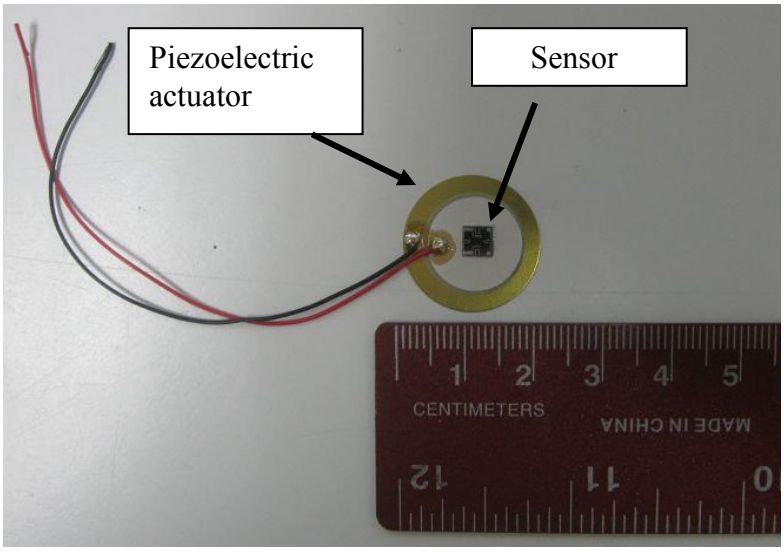

Figure 47. Sensor glued to piezoelectric actuator to explore resonant frequency and mode of vibration of the membranes.

Figure 48 shows a composite of pictures illustrating a full cycle of a device with a p+-diffused heater in 40 degree increments. It can be observed that the membrane is originally down and it will oscillate up and down by a few microns. The data presented here shows that this displacement is not enough to break the vertical plane of the device. The measured resonant frequency of 14,500 Hz falls within the expected values for such a device. The mode of resonance is the fundamental mode, up and down in the center of

the membrane, which is what is wanted for the fluid measurements to be undertaken. The amplitude of the oscillation is relative to the amplitude of the actuator and is not relevant as it will be different, and much lower, when heat excitation is utilized.

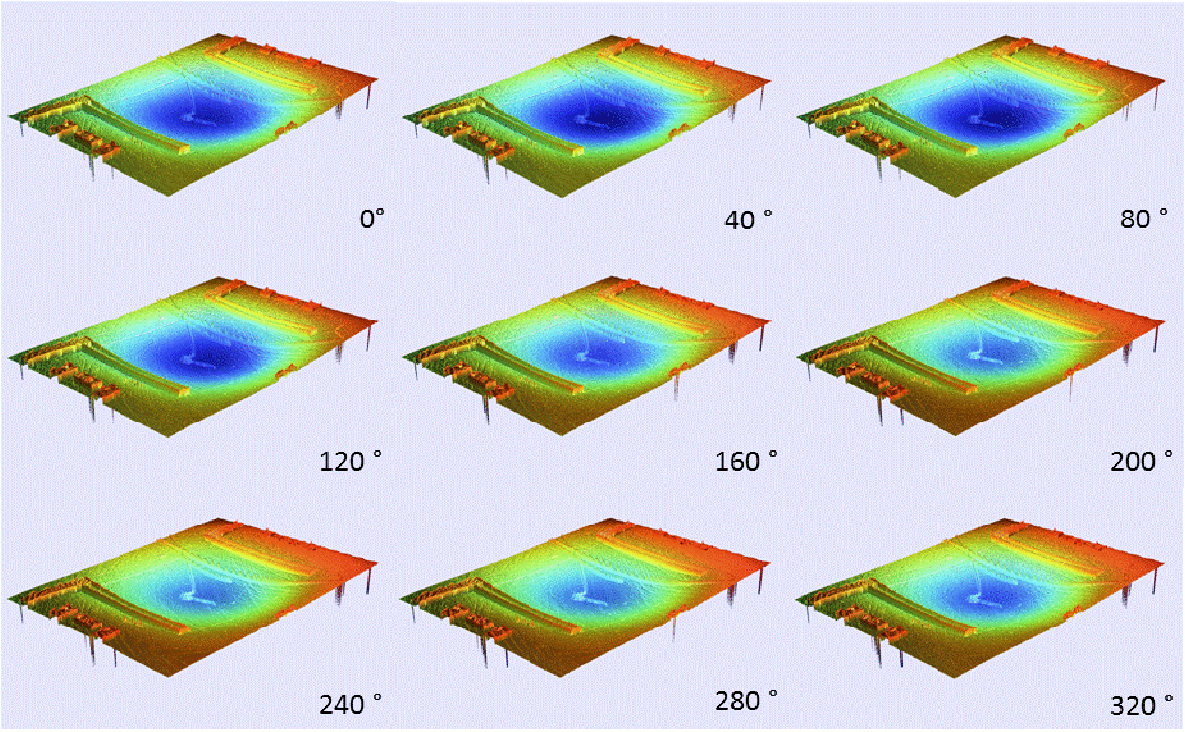

Figure 48. Full cycle of resonance of device with a p+-diffused heater.

Similarly, a device with a polysilicon resistor was also made to resonate at its natural frequency. The results for this device are presented in Figure 49. The fundamental mode of resonance can be seen from this sequence of surface profiles. The membrane starts deflected up and its center vibrates up and down around that starting position. The resonant frequency of this device was of 29,000 Hz which has also been observed on devices of this type electrically.

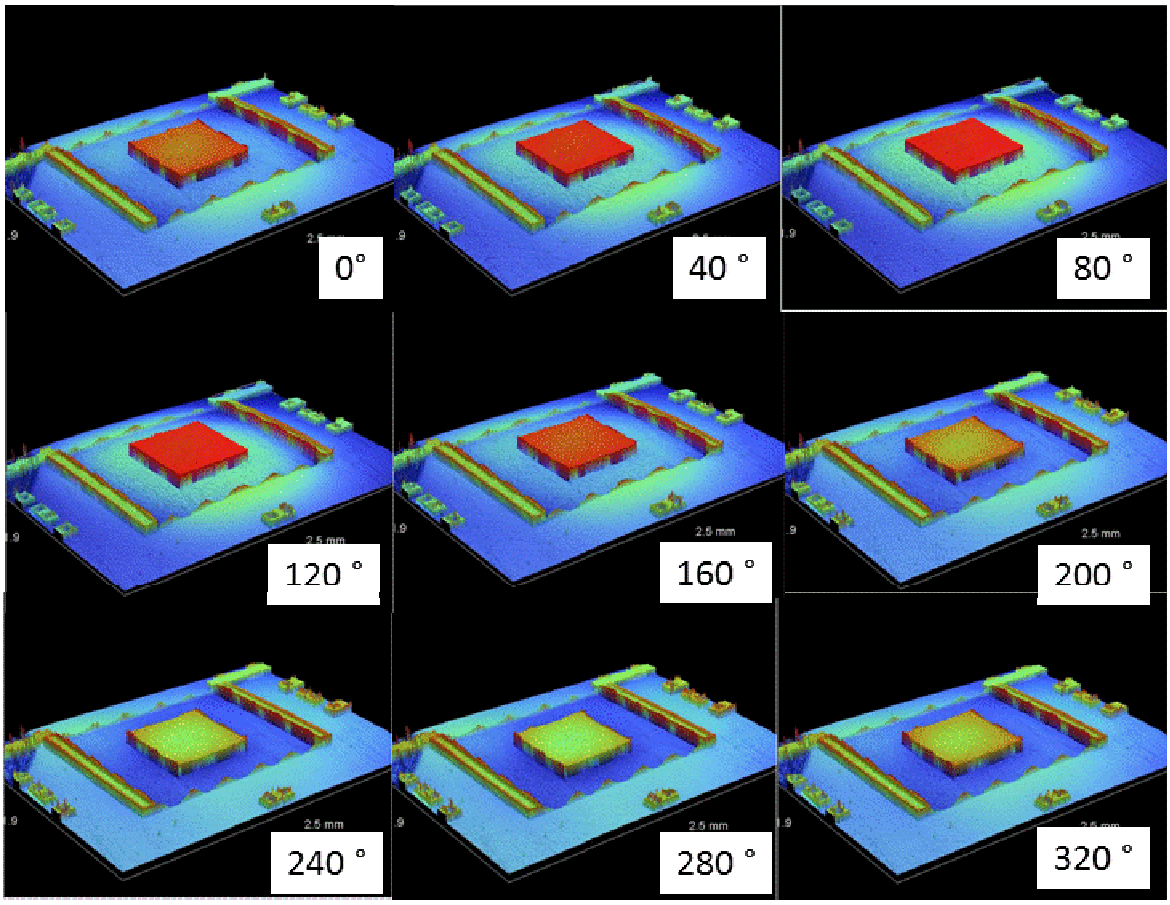

Figure 49. Full cycle of resonance of device with a polysilicon heater at 29,000 Hz.

7.4.2 Free vibration with heat-burst excitation

The DMEMS measurement tool in the Wyko profilometer requires that the movement of the structure to be measured is cyclical. The surface measurements are taken over several cycles at a determined time interval which is synchronized with the actuation signal. As seen in the previous section this is straight forward when the structure moves at the same frequency as the actuation signal. On the other hand, to measure the free vibration of a structure as a response to an impact load, as is the case in our devices, the measuring technique needs to be modified.

It is important to understand the nature of the excitation and the expected response of the structure in order to obtain accurate measurements. As such, an oscilloscope is used to electrically monitor the membrane movement. As can be seen in Figure 50, the membrane will start to oscillate as soon as the excitation signal is removed. The heater is rapidly increased to -15V for 20 microseconds at the end of the cycle so as to line up the sensor response at t=0 of the consequent cycle.. The frequency of oscillation of this particular device D11 is 17,224 Hz and the oscillation decays to noise level after 20 cycles or 1 millisecond.

The actuation signal was set to a frequency of 500 Hz which corresponds to a period of 2 milliseconds. The Wyko tool will perform measurements at a given time interval according to this actuation signal frequency. As such, dividing this time period by the 360 degrees, which the tool assumes as the full cycle of the oscillations, results in 5.556 microseconds / degree.

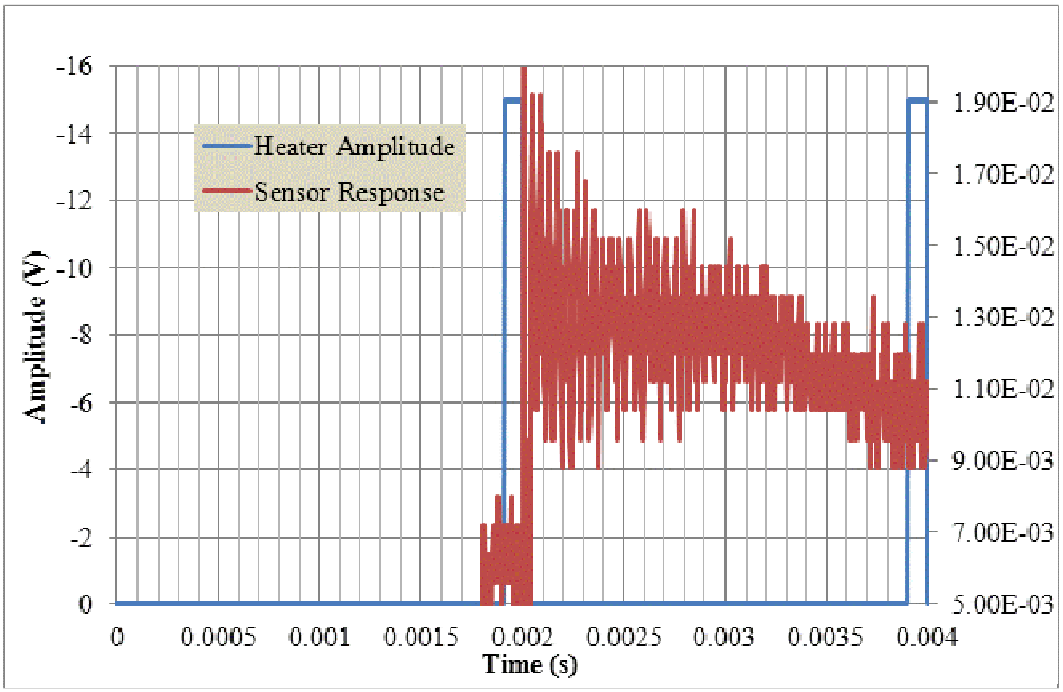

Figure 50. Excitation and membrane sensor signal during profilometer measurements.

Figure 51 shows a close up view of the sensor signal. During the first few microseconds the signal is noisy. As such, the measurements are taken during the second oscillation at t = 84 µs, 98 µs and 112 µs to obtain the maximum, middle and minimum position of the oscillation. These correspond to 15°, 17.5° and 20° of the actuator cycle respectively. The maximum value of this oscillation should be observed at 84 µs and the minimum at 112 µs. Knowing that the expected sensitivity is of 1.341 mV/µm, according to the calibration values obtained in Chapter 6, and keeping in mind that the output voltage has been amplified by a factor of 45 as described in Figure 12, the oscillation level that we are trying to measure is of 290 nm.

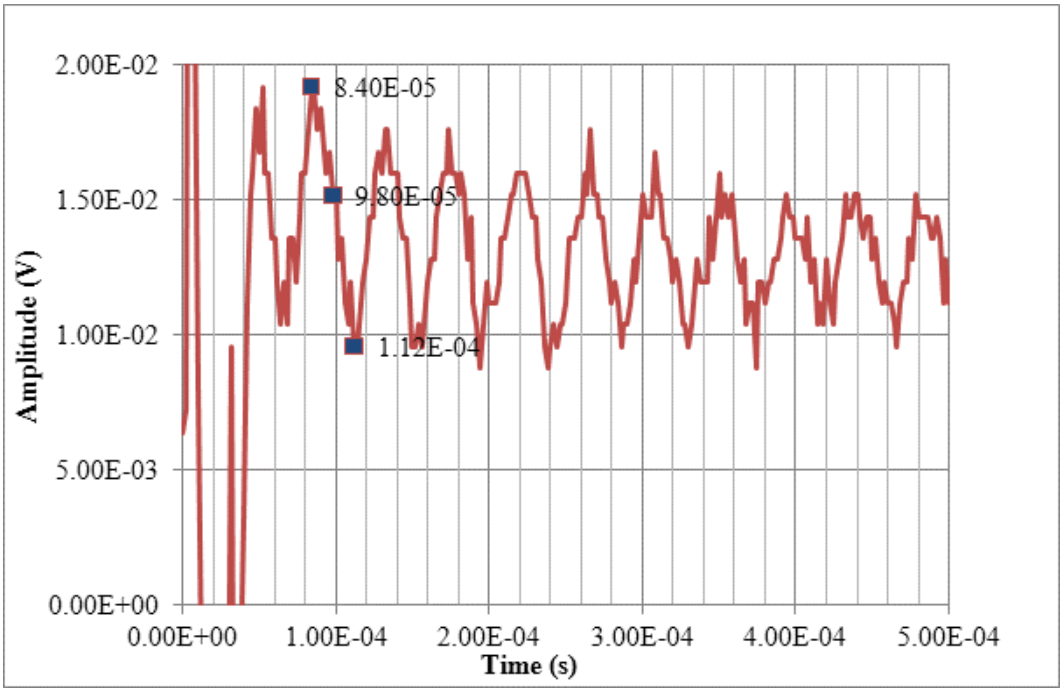

Figure 51. Detail of membrane sensor signal during profilometer measurements.

The resulting data is presented in Figure 52 for the maximum, center and minimum displacement points. Figure 53 shows the data extracted from the Wyko measurements overlaid with the data obtained from the electrical measurements after the calibration factor has been applied.

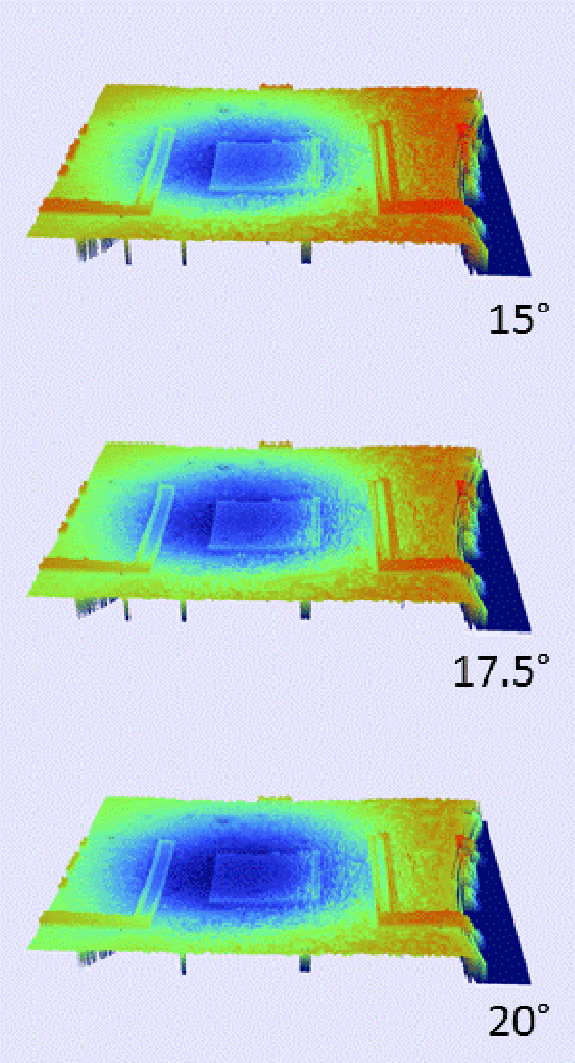

Figure 52. Wyko results of thermally actuated membrane vibrating at 17K Hz. The cycle amplitude is measured to be about 190 nm.

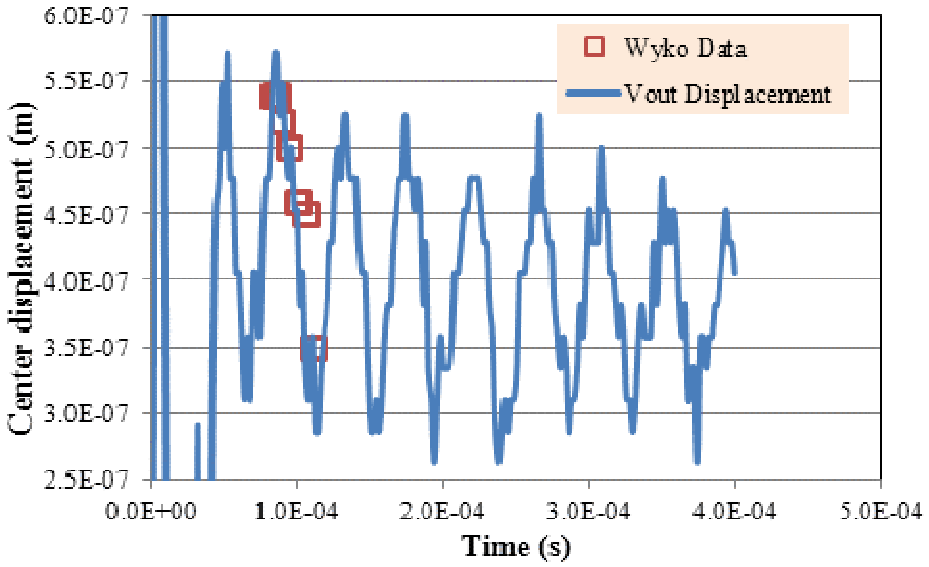

Figure 53. Overlay of the elecrical ouput and the DMEMS measurements obtained in the Wyko profilometer for sensor D11 vibrating in air.

These results confirm that the membrane is vibrating when excited with a burst of heat as predicted by the theory and the simulation. It also confirms that this vibration is at its fundamental natural frequency. More importantly, the vibration amplitude matches both the electrical measurements and the simulations values. This confirms that the static calibration that was performed originally is valid for dynamic measurements.

7.5 LabView integration

The test setup was improved from the previous chapters by integrating LabView to the data collection scheme. Figure 54 shows the schematic representation of this set up. The oscilloscope is connected to a PC trough a GPIB connection and that data is analyzed by a LabView script to perform a Fast Fourier Transform at an interval of 5 seconds. The FFT result is further analyzed to extract the frequency of oscillation, its quality factor and the amplitude of the oscillation.

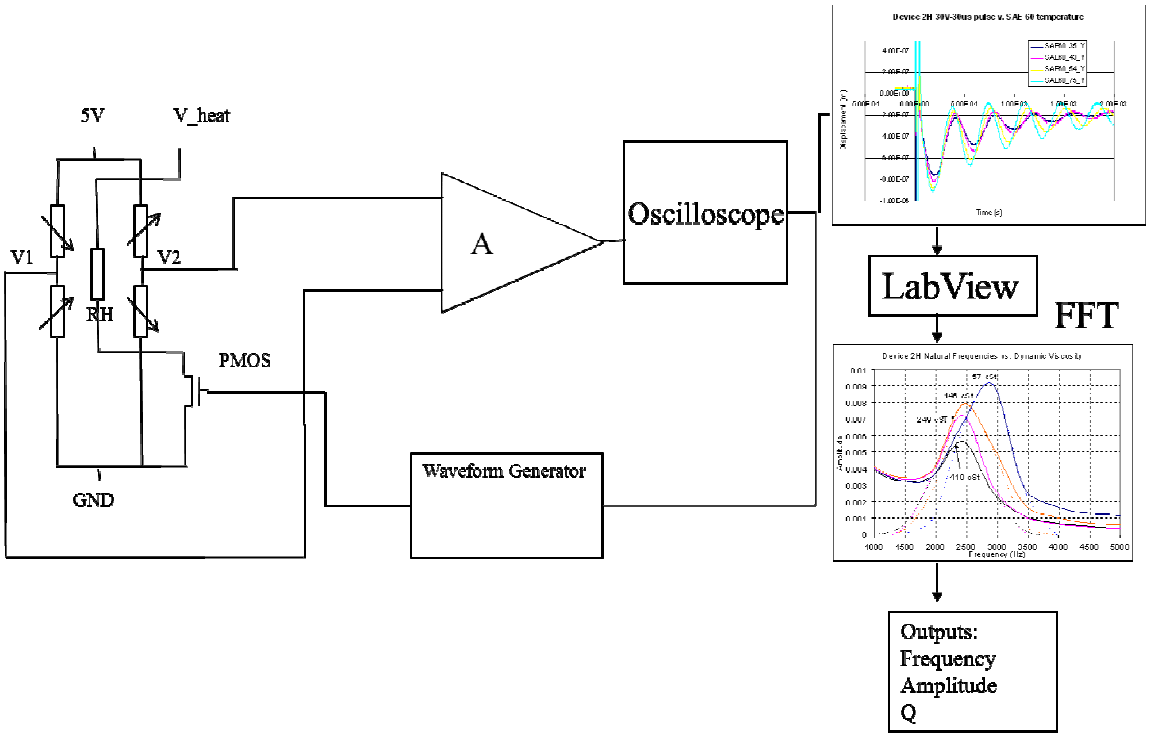

Figure 54. Schematic of Test setup with LabView Integration.

LabView was programmed to perform an FFT analysis of the 1000 data points that are imported from the Tektronic TDS3400 oscilloscope every 5 seconds. Using a peak detector routine LabView identifies the vibration frequency by fitting a quadratic peak to the FFT signal within a determined number of points. The frequency value of this peak can be calculated by knowing the delta Frequency (*dF*) utilized by the FFT routine as such:

$$f_{\max} = x_{\max} \cdot dF \qquad (50)$$

The quadratic fit routine outputs the second derivative ***y''*** and y_{max} of that function. By assuming a quadratic equation of the form:

$$y = ax^2 + b\,. \qquad (51)$$

Since we know ***y''*** and ***ymax,*** we can re-write this equation as:

$$y = \frac{y''}{2}x^2 + y_{\max} \tag{52}$$

The Q value was calculated by using the parameters of this quadratic equation to find the 1/2 max of the peak frequency as follows:

$$\frac{y_{\max}}{2} = \frac{y''}{2}x^2 + y_{\max} \tag{53}$$

$$x_{1,2} = \pm\sqrt{\frac{-y_{\max}}{y''}} \tag{54}$$

$$Q = \frac{f_{\max}}{(f_{\max} + x_1 \cdot dF) - (f_{\max} - x_2 \cdot dF)} \tag{55}$$

The amplitude of the oscillating frequency is calculated by the FFT routine as a Vrms.

A snap-shot of the LabView program is presented below in Figure 55. The code shows the programming done once the data has been collected from the oscilloscope. This code also includes a routine to obtain the vibration measurements directly from the raw oscilloscope data without performing an FFT. This data is not always reliable as it is very susceptible to the noise level of the vibration. As such, the FFT routine is the preferred one. The code to obtain the temperature value from a small-form discrete forward-biased diode is also shown with its calibration factor included.

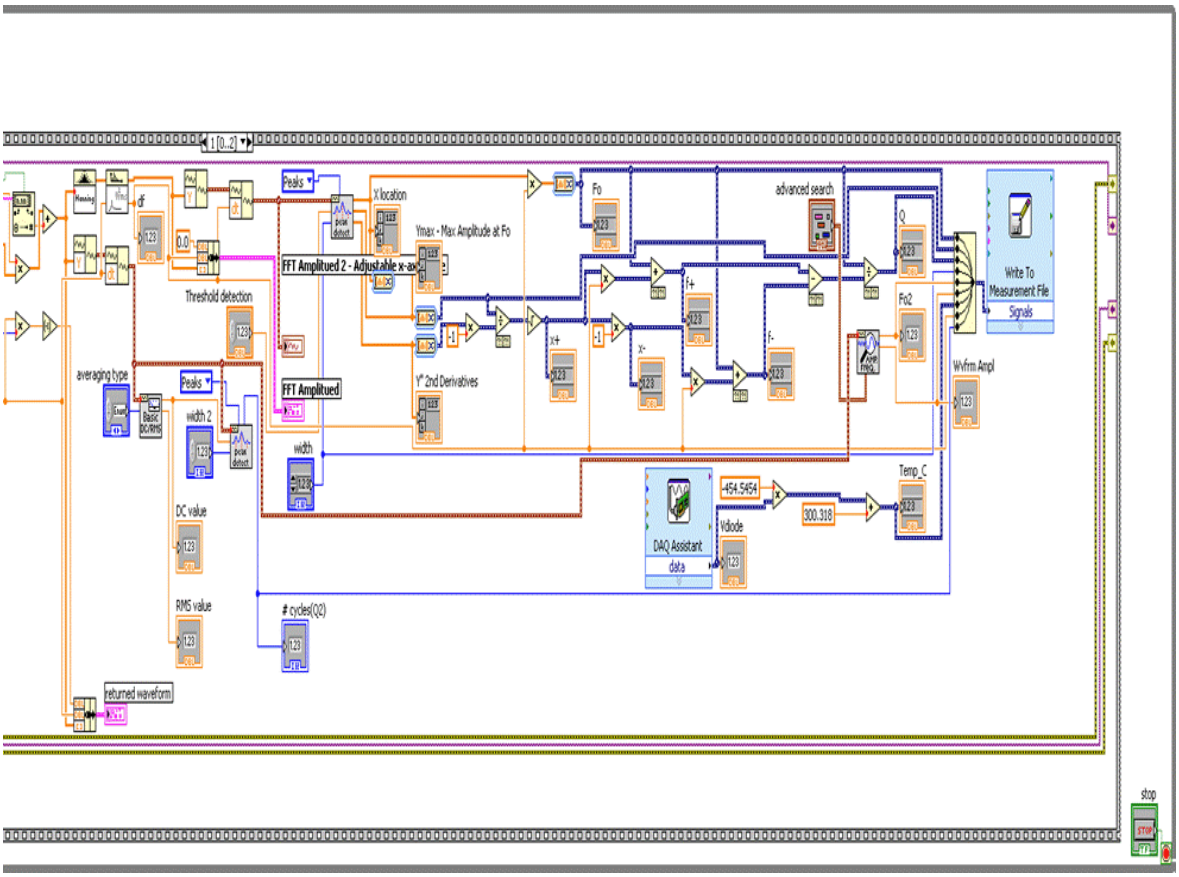

Figure 55. LabView code written to perform FFT mesurements on the data collected from the oscilloscope.

The front panel of the LabView interface is shown in Figure 56. The imported oscilloscope data is shown on the top part of the interface. Measurements are taken from this raw data using LabView's peak fit routine. This routine extracts the vibration frequency and the number of oscillations but it is very sensitivity to noise and it is not reliable. Two FFT plots are shown. The bottom one offers a general view of the spectrum. The one on top shows a close-up of the range of frequencies of interest. The peak fit routine is used in the FFT spectrum to detect the value of this peak. The quality factor is determined from this routine as described above. The interface also indicates the temperature measured with the discrete diode. There are also some simple instructions on how to set up some of the measurement parameters. Every 5 seconds, the routine will

save the peak frequency, the quality factor and the amplitude from the FFT data and the temperature.

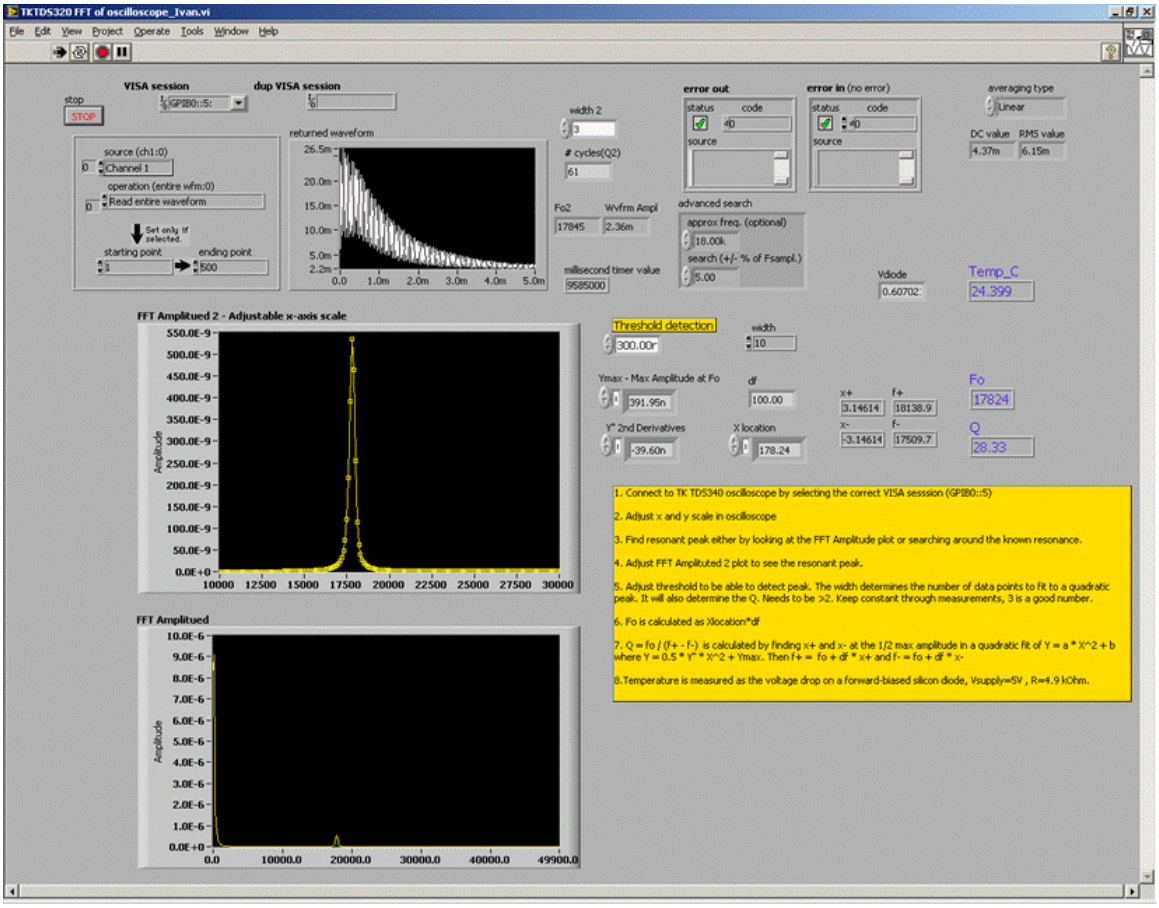

Figure 56. LabView front panel interface.

7.6 DOE Results

The designed experiment was analyzed using an ANOVA study of the main effects. Data was collect at room temperature for 23 different sensors. The devices were tested directly on a wafer chuck after they had been diced. This was done to prevent any variation that could be introduced during packaging. Some variation is expected as some of the devices showed fabrication defects which are likely to affect the natural vibration behavior.

Q and amplitude of vibration were normalized to the applied power to account for the resistance difference between the p+-diffused and the poly heaters. This is shown in Figure 57 where two devices with the same characteristics other than the material of the heating resistor were tested. The vibration characteristics of devices 4D34 and 4D28 are shown in this Figure. 4D34 has a 220-ohm p+-diffused heater and 4D28 a 40-ohm poly heater. Increasing the Voltage applied to the higher resistance heater form 14V to 30V results in similar Q and amplitude of vibration as that of the lower resistance heater without affecting the frequency of oscillation It is important that the power applied to all devices be the same so that a direct comparison of the Amplitude and the quality factor of the oscillation can be made.

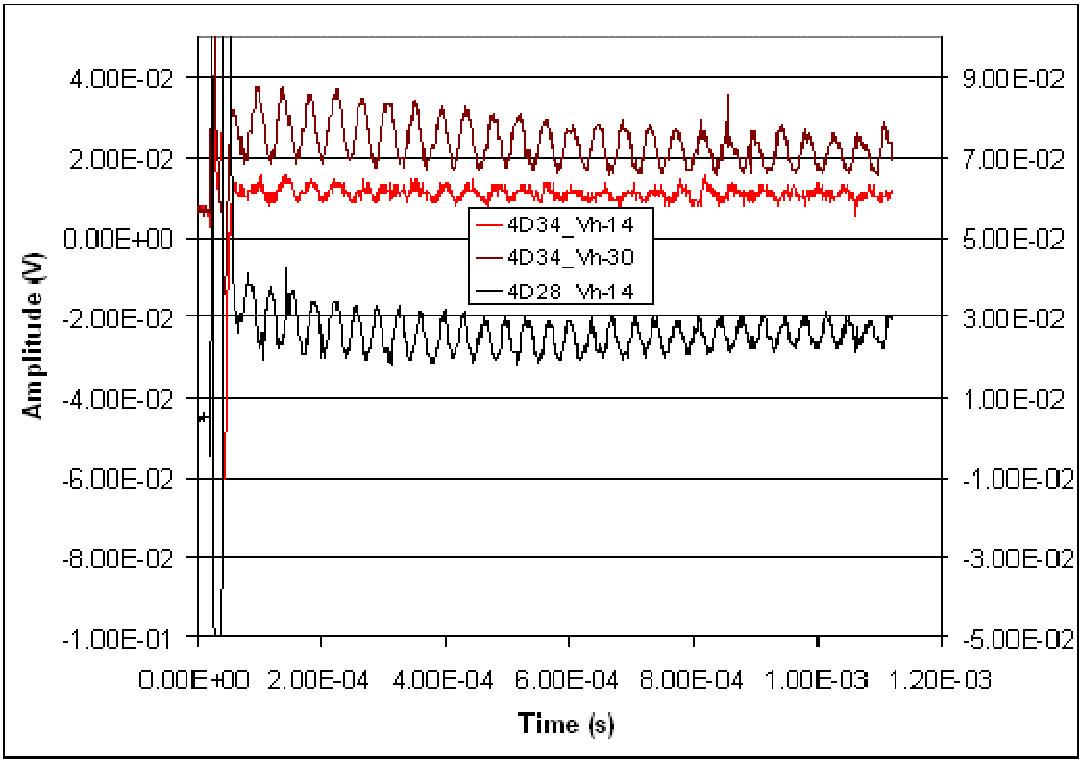

Figure 57. Vibration characteristics of devices 4D34 and 4D28.

The ANOVA results indicate a good model fit for Fo, Q and Amp with R^2 values of 0.96, 0.89 and 0.83 respectively. The summary of these model fits can be seen in Appendix B. The following Figures present a visualization of these results.

The x-axis indicates the characteristic of the device tested according to the DOE factors. The results for the p+-diffused heater devices are shown on the left of the Figure and the results for the devices with polysilicon heaters are shown the right. The devices have also been grouped by heater size. Finally they have been divided on whether passivation and/or metal are present. Lines, arrows and labels have been included to help follow the trends.

Figure 58 shows the results of the natural frequency of vibration to the variables studied. For the devices with a p+-diffused heater the addition of passivation and metal increase the frequency of vibration as thickness and stiffness of the membrane increases. This is not so for the devices with a poly heater with the exception of the devices with the smallest polysilicon heaters.

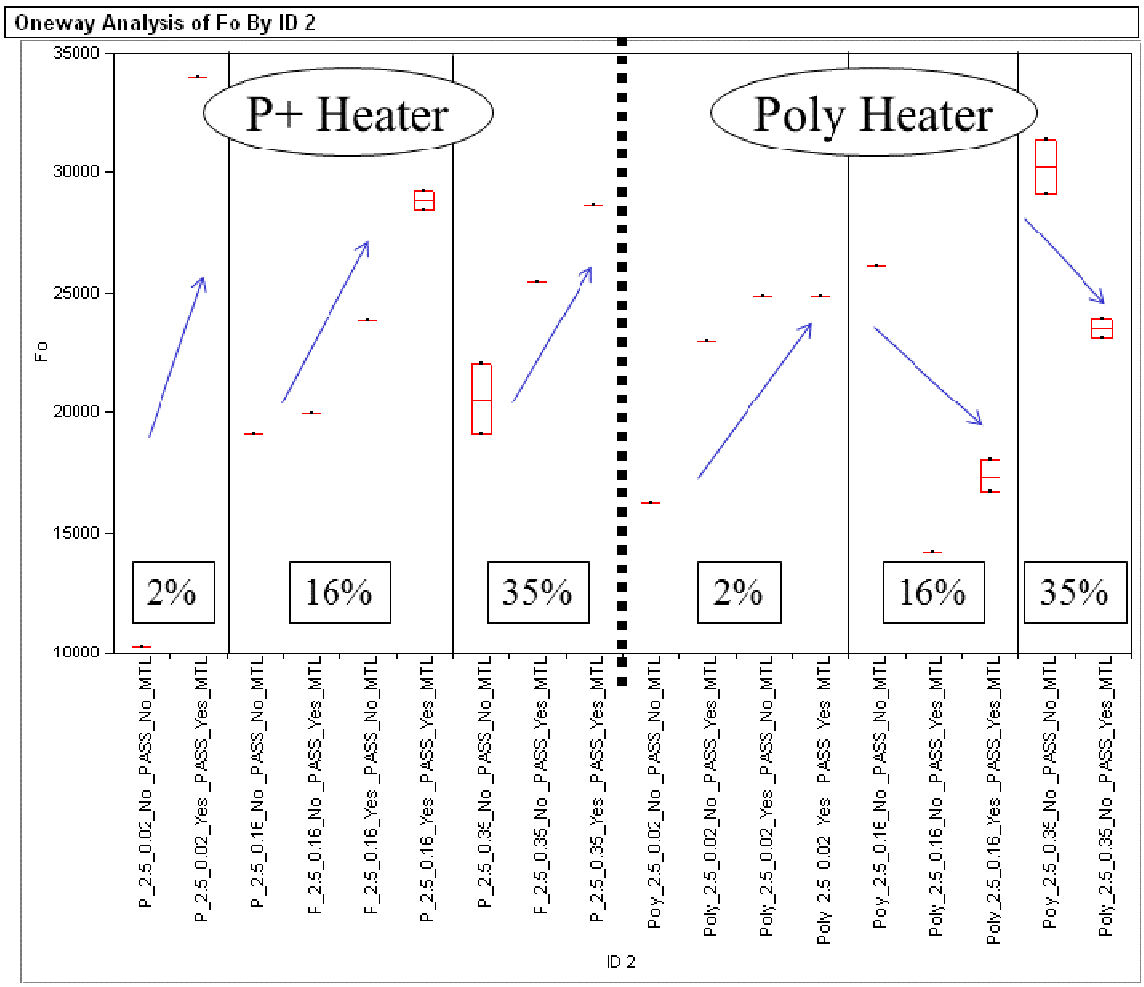

Figure 58. Frequency variation due to varations in heater material, size, passivaiton and metal.

Figure 59 shows the results of the quality factor Q of the vibration to the variables studied. The results indicate that the devices with heaters of 2% and 16% of the total membrane area result in higher Q values. The p+-diffused heater, with metal and passivation, independently of its size, results in an increased Q. On the other hand, devices with poly heaters see a decrease in Q when metal and passivation are present.

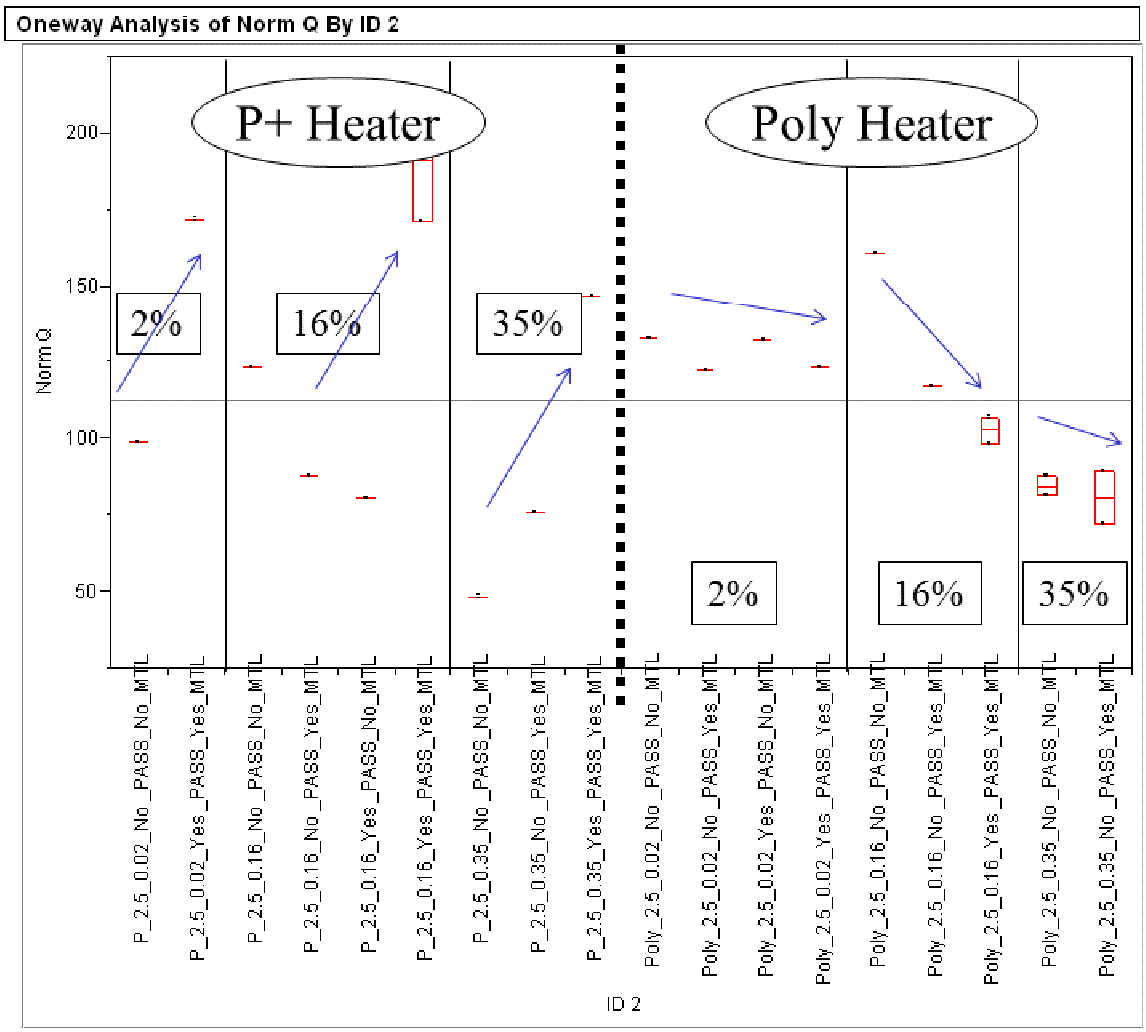

Figure 59. Q variation due to varations in heater material, size, passivaiton and metal.

Chapter 9.

VISCOSITY MEASUREMENTS

The standard mineral oils and commercial motor oils shown in Table 14 were used to perform viscosity measurements at room temperature. The viscosity and density reference standard oils were obtained from Koehler Instrument Company, Inc. An uncertainty between 0.07% and 0.17% is expected. The commercial motor oils were test at Impact Technologies LLC using a Brookfield DV-II+Pro cone-and-plate viscometer.

The devices shown in Table 15 were packaged on a PCB and fully submerged in the oil to be tested. A significant representation of the devices with best expected performance based on the DOE results was chosen. The sensors were glued and wire bonded to a PCB board with an access hole drilled on its back. Thus, both surfaces of the diaphragm are in direct contact with the fluid to be tested. The PCB was suspended over the oil and held at only one point as shown in Figure 60. The intent is to allow the sensor to vibrate freely without adding any external stress. External stress could be added if the PCB rested on the bottom or against the sides of the container. It is important that the devices always be position the same way so as to not affect the natural vibration behavior.

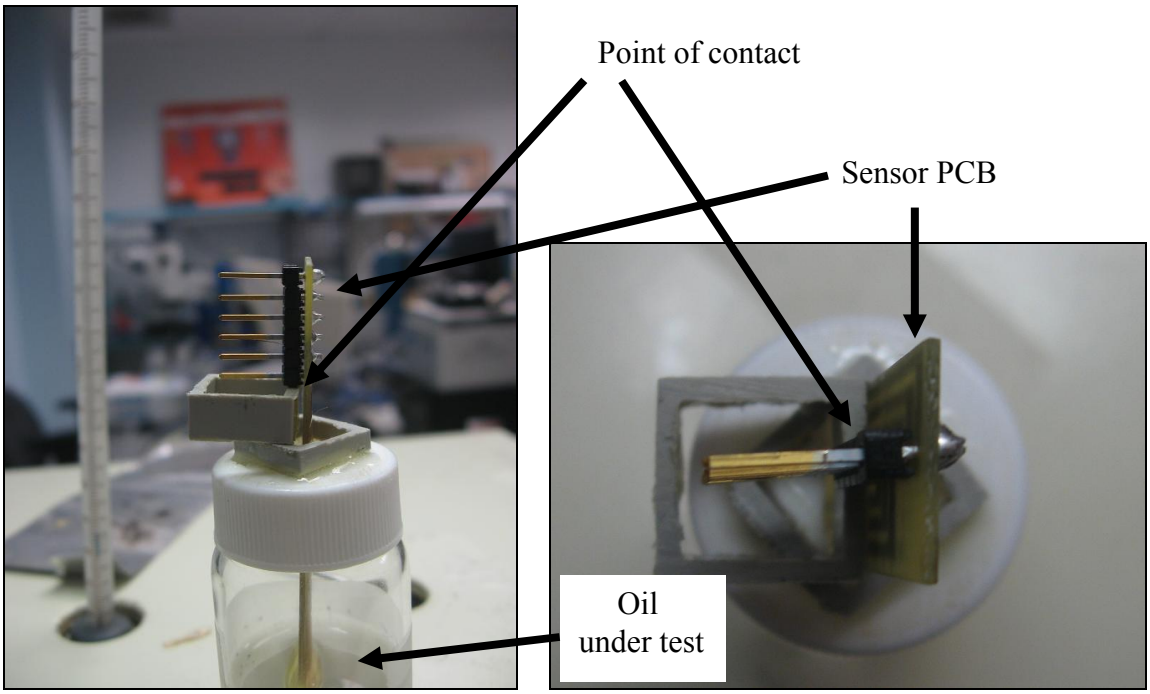

Figure 60. Side-view (left) and top-view (rigth) showing how the sensor is positioned over the test fluid.

The devices were first tested in the standard oils with increasing viscosity. Then, they were tested in the commercial motor oils, with viscosities falling within the range of the standard oils. The devices were carefully cleaned with a lint-free cloth wipe between tests in order to prevent damaging or softening the epoxy which would result with the use of degreasers, solvents or water. Some cross-contamination is possible but this would always happen to the higher viscosity oil and the effect should be small.

The same test conditions were used through the testing of each device. The typical settings were a Wheatsone Bridge bias of 5 V, a heating resistor bias at a frequency of 20 Hz with a voltage of -15 V for 30 microseconds and an amplifier gain of 50. These conditions were slightly adjusted for each sensor in order to obtain the best signal possible.

Table 14 STANDARD AND COMMERCIAL MOTOR OILS USED FOR ROOM TEMPETATURE (25 °C) MEASUREMENTS

Oil	Kinematic Viscosity (25 °C) mm^2/s or cSt	Density (25 °C) g/mL
S3	4.035	0.8085
S6	8.792	0.8231
N10	17.01	0.8484
N35	65.07	0.8519
N100	238.7	0.8638
N350	824.2	0.8708
5W30	132.91	0.8860
10W40	211.49	0.8650
SAE60	644.20	0.8690

Table 15 DEVICES TESTED WITH STANDARD AND MOTOR OILS AT ROOM TEMPERATURE

ID	Size	Heater	Heater Size	Passivation	Metal
D12	2.5	P	2%	Yes_P	Yes_M
D11	2.5	P	16%	Yes_P	Yes_M
4D27	2.5	Poly	2%	Yes_P	Yes_M
4D22	2.5	Poly	16%	Yes_P	Yes_M
D62	2.5	Poly	16%	No_P	No_M
4D10	2.5	Poly	35%	No_P	No_M

The typical vibration behavior of one of these devices in the different oils is shown in the composite of Figure 61. As seen in this sequence the number of vibrations decays as the viscosity increases. This can be measured by monitoring the Q value of the FFT output. The Vrms amplitude of the vibration is also an indication of this behavior as its amplitude over a fix period of time, decays with increasing viscosity. It's more difficult to observe the frequency variation in these plots. The frequency, according to the theory presented in Chapter 4, is expected to decrease with the increase in both density and viscosity. This response is more easily studied with the automated data collection integrated with LabView.

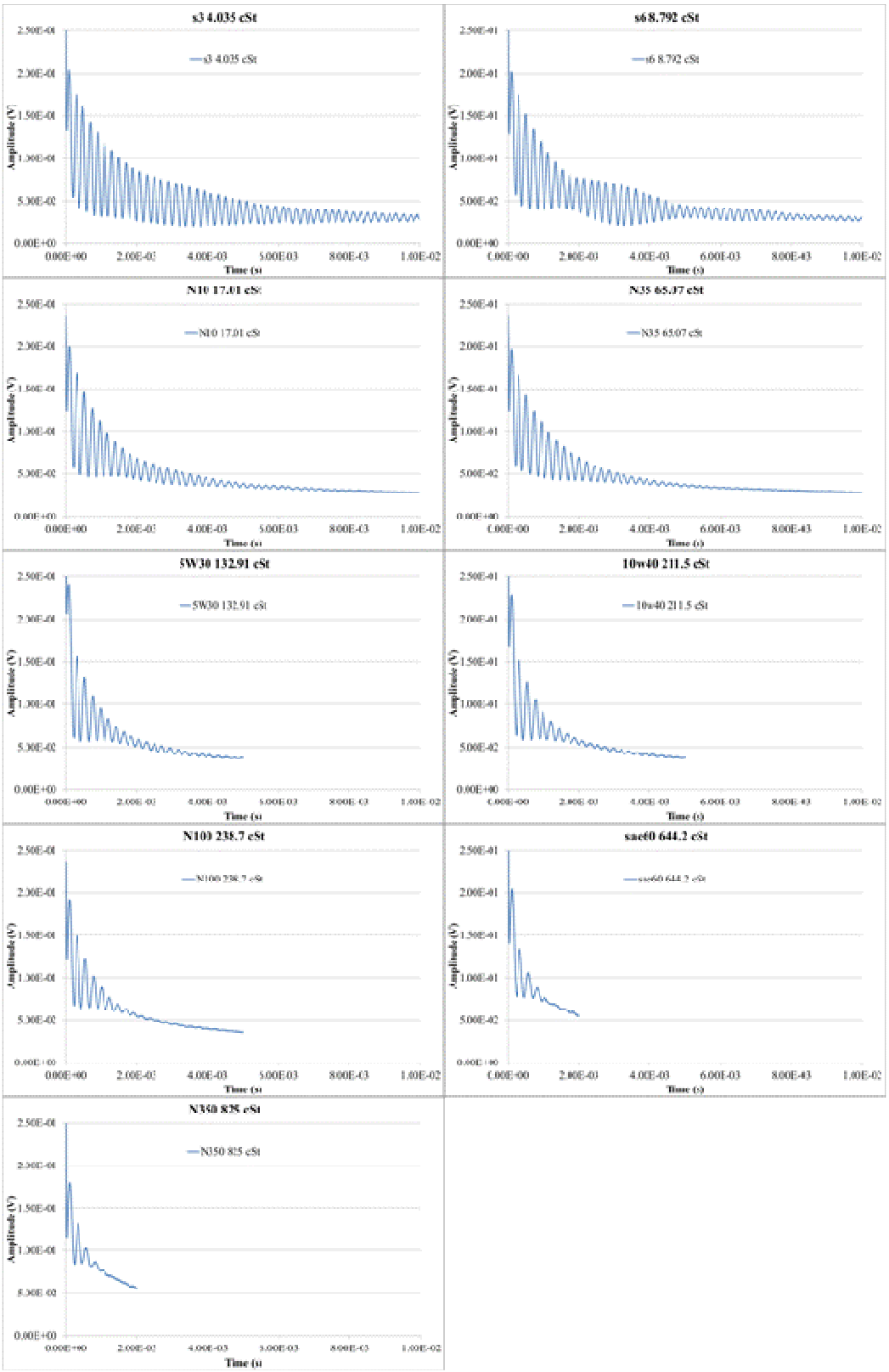

Figure 61. Vibration sequence of device 4D10 in oils of increasing viscosities.

As described in the earlier sections of this Chapter, the data collection was automated through LabView to extract the frequency of vibration, quality factor and the amplitude of the oscillation. Figure 62 shows the results obtained with D62, which is a typical representation. The sensor was placed in each of the oils for different lengths of time as can be seen by the different number of data points at each viscosity condition. The trend shows the expected decrease in vibration amplitude Vrms as the viscosity increases. The last three viscosity groups correspond to the motor oil samples and where purposely chosen to fall within the range of standard oils.

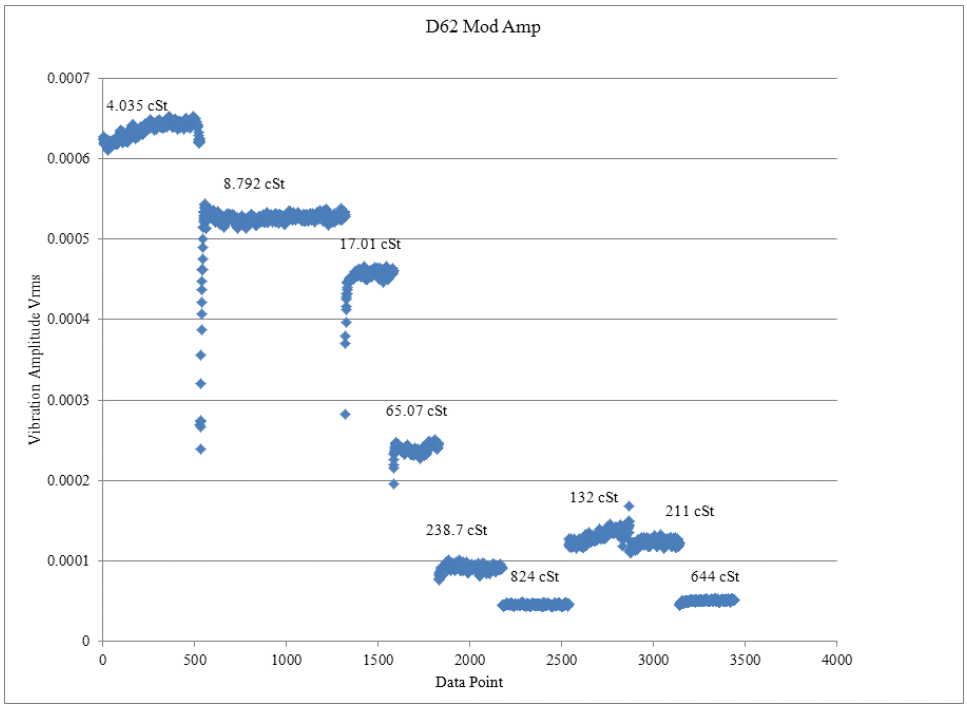

Figure 62. Vibration amplitude Vrms change with increasing viscosity for device D62.

Figure 63 shows how the change in viscosity affects the frequency of vibration of device D12. Although device D12 shows a clean signal this result was more difficult to obtain for other devices. The frequency of vibration of the membrane seems to be affected by the placement of the sensor during test. Depending on the way the PCB was

placed in the text fixture the vibration frequency will change by a factor larger than that of the induced by the change in viscosity or density. The same is to be said for Q as it depends on the frequency of vibration. A typical result obtain for Q is presented in Figure 64. The variation of this measurement within each group is significant. Other devices showed even more variation. The more reliable and consistent test was the vibration amplitude Vrms which does not depend on extracting the frequency of vibration from the FFT but rather on integrating the amplitude of the vibration through the time interval and performing a root mean square measurement.

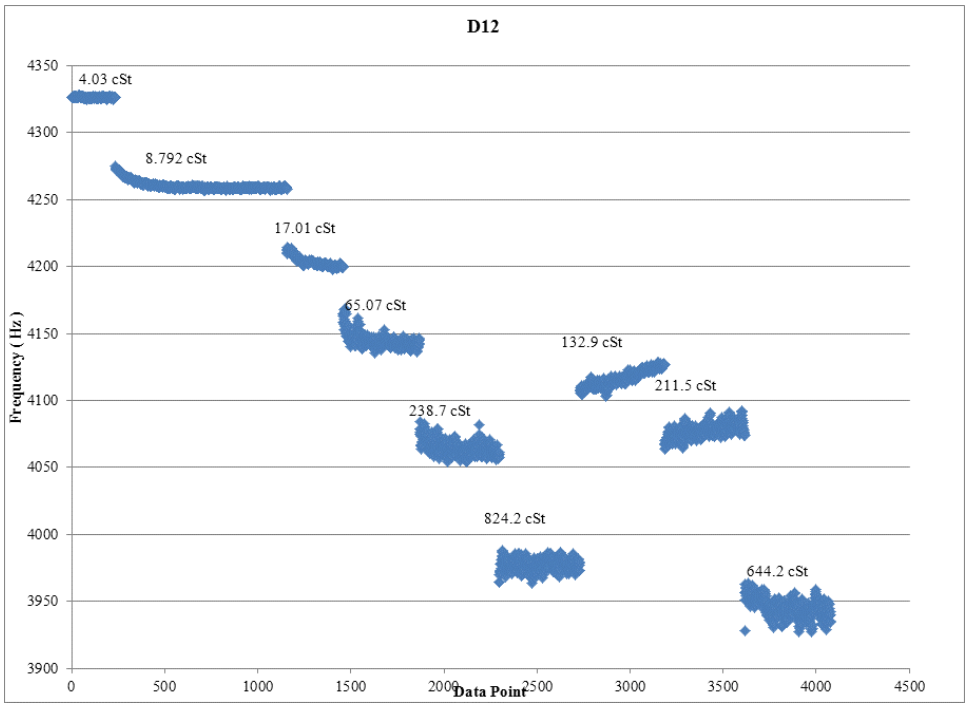

Figure 63. Vibration frequency change with increasing viscosity for device D12.

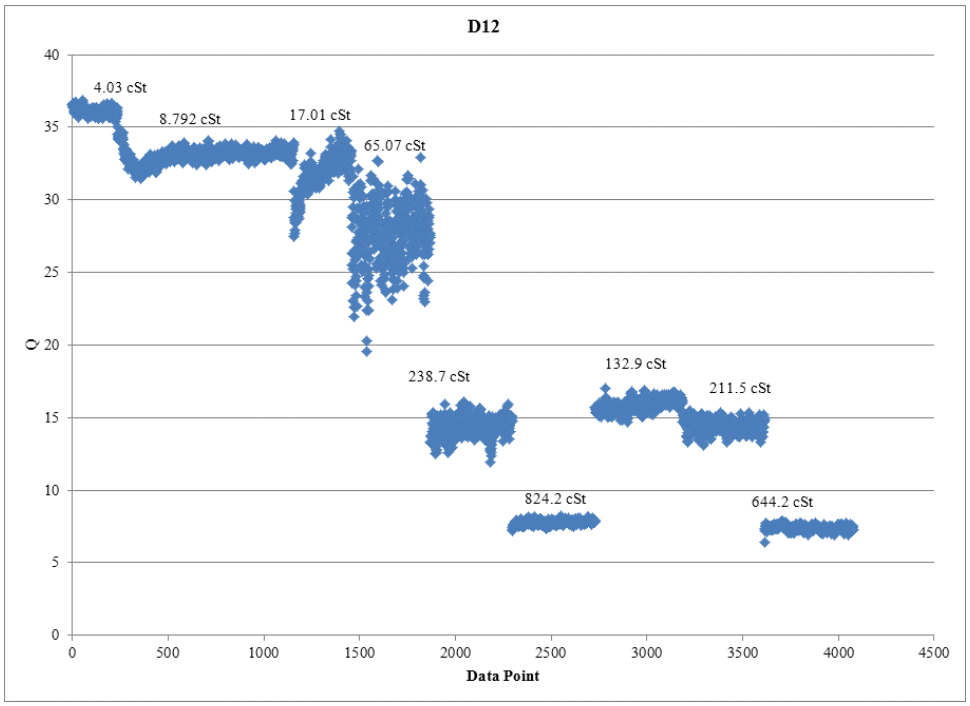

Figure 64. Q change with increasing viscosity for device D12.

In order to determine whether the sensor is reacting to either changes on viscosity of changes in density, the two variables are plotted along with the predicted theoretical behavior described in Chapter 4. The natural frequency of vibration was expected to shift according to Lamb's prediction when the sensor was placed in the oil as predicted by the equations below:

$$\omega_{fluid} = \frac{\omega_{vacuum}}{\sqrt{1+\beta}} \tag{56}$$

where β

$$\beta = 0.669 \frac{\rho_{fluid} a}{\rho_{plate} h} \tag{57}$$

This shift in frequency would not only be due to the density of the oil but also due to its viscosity according to Kozlovsky's model. The Q value of these structures would also decrease as the viscosity increased due to the dampening of the vibrations. Kozlovsky's observations also predicted that the frequency shift due to viscosity would not be as

significant when the viscosity fell below the threshold value of <10 cP. Below 10 cP, viscosity does not seem to affect the natural frequency of vibrating diaphragms [5].

Kozlovsky's model modifies Lamb's virtual mass $\boldsymbol{\beta}$, as shown below, to predict the decrease in frequency due to both the density and viscosity increasing.

$$\beta = 0.6538 \frac{\rho_{fluid} a}{\rho_{plate} h}(1 + 1.082\xi) \tag{58}$$

$$\text{where, } \xi = \sqrt{\frac{\upsilon}{\omega a^2}} \tag{59}$$

Kozlovsky's model also predicts the effect of viscosity to the Q factor as follows:

$$Q = 2\pi \frac{energy\_stored}{energy\_dissipated\_per\_cycle} \approx \frac{0.95}{\xi} \tag{60}$$

Figure 65 shows the change in normalized frequency due to the change in viscosity for the sensors studied. The theoretical prediction using Lamb's and Kozlovsky's model is also shown for comparison. Trend lines have been added to observe the general sensitivity. The actual power law fits are shown in Table 16 . Error bars have also been added as one standard deviation. The results match Kozlovsky's prediction for devices D11 and D12 which have p+-diffused heaters as actuators. Devices 4D27 and 4D10 have poly heaters and seem to have a slightly higher sensitivity than the predicted by the theory. The shape of the response matches the theoretical prediction and a power law fit can be applied. Table 16 shows the equation and R-squared value of these fits. When plotting the response of the frequency to the changes in density the general response is to decrease with an increase in temperature. A linear fit can be applied to the sensor response but the goodness of fit is not as good as the fit to the change in viscosity as seen in Figure 66.

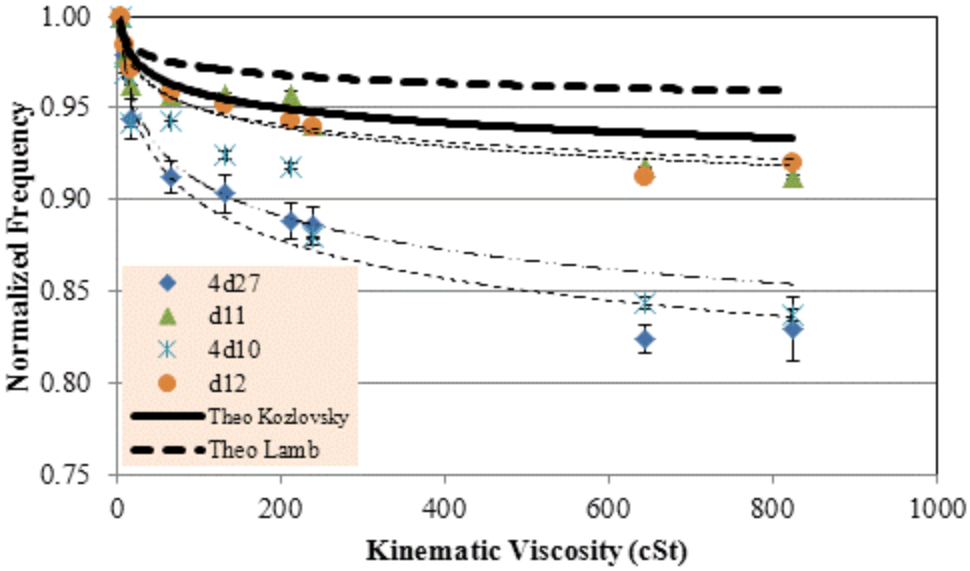

Figure 65. Normalized frequency as a function of changes in viscosity.

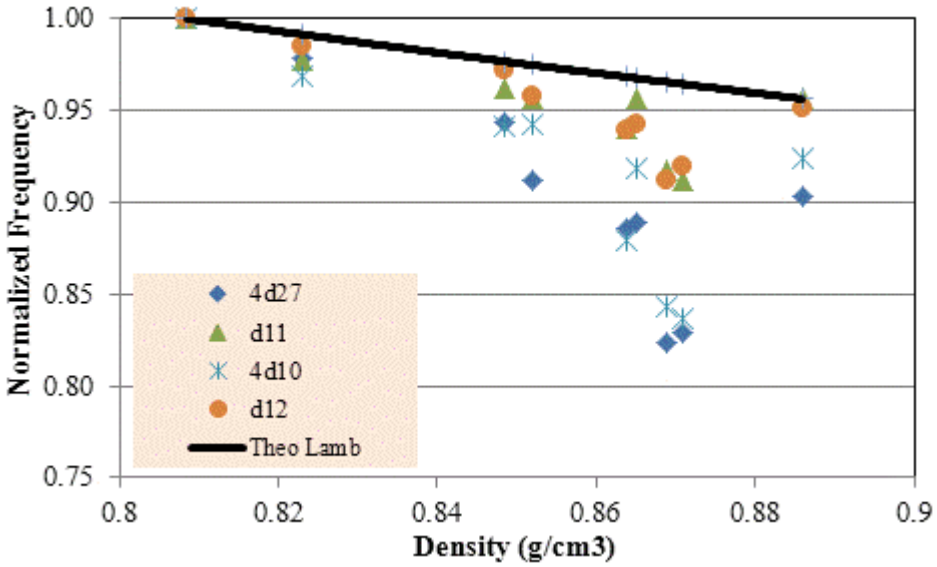

Figure 66. Normalized frequency as a function of changes in density.

Table 16 POWER LAW FIT TO FREQUENCY OF DEVICES TESTED IN CHANGING VISCOSITY

ID	Size	Heater	Heater Size	Pass	Metal	Fo	Fo-Rsq
D11	2.5	P	16%	Yes_P	Yes_M	$y=1.0148x^{-0.014}$	0.871
D12	2.5	P	2%	Yes_P	Yes_M	$y=1.0214x^{-0.016}$	0.969
4D10	2.5	Poly	35%	No_P	No_M	$y=1.0448x^{-0.03}$	0.882
4D27	2.5	Poly	2%	Yes_P	Yes_M	$y=1.0533x^{-0.034}$	0.959

A similar analysis was done for the energy dissipation factor Q. The Lamb model does not predict the behavior of this factor as it does not take into account the effect of viscosity. Kozlovsky's model predicts its behavior with Equation 59 and 60. Figure 67 shows the predicted values compared to the measured values for six different sensors. Error bars have been added to the data points to indicate one standard deviation. Power fits have been added although not labeled to avoid crowding the plot. The trend lines help visualize the response and to confirm that the follow the same trend. The actual equation fit and the R-squared values are presented in Table 17. Figure 68 shows Q plotted against the density of the oils tested. Even though there is a general down trend, there is no clear relationship between the change in density and Q. The general down trend is due to the higher density values of the higher viscosity oils rather than the increase in density itself.

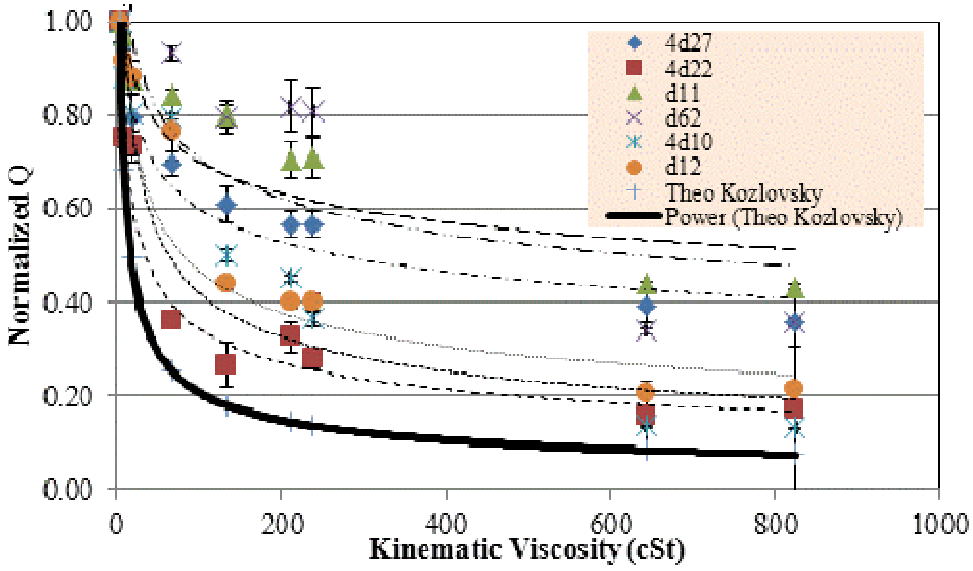

Figure 67. Normalized Q as a function of changes in viscosity.

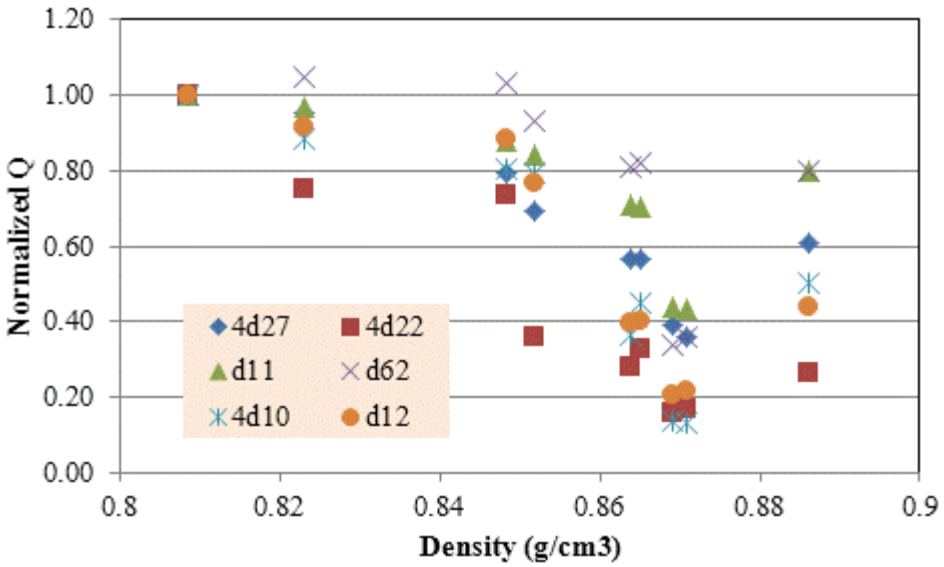

Figure 68. Normalized Q as a function of changes in density.

Table 17 POWER LAW FIT TO Q OF DEVICES TESTED IN CHANGING VISCOSITY

ID	Size	Heater	Heater Size	Pass	Metal	Q	Q-Rsq
D11	2.5	P	16%	Yes_P	Yes_M	$y=1.3783x^{-0.147}$	0.791
D12	2.5	P	2%	Yes_P	Yes_M	$y=1.9189x^{-0.307}$	0.901
4D10	2.5	Poly	35%	No_P	No_M	$y=2.2833x^{-0.368}$	0.803
4D27	2.5	Poly	2%	Yes_P	Yes_M	$y=1.3992x^{-0.184}$	0.943
4D22	2.5	Poly	16%	Yes_P	Yes_M	$y=1.6766x^{-0.345}$	0.962
D62	2.5	Poly	16%	No_P	No_M	$y=1.6785x^{-0.188}$	0.648

From Table 17 we can see that the devices 4D22 and D12 show the best fit, but there is no clear factor that determines the best fit. There is quite a big range of responses but a consistent trend. Devices D11 and D62 have the poorest fit. These two devices also had a poor fit with respect to the vibration frequency. As mentioned previously the vibration frequency sensitivity seems to be affected by factors difficult to repeatedly control in a lab environment such as sensor fabrication defects, PCB positioning and cleaning methods between tests. These issues could be solved in a production environment where quality control is much better.

As mentioned above a factor that is not dependent on the frequency of vibration but that it gives us an indication of the energy dissipated by viscosity is the vibration amplitude factor Vrms measured by the FFT routine. This factor needs to be normalized to a consistent time interval as the FFT Vrms amplitude routine will not account for the range change that is needed to obtain an accurate measurement at the higher viscosity settings.

The improvement is clearly visible in Figure 69. In this Figure Kozlovsky's theoretical prediction for Q has been plotted to use as a reference. The Vrms amplitude matches this trend better than the actual calculation for Q, this leads to the conclusion that this factor is indeed an indication of the energy dissipation factor Q. The only exception is device 4D27. This sensor showed very small Q values even when immersed in oils with low viscosities and does not seem to behave accordingly to the other devices. The power law fit of all the sensors is summarized in Table 18

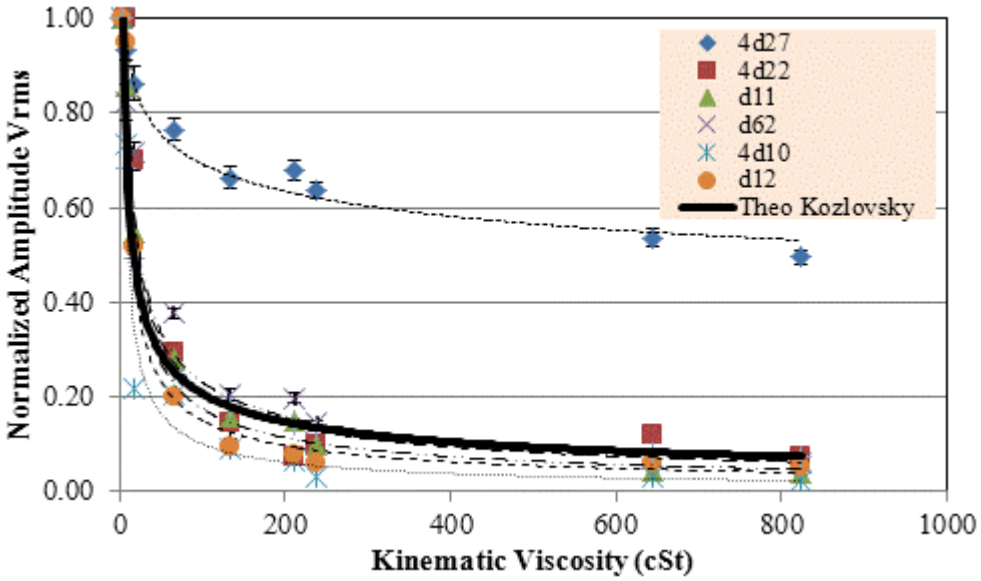

Figure 69. Normalized Vrms amplitude as a function of changes in viscosity.

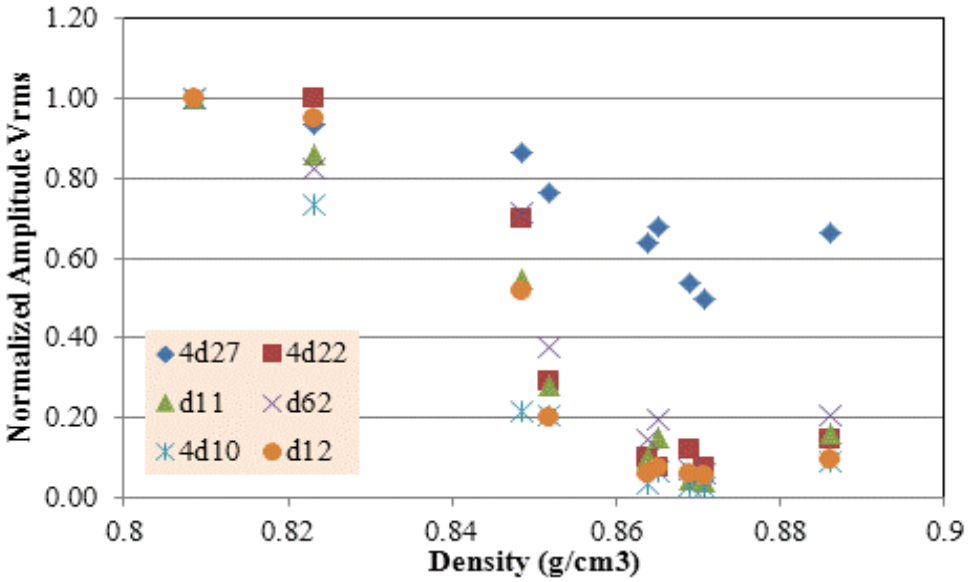

Figure 70. Normalized Vrms amplitude as a function of changes in density.

The relation to density is also shown in Figure 70 to indicate the same conclusions as with the previous analysis: no clear relation is seen in the membrane behavior with respect to changes in density.

Table 18 SUMMARY OF POWER FIT OF VRMS AMPLITUDE TO VISCOSITY AND R-SQUARE

ID	Size	Heater	Heater Size	Pass	Metal	Amp	Amp-Rsq
D11	2.5	P	16%	Yes_P	Yes_M	y=3.1528x^-0.629	0.972
D12	2.5	P	2%	Yes_P	Yes_M	y=2.7716x^-0.634	0.956
4D10	2.5	Poly	35%	No_P	No_M	y=2.6931x^-0.715	0.950
4D27	2.5	Poly	2%	Yes_P	Yes_M	y=1.2349x^-0.126	0.967
4D22	2.5	Poly	16%	Yes_P	Yes_M	y=3.134x^-0.586	0.883
D62	2.5	Poly	16%	No_P	No_M	y=2.7974x^-0.542	0.964

Chapter 10.

TEMPERATURE DEPENDENT MEASUREMENTS

The previous Chapter has demonstrated that this sensor can be used to measure the viscosity of a liquid at room temperature between 4 cSt and 800 cSt. This provides a useful sensor when the viscosity of a fluid needs to be monitored for any changes that happen at a constant temperature. Another very common application of viscometers is to characterize the temperature dependence of the viscosity of a fluid. It is often of interest to monitor the change in viscosity of a fluid as the temperature is increased in order to evaluate the rheological characteristics of this fluid. As introduced in Chapter 3, it is important to note the very strong correlation of oil viscosity with temperature. It follows the following Arrhenius relationship:

$$\eta = Ae^{-B/T} \tag{61}$$

where A and B are constants of the liquid that can be solved if the viscosity values are known at two different temperatures.

The effect of thermal impact on diaphragms has been extensively studied as presented in Chapter 3. These studies conclude that after an initial static deflection the diaphragm will vibrate at is natural frequency. The amplitude of the static deflection and the amplitude of the vibrations are proportional to the step heat input. Most of these studies simplify the diaphragm structure to a single material which is thermally excited

by an external source such as a laser [109]. The thermal effects on the vibration of such an idealized structure can be accomplished by analyzing the thermal sensitivities as they related to the device material and dimensions [110]. Such structure is easily analyzed but is not a realistic structure for a device with an in-situ heater. A device with an in-situ heater will need, at the very least, an electrical isolation layer and could also include a heater built with a different material than the diaphragm. Even though homogeneous multilayer diaphragms have been studied by analyzing the vibration behavior as the ambient temperature changes [111], this analysis is not valid when the layers that form the diaphragm are of different materials. Due to fabrication induced film stresses in the form of thermal and intrinsic stress, non-linear dependence is expected. This Chapter will explore the vibration behavior to changes in ambient temperature of non-homogeneous multilayer diaphragms that have been fabricated for fluid viscosity measurements.

This Chapter aims to study the effect of temperature on the vibration characteristics of a MEMS membrane actuated with an in-situ heater with the purpose of using this device as a viscosity sensor. In order to accomplish this we will first examine the vibration behavior of the silicon membrane in air at different ambient temperatures. We will examine different membrane compositions and whether these affect the temperature dependence. Secondly we will examine how the viscosity sensor sensitivity is affected by changing the temperature of the fluid being tested.

9.1 Unpackaged devices

Several devices were tested directly on a heated wafer chuck to study the effects of changing the ambient temperature on their free vibration characteristics. These devices

were not packaged as the epoxy used to attach the devices to the PCB's as well as to protect the wire bonds could create additional stress on the membrane as it becomes heated. The next Section looks at the effects of packaging.

The test set up with the LabView interface presented in Section 8.5 is used to collect several data points at each temperature setting. The devices were allowed to vibrate for a total of five minutes while the data was collected. This allowed for the temperature to stabilize and also allowed us to monitor and quantify any variation on the data.

The devices used for this study are listed in the Table below. The membrane composition details are listed as well as their free vibration frequency, the Q value and the FFT amplitude of the oscillations Vrms measured at room temperature. These values are typical of the devices studied previously in Section 8.6 and match the behavior observed during the analysis of the DOE presented in that Section with respect to membrane composition and heater material and size. It is important to note that the amplitude value used for the present analysis is the amplitude of the vibration Vrms and not the maximum peak to peak amplitude that was used during the DOE analysis. It has been explained before that the Vrms amplitude correlates to the quality factor of the vibration Q, whereas the maximum peak-to-peak amplitude depends on the power applied to get the membrane to vibrate. Since different powers were applied to the devices in order to obtain their best vibration response, it would not be appropriate to study this variable.

Table 19 DEVICES USED TO STUDY THE THERMAL EFFECTS ON THE VIBRATION OF SILICON BASED MEMBRANES.

ID	Size	Heater	Heater Size	Pass	Metal	Fo (Hz)	Qo	Vrms
4D36	2.5	P	16%	No_P	Yes_M	22815	29.83	2.00E-07
4D34	2.5	P	16%	Yes_P	No_M	22941	41.086	4.00E-06
4D25	2.5	Poly	2%	Yes_P	No_M	24057	19.759	3.00E-07
4D24	2.5	Poly	2%	No_P	Yes_M	21789	34.858	4.00E-06
4D27	2.5	Poly	2%	Yes_P	Yes_M	25118	35.018	9.00E-07
4D29	2.5	Poly	16%	Yes_P	Yes_M	15969	15.771	5.00E-06
4D7	2.5	Poly	35%	No_P	Yes_M	20983	17.64	1.00E-06
4D26	2.5	Poly	35%	No_P	Yes_M	21211	26.497	1.00E-07
4D30	2.5	Poly	35%	Yes_P	No_M	33613	52.625	5.00E-07

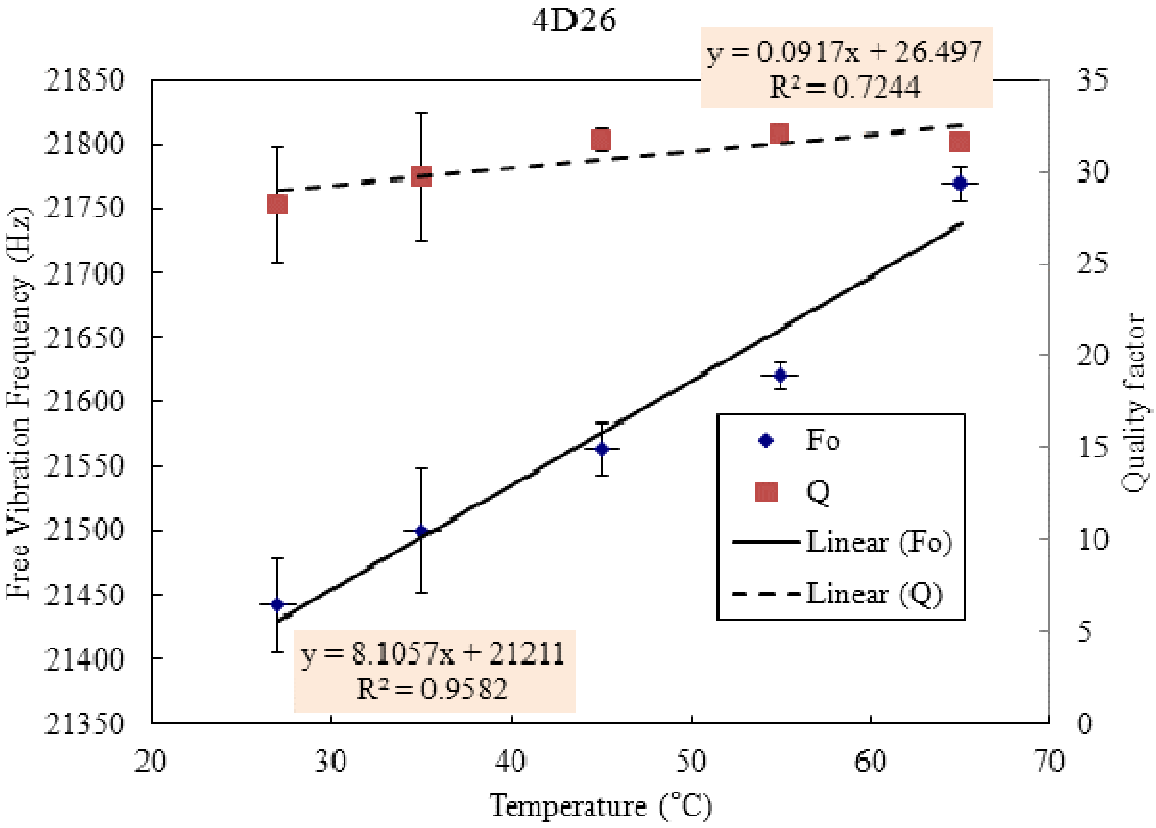

Figure 71. Typical response of the free vibration frequency to temperature.

A typical response to temperature is shown in Figure 71. Device 4D26 shows an increase of the vibration frequency with temperature. It also shows an increase of the vibration quality factor Q.

The analysis consists on fitting a linear equation to the data and on extracting the fit coefficients. To facilitate the analysis the initial Fo and Qo presented in Table 19 are those of the equation fit, at the x-axis intercept (at 0 ºC). These values will be used to normalize the fit coefficients so that the behavior of the different devices can be compared.

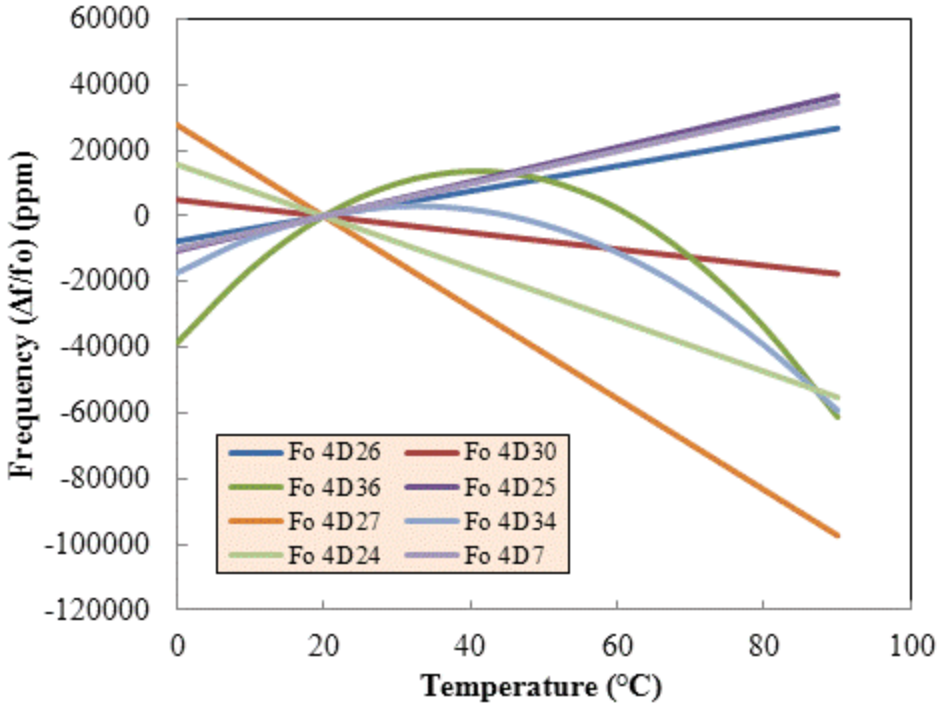

Figure 72. Temperature sensitivity of normalized frequency of tested devices.

Plotting the temperature response using the fitting equations gives us an idea of the different expected behaviors of the devices studied. This is seen in Figure 72. Devices 4D27 and 4D24, both with 2% polysilicon heaters show an important decrease in frequency as the devices are heated. Device 4D36 and 4D34 show a quadratic behavior with an inflexion point at around 40 °C. This behavior could indicate the effect of thermal stress created during the fabrication process. These two devices have a 16% p+-diffused heater, one with additional SiO_2 and the other one with aluminum for bimetal enhancement. These four devices show important dependence on temperature that may

make them not suitable to measure temperature-induced viscosity changes of fluids. The rest of the devices which have 35% polysilicon heaters show temperature variations in the range of -250 ppm / °C to 523 ppm / ºC. These values are large when compared to silicon-only resonators, which have been shown to be in the range of -30 to -60 ppm / °C [110,112]. These reported values are based on simple silicon structures and account mainly for the change in the Young's modulus of silicon with temperature. The larger temperature dependence observed in our devices is due to the combination of different materials and their interactions with temperature. It is important to keep in mind that our membranes are composed of Si, SiO_2, polysilicon and aluminum for interconnects and in some devices as a bimetallic layer.

A summary of the frequency dependence on temperature for the devices tested is shown in Table 20 ranked from most negative to most positive dependence.

Table 20 SUMMARY OF FREQUENCY SENSITIVITY TO TEMPERATURE

ID	Size	Heater	Heater Size	Pass	Metal	F(T)	$F(T^2)$
4D27	2.5	Poly	2%	Yes_P	Yes_M	-1.4E-3	
4D24	2.5	Poly	2%	No_P	Yes_M	-788.4E-6	
4D30	2.5	Poly	35%	Yes_P	No_M	-250.6E-6	
4D26	2.5	Poly	35%	No_P	Yes_M	382.1E-6	
4D7	2.5	Poly	35%	No_P	Yes_M	495.4E-6	
4D25	2.5	Poly	2%	Yes_P	No_M	523.9E-6	
4D34	2.5	P	16%	Yes_P	No_M	1.2E-3	-19.0E-6
4D36	2.5	P	16%	No_P	Yes_M	2.6E-3	-31.2E-6
4D29	2.5	Poly	16%	Yes_P	Yes_M	5.6E-3	

The basic equation that defines the natural frequency of a simply-supported membrane is shown in (62). When analyzing this equation, we find that when the dominating factor is a decrease of the Young's modulus of silicon, the frequency will

tend to decrease. This happens with the devices that have small polysilicon heaters and larger ones with no bimetallic aluminum. Changes in dimension will not be as dominating as the thermal expansion coefficient of silicon at room temperature, 2.6 ppm / ºC, is 10 times smaller than the expected change in Young's modulus. On the other hand, the change in Young's modulus of SiO_2 seems to become important as it has been reported to have a value of 185 ppm / ºC, opposite and larger than that of silicon [113]. The presence of a top layer of metal as both interconnects and to enhance the vertical displacement, will also complicate the analysis. Aluminum has a large temperature dependence of Young's modulus of -500 ppm / ºC. Finally, the fabrication-induced thermal and intrinsic stress of the SiO_2, polysilicon and aluminum layers seem to lead to an increase in frequency with temperature.

$$f = \frac{19.74}{2\pi a^2}\left[\frac{Eh^3}{12\rho h\left(1-\nu^2\right)}\right]^{1/2} \tag{62}$$

Devices with p+-diffused heaters exhibit a quadratic behavior which indicates that the combined effects of the changes in stress lead to an initial increase in frequency which is later overcome by the Young's modulus change in silicon at higher temperatures, which leads to a decrease in frequency.

Similarly, devices which show a linear increase in frequency with temperature are dominated by the combined effects of the fabrication-induced stress as well as the change in Young's modulus of SiO_2.

We can remove the effect that the presence of metal has on the behavior of the devices by analyzing the following sensors: 4D30, 4D25 and 4D34. These devices have the same material composition which includes a 15 μm silicon membrane, sandwiched between a 1 μm of SiO_2 on the bottom and a 3.5 μm SiO_2 on the top. The only variation

is the amount of polysilicon which is located on the first 0.5 μm of SiO_2 on top of the membrane as seen Figure 11. 4D30 has the largest polysilicon layer covering 35% of the membrane area, and is shows a negative thermal dependence of frequency of -250 ppm. Device 4D25, with only a 2% polysilicon heater shows a positive thermal dependence of + 524 ppm. Lastly, device 4D30 with no polysilicon, shows an even larger positive thermal dependence of + 1200 ppm which turns into a quadratic behavior at temperatures above 40 °C. Without the presence of the additional metal plate, the temperature dependence of frequency becomes more positive as the presence of polysilicon is removed. This would correlate with the fact that SiO2 has a positive temperature change in Young's modulus.

Regardless of the behavior of the sensor with temperature, an initial test in air is necessary if one intends to use frequency an indicating factor of changes in fluid viscosity. The effect of viscosity in frequency will then need to be adjusted by removing the effect of temperature. As such, devices with the smallest temperature dependence are preferred.

The effects of temperature on Q have been reported in the literature as being up to 1% / ºC due to thermo-elastic dissipation and damping on silicon cantilever beam resonators [104]. Even with this large variation in Q due to temperature, the changes expected due to the fluid viscosity changing is expected to be much larger. It is also expected to decrease with viscosity as shown in the previous Section.

Figure 73 shows the temperature dependence of quality factor of several devices. As seen with the frequency some devices will tend to linearly increase with temperature, others decrease and others to follow a quadratic behavior.

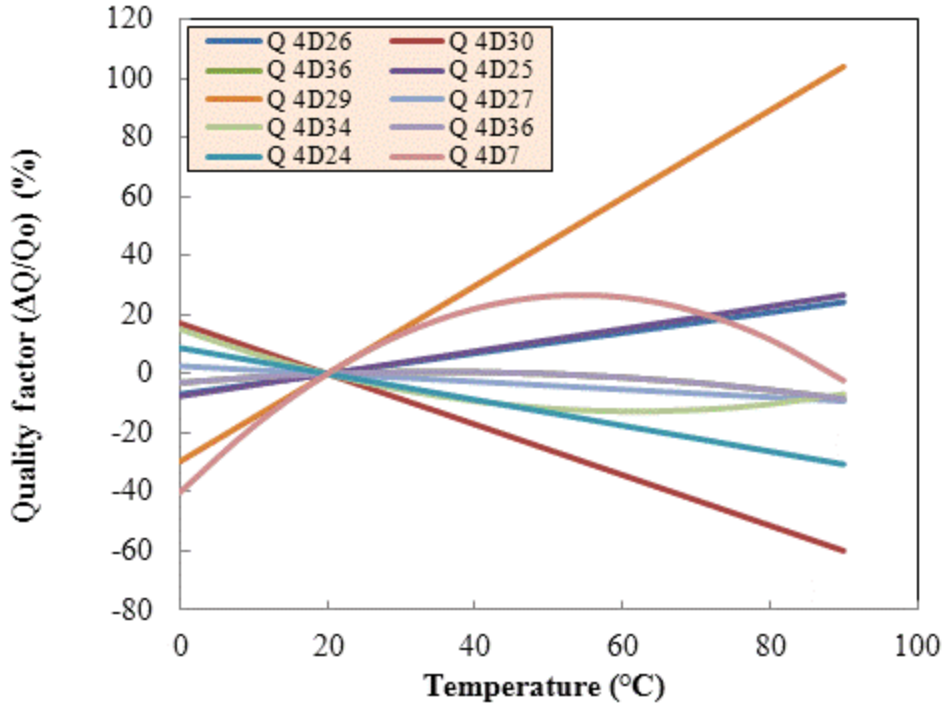

Figure 73. Temperature sensitivity of normalized Q of tested devices.

The quality factor, Q is dependent on thermoelastic dissipation. As the membrane flexes, strain gradients result in temperature gradients inside the membrane. This temperature gradients lead to thermal transport which leads to fast energy dissipation and limits Q. The material properties such as thermal expansion coefficient $\boldsymbol{\alpha}$, specific heat $\boldsymbol{C_p}$ and thermal conductivity $\boldsymbol{k}$ dominate this effect. These material properties tend to rapidly increase with temperature with the exception of thermal conductivity which tends to decrease slightly. As such, Q is expected to decrease with temperature. This dependence is shown in Equation 63 below [104,110].

$$Q = \left(\frac{f_M^2 + f_T^2}{f_M f_T} \right) * \frac{C_p \rho}{\alpha^2 T E} \tag{63}$$

where $$f_T = \frac{\pi k}{2 C_p \rho h^2} \tag{64}$$

On the other hand, as the quality factor Q is also dependent on the mechanical frequency of vibration f_M, the devices that show a strong increase in frequency with temperature will still show an increase in Q while others may exhibit a quadratic behavior as one effect overtakes the other.

As such, a listing of the fit or linear or quadratic parameters remains in the same order as the frequency one, from most negative to most positive, with a few devices which were originally positive becoming negative or quadratic in behavior. This is presented in Table 21

Table 21 SUMMARY OF Q SENSITIVITY TO TEMPERATURE

ID	Size	Heater	Heater Size	Pass	Metal	Q(T)	$Q(T^2)$
4D27	2.5	Poly	2%	Yes_P	Yes_M	-1.32E-03	
4D24	2.5	Poly	2%	No_P	Yes_M	-4.38E-03	
4D30	2.5	Poly	35%	Yes_P	No_M	-8.56E-03	
4D26	2.5	Poly	35%	No_P	Yes_M	3.46E-03	
4D7	2.5	Poly	35%	No_P	Yes_M	2.46E-02	-2.27E-04
4D25	2.5	Poly	2%	Yes_P	No_M	3.80E-03	
4D34	2.5	P	16%	Yes_P	No_M	-9.02E-03	7.30E-05
4D36	2.5	P	16%	No_P	Yes_M	2.11E-03	-3.02E-05
4D29	2.5	Poly	16%	Yes_P	Yes_M	1.49E-02	

The normalized slope of this temperature dependence is quite large but it is generally linear. It ranges from -8 %/ºC to + 2.4 %/°C. The expected response to viscosity with increasing temperature is expected to follow a power law and be much more significant according to the results presented in Chapter 9. In any case, devices that exhibit a large negative dependence or large quadratic behavior will be avoided as they would confound the viscosity measurements.

9.2 Packaged devices

In M. Hopcroft PhD dissertation, completed in 2007, the temperature sensitivity of a silicon beam resonator was studied in detail. The temperature effects on frequency and Q factor of such resonators were analyzed in terms of changes to the material elasticity (Young's modulus), dimensional changes and stress. Hopcroft concluded that for resonators which were mechanically isolated from the substrate, the material elasticity change was the most important at effect to changes in frequency at -31.9ppm/ºC. Packaging stress was the most important factor affecting resonant behavior of devices which were not isolated from the substrate as is the case in our analysis. His single anchor devices, which were only held by the substrate at one point, thus becoming isolated from the substrate, showed 5-6x lower sensitivity to temperature compared to his double anchor devices, which were held by the substrate at two locations, thus being affected by compressive or tensile forces produced in the interface between the substrate and the package [110].

In order to ascertain the effect of packaging on our sensors several devices that were previously tested on a wafer chuck were packaged. They were glued to a PCB with epoxy, wire bonded and tested again for their temperature sensitivities. This PCB has a hole drilled on the back so that both surfaces of the sensor are exposed to the fluid. Then, they were encapsulated with additional epoxy and tested again to analyze any changes on their temperature sensitivities. The encapsulating epoxy covered the wire bonds as well as the perimeter of the chip as shown in, but not the membrane which must remain exposed so that it can interact with fluid.

Figure 74 shows the sensor packaging sequence. The top picture show the PCB with the access hole for the back of the membrane. The middle picture shows the device wire-

bonded and glued to the PCB. The bottom picture shows the device wire-bonds covered with epoxy.

A typical response of the results is presented in Figure 75. Device 4D7 showed a sensitivity of 488 ppm/ºC when tested without any packaging. After it was attached to a PCB with epoxy and wire bonded for contacts the sensitivity increased slightly to 671 ppm/°C. Encapsulating the wire bonds and the edge of the chip with additional epoxy increased the sensitivity again to about 815 ppm / ºC. The total sensitivity increase was around 2X. This is a significant increase in sensitivity to temperature and must be taken into account when analyzing the frequency response to viscosity with changing temperature. These results are typical independently of the membrane composition as shown in Table 22 and Table 23

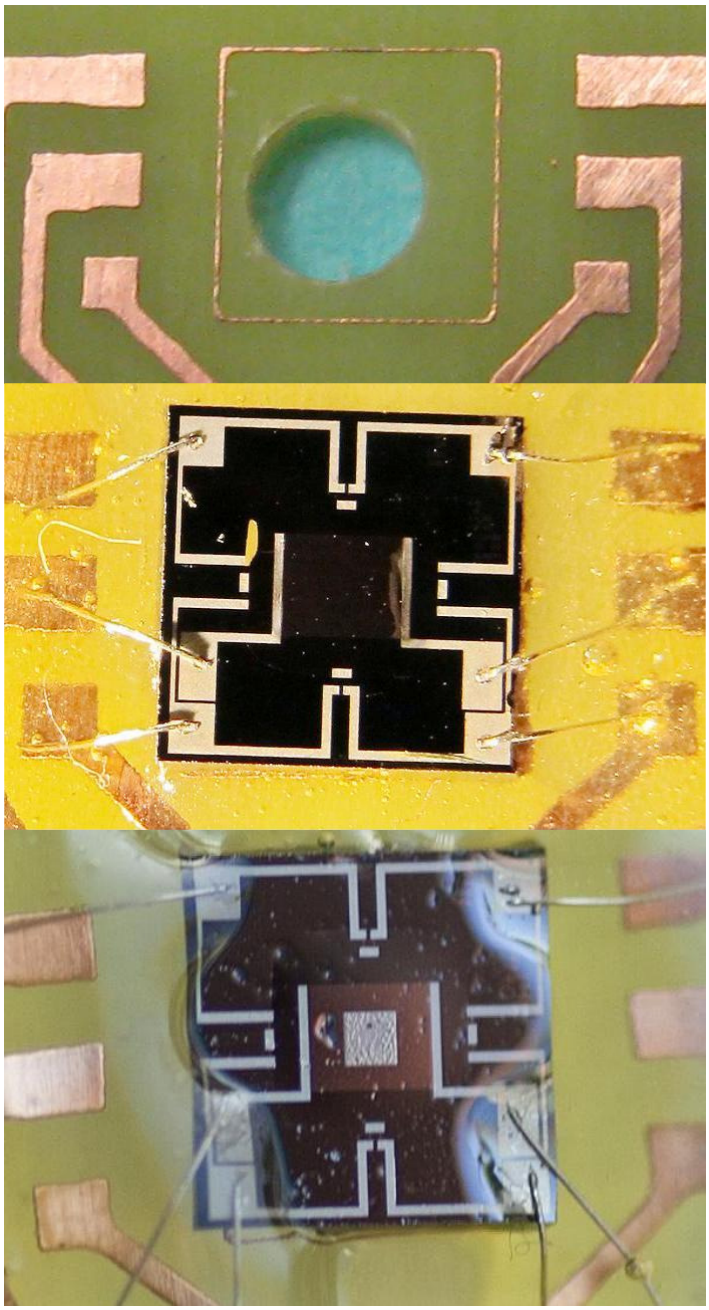

Figure 74. Sensor packaging sequence.

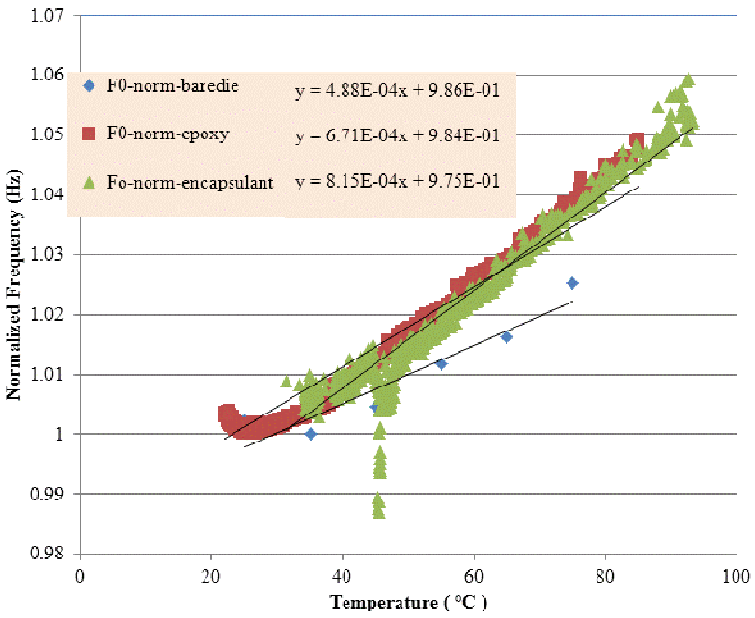

Figure 75. Temperature senstivitiy of frequency of device 4D7 due to packaging.

Table 22 SENSTIVITY OF FREQUENCY TO TEMPERATURE DUE TO PACKAGING

					Frequency (T)		
ID	Heater	Heater Size	Pass	Metal	Bare die	Epoxy	Encap.
4D34	P	16%	Yes	No	4.50E-04	7.16E-04	1.42E-03
4D27	Poly	2%	Yes	Yes	-1.56E-03	-2.93E-03	-2.62E-03
4D24	Poly	2%	No	Yes	-8.05E-04	-1.80E-03	-2.22E-03
4D29	Poly	16%	Yes	Yes	4.90E-03	1.20E-03	1.01E-03
4D7	Poly	35%	No	Yes	4.88E-04	6.71 E-04	8.15E-04

Table 23 CHANGES OF SENSTIVITY OF FREQUENCY TO TEMPERATURE DUE TO PACKAGING

					F(T) Ratios		
ID	Heater	Heater Size	Pass	Metal	Bare die	Epoxy	Encap.
4D34	P	16%	Yes	No	1.000	1.591	3.156
4D27	Poly	2%	Yes	Yes	1.000	1.878	1.679
4D24	Poly	2%	No	Yes	1.000	2.237	2.756
4D29	Poly	16%	Yes	Yes	1.000	0.245	0.206
4D7	Poly	35%	No	Yes	1.000	1.731	1.821

On the other hand, the quality factor sensitivity to temperature decreases with packaging. This is explained by the same effects described in the previous Section. Most of the devices involved in this study showed positive temperature sensitivity of their natural frequency of vibration. Their vibration frequencies increased as temperature was increased. Packaging, with the exception of 4D29, increased this sensitivity to temperature even further. This farther increase in mechanical frequency is counteracted by the decrease in thermal frequency that the membrane is also experiencing. As such the quality factor tends to show less sensitivity to temperature. 4D29 did not see an increase in sensitivity but it still remained with a positive sensitive to temperature leading to the same effect. On the other hand, the devices that showed negative temperature coefficient of vibrating frequency (4D27 and 4D24) showed an increase in Q sensitivity to temperature as they were packaged, due to the thermal frequency dominating this effect and not being counteracted by the increase in mechanical frequency.

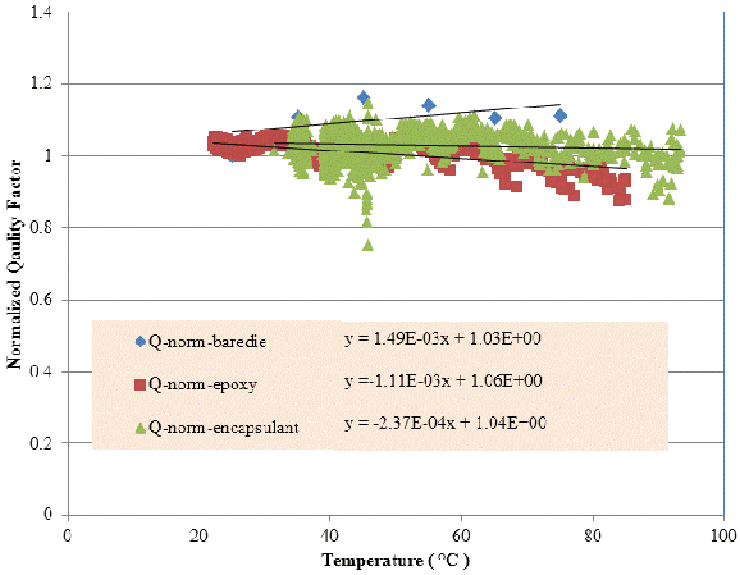

Figure 76. Temperature senstivitiy of quality factor Q of device 4D7 due to packaging.

Figure 76 shows the response of quality factor through packaging from device 4D7. Its sensitivity to temperature is reduced as the device is packaged due to the simultaneous increased sensitivity of the natural frequency of oscillation. A summary of the linear sensitivity of these devices and how they compare to their original values is shown in Table 24 and Table 25 As mentioned before, with the exception of the devices which show negative temperature dependence of their natural frequency, all the other devices showed a decrease in the sensitivity of the quality factor.

Table 24 SENSTIVITY OF Q TO TEMPERATURE DUE TO PACKAGING

					Quality Factor (T)		
ID	Heater	Heater Size	Pass	Metal	Bare die	Epoxy	Encap.
4D34	P	16%	Yes	No	3.22E-03	7.32E-04	1.43E-03
4D27	Poly	2%	Yes	Yes	-1.37E-03	4.43E-03	8.21E-03
4D24	Poly	2%	No	Yes	-5.24E-03	-1.48E-03	-5.42E-03
4D29	Poly	16%	Yes	Yes	1.10E-02	1.29E-03	3.90E-03
4D7	Poly	35%	No	Yes	1.49E-03	1.11E-03	-2.37E-04

Table 25 CHANGES OF SENSTIVITY OF FREQUENCY TO TEMPERATURE DUE TO PACKAGING

					Q(T) Ratios		
ID	Heater	Heater Size	Pass	Metal	Bare die	Epoxy	Encap.
4D34	P	16%	Yes	No	1.000	0.227	0.444
4D27	Poly	2%	Yes	Yes	1.000	-3.234	-5.993
4D24	Poly	2%	No	Yes	1.000	0.282	1.034
4D29	Poly	16%	Yes	Yes	1.000	0.117	0.355
4D7	Poly	35%	No	Yes	1.000	0.745	-0.159

Even though packaging shows and improvement on the quality factor sensitivity to temperature, the absolute variation is still large. Q temperature sensitivity values between -5% / °C and 8% / ºC have been observed during this study.

9.3 Temperature-Dependent viscosity measurements

Once we have established the behavior of the sensors with changing temperatures we are ready to perform viscosity measurements on motor oil as we change its temperature. As mentioned above a very common application of viscometers is to characterize the temperature dependence of the viscosity of a fluid. It is often of interest to monitor the change in viscosity of a fluid as the temperature is increased in order to evaluate the rheological characteristics of this fluid. As introduced in Chapter 3, it is important to note the very strong correlation of oil viscosity with temperature. It follows the following approximate Arrhenius relationship:

$$\eta = Ae^{-B/T} \tag{65}$$

where A and B are constants of the liquid that can be solved if the viscosity values are known at two different temperatures.

An advantage to using motor oil for this test is that it provides a non-conductive media that does not require electrical isolation of the sensor interconnects. Another advantage is that we can test a wide range of viscosities just by changing the temperature of the oil without introducing any cross contamination of fluids or any other external variables. A disadvantage is that the frequency and quality factor of the oscillation of the sensor will also change with temperature as described in the previous section. Thus, the temperature effect will need to be subtracted from the natural frequency and Q shift to obtain an accurate measurement of viscosity.

The temperature vs. viscosity plots of three different oils is presented in Figure 77. Impact Technologies LLC using a Brookfield DV-II+Pro cone-and-plate viscometer took these measurements. Table 26 presents the specification data for these oils, which are provided by the manufacturers.

Table 26 SPECIFICATIONS OF MOTOR-OIL TESTED

	5W30	**10W40**	**SAE60**
Density (60 F)	0.876 kg/l	0.8713 kg/l	0.8931 kg/l
Viscosity 40C	57.2 cSt	109.7 cSt	293.4 cSt
Viscosity 100C	10.5-11.2cSt	14.0 cSt	24.0 cSt
Viscosity Index	176	146	104

5W30 and 10W40 oils are multi-grade oils; as such their viscosity change over temperature is not as significant as the single grade SAE60 oil. Note the strong temperature dependence of the viscosity of SAE60. At the higher operating temperature

of 100 °C, the viscosity of the oils converge to a small range of 10 – 25 cP as their specification show in Table 26 and determined by the standards of Table 1

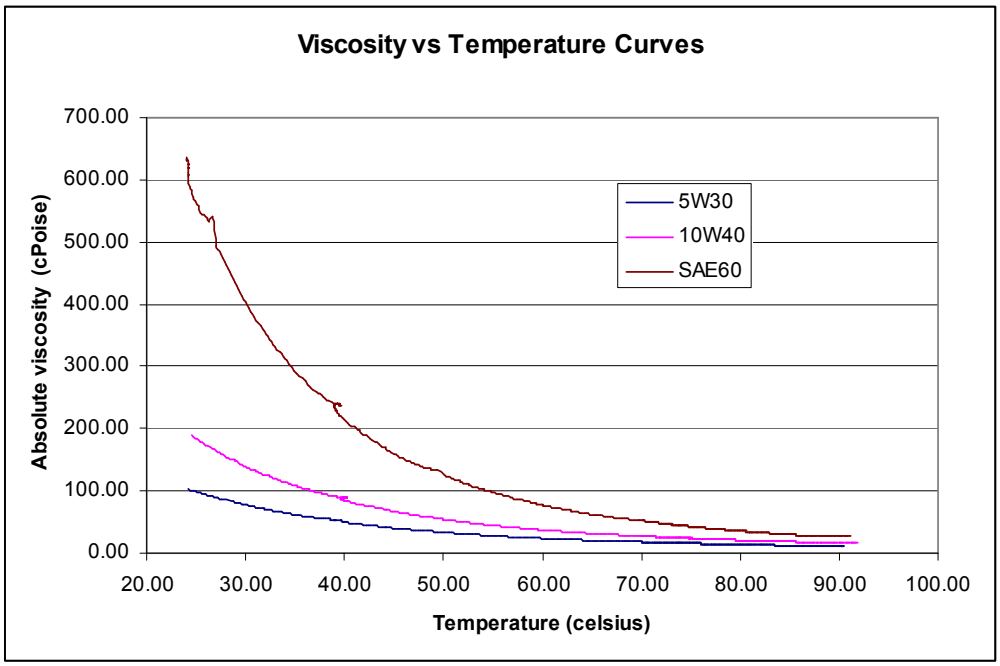

Figure 77. Viscosity-temperature curves for 3 types of motor oil.

Based on the knowledge obtain from the previous sections we will only choose sensors which exhibit a moderate temperature dependence of natural frequency and quality factor in air. Moderate numbers are less than 0.5% / °C for frequency variation and less than 5% / ºC for Q variation. Devices with quadratic behaviors will also be avoided.

Device D25 was chosen for its relatively low temperature sensitivities. This device has a polysilicon heater which covers 35 % of the area of the membrane, a top aluminum plate for additional actuation enhancement but no additional passivation. The natural frequency of vibration of this device increased linearly with temperature at a rate of 0.131% / °C. The quality factor increased linearly with temperature at a rate of 0.45 % / °C. Device D25 was tested in single-grade SAE60 motor oil as its viscosity was

decreased by increasing its temperature. Single grade mineral oils are generally Newtonian in behavior and their viscosity is usually not related to the shear rate. Furthermore, the rate of shear used to measure the viscosity of this fluid is kept within a narrow range for which its behavior should remain Newtonian.

The sensor was glued and wire bonded to a PCB board with an access hole drilled on its back. Thus, both surfaces of the diaphragm are in direct contact with the fluid to be tested. Figure 79 shows the results of testing device D25 in SAE60 as the temperature is increased. The method for determining the frequency of vibration and the quality factor was outlined in the previous sections. The data collection method was automated through the use of National Instruments' LabView to obtain real time temperature of the oil as well as the corresponding frequency and quality factor of the vibrating sensor. Figure 78 shows FFT results of device D25 tested in SAE60 as it is heated. This data helps us visualize how the FFT measurements evolve over the course of the measurements as the oil is heated and the viscosity is decreased. Both the natural vibration frequency and Q increase as the temperature increases and the viscosity and density of the oil decrease. The estimated error for the natural vibration frequency was less than 1% of measurements at higher temperatures where the viscosity is lower and up to 5% at lower temperatures where the viscosity is higher. The error bars are barely noticeable in the frequency values in Figure 79. On the other hand, the measurements for the quality factor Q show larger variation.

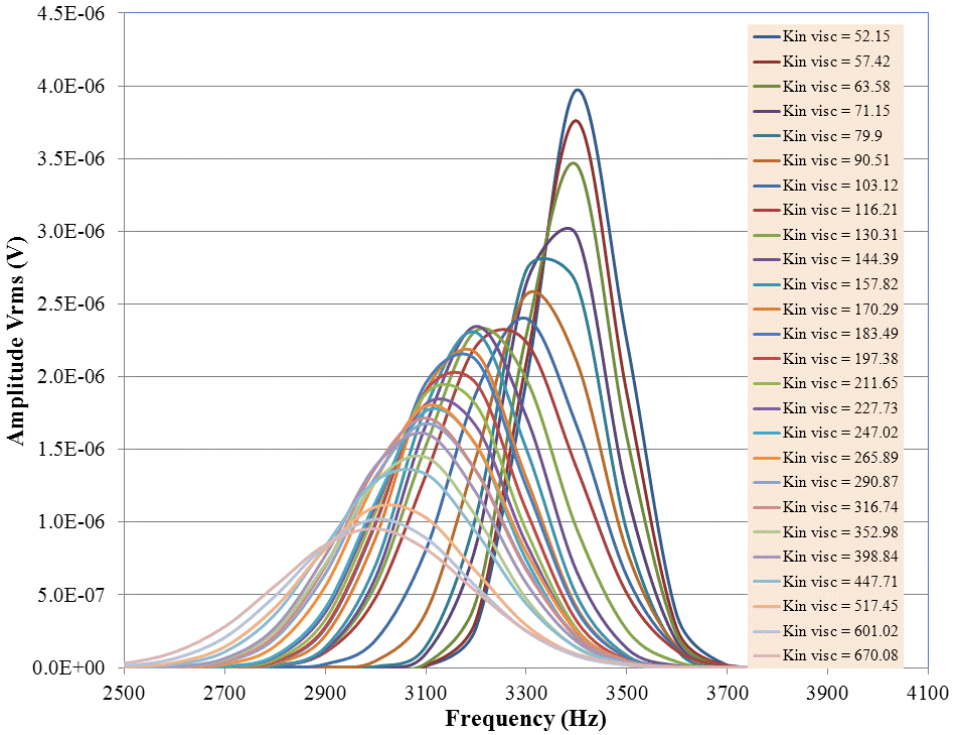

Figure 78. FFT progression of device D25 as the temperature of motor oil SAE60 is increased and the viscosity is decreased.

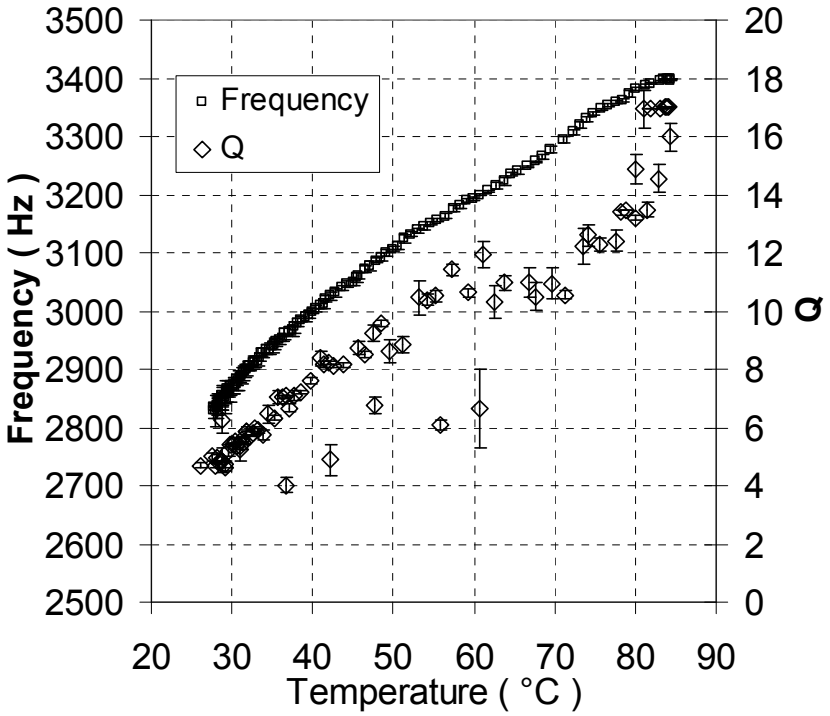

Figure 79. Device 25. Natural frequency and Q variation vs. SAE60 temperature.

During these measurements, the increase in natural vibration frequency and quality factor are influenced by three factors: i) the increase in temperature, as measured in the previous section, ii) the decrease in density and iii) the decrease in viscosity.

The effect that the temperature has on the vibration frequency and Q factor can be removed based on measurements of the sensor in air while changing the temperature. The frequency of vibration of this device increased with temperature at a rate of 0.131% / °C. The quality factor increased with temperature at a rate of 0.45 % / °C. The changes in density and viscosity due to temperature can be accounted for by plotting the results versus the kinematic viscosity. The kinematic viscosity is defined as the ratio of dynamic viscosity and density and is a more appropriate metric for our sensor since the moving membrane also displaces the fluid under test. The dynamic viscosity of the SAE60 oil as a function of temperature was previously obtained using a commercial Brookfield DV-II+ Pro cone-and-plate viscometer. The change in natural vibration frequency and Q with respect to the kinematic viscosity of the oil is plotted in Figure 80. On this plot, only the effect that the kinematic viscosity has on the natural vibration frequency and Q is shown. As expected, the natural vibration frequency decreases when the viscosity increases. The Q value also decreases but at a much larger rate. These results are consistent with those obtained at room temperature and presented in Chapter 9.

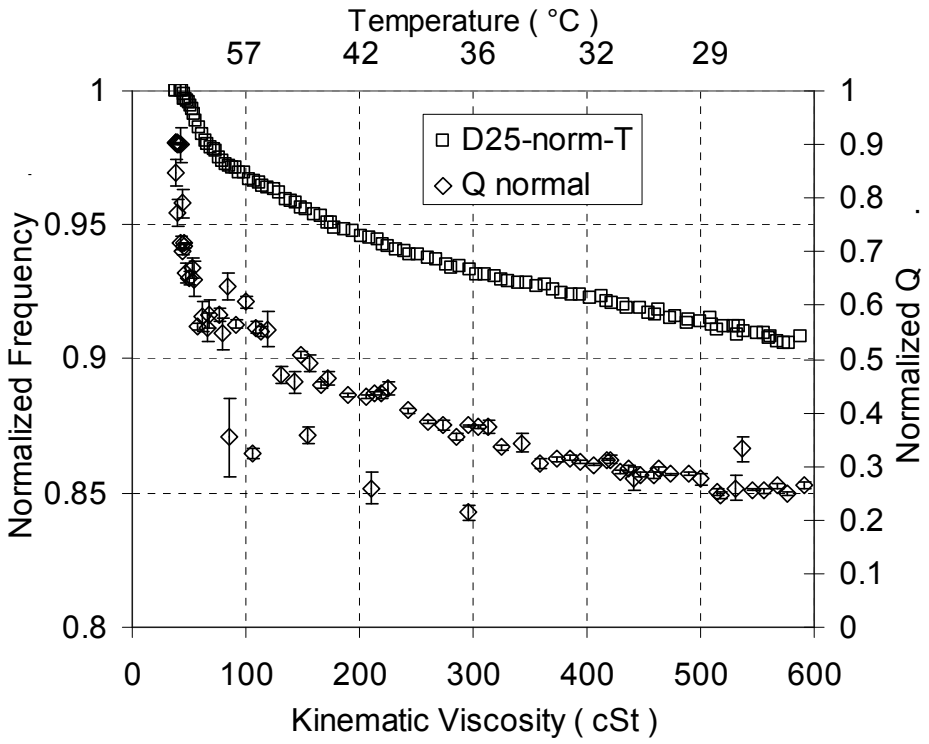

Figure 80. Normalized frequency of vibrations and Q with respect to kinematic viscosity and temperature of the oil.

We now compare the obtained results to both Lamb's and Kozlovsly's models in Figure 81. Lamb's model predicted a change in vibrating frequency only due to the change in density of the fluid. This model has been verified as accurate in several studies with larger membranes and fluids of low viscosities [93], [94], [95], [96]. Kozlovsky's model accounts also for changes in viscosity. Over the range of temperatures and kinematic viscosities studied, Lamb's model predicts a change in natural vibration frequency, which is due to only the change in oil density, of approximately 2%, according to (32). Kozlovsky's model predicts a change of 5% by taking into account the viscous forces as in (34). The results show the expected general behavior described by both theoretical models. At lower viscosities the natural frequency of vibration changes more rapidly. Over 100 cSt it starts to level off. The actual results obtained indicate a

change of 9%, which is larger than the predicted by either model but it leads to the conclusion that the change in density alone could not account for such a large change. It is important to remember that, for the range of values studied, the kinematic viscosity changes by over two orders of magnitude, from 40 cSt to 600 cSt. On the other hand, over this same range, the density only changes by 5%, from 833 kg / m^3 to 870 kg / m^3 [114].

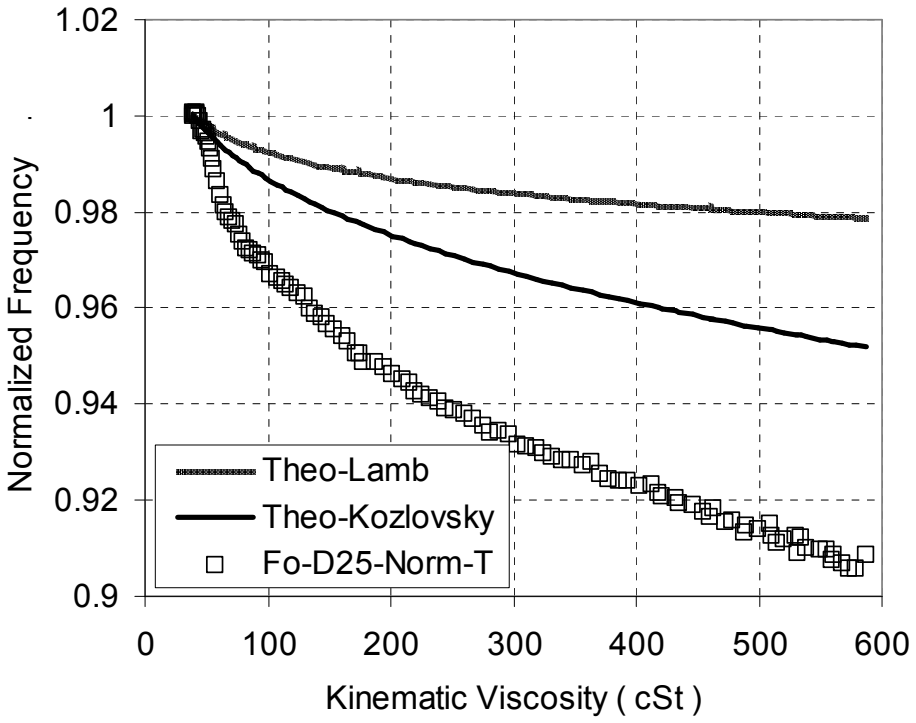

Figure 81. Comparison of Lamb and Kozlovsky's models to experimental data.

Utilizing Kozlovsky's model as presented in (35) and (36), we can also observe the energy dissipation factor Q as a function of kinematic viscosity. Figure 82 compares the obtained results to the predicted values. In this case, the change in Q fits the predicted values well, although it indicates a certain degree of variation especially at lower viscosities. Q decreases significantly as the viscosity of the fluid is increased.

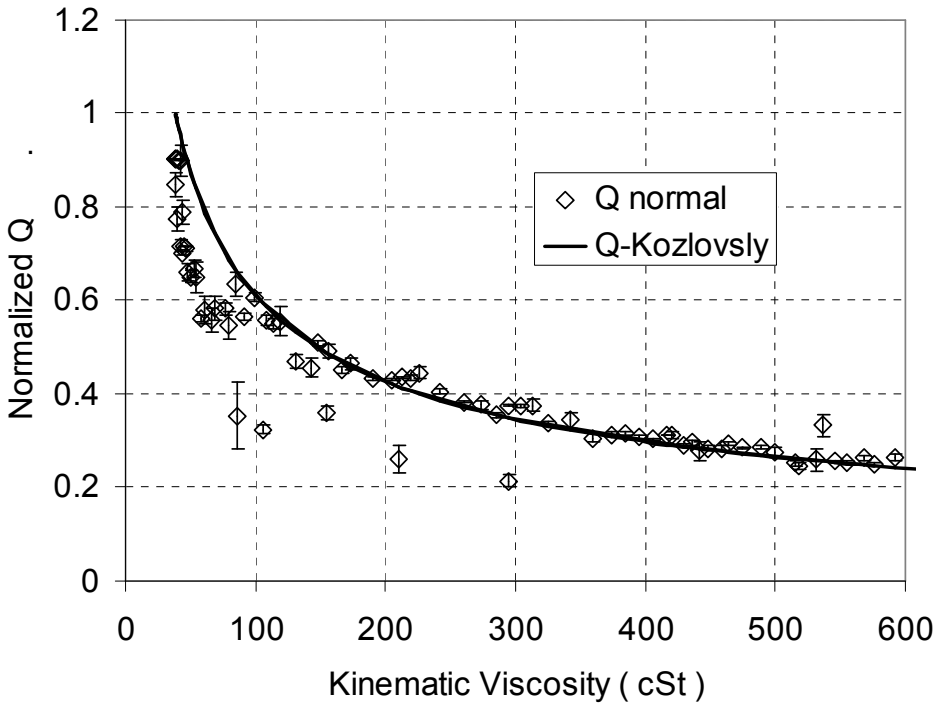

Figure 82. Comparison of Kozlovsky model for Q-value to experimental data.

These results are consistent with those obtained at room temperature in Chapter 9. This demonstrates that both room temperature and elevated temperature measurements can be made with the proposed thermal actuated MEMS sensor. Further thermal calibration needs to be done with the device structures to fully understand the thermal dependence of the vibration and if possible reduce this sensitivity so that the effects of viscosity are dominant. Possible ways of reducing this is by carefully studying the effects of the thickness of SiO2 passivation such as in [113] where Si beams were encapsulated with SiO2 in order to reduce the resonance dependence on temperature variation.

Other devices were tested with the same methodology. The devices chosen with low temperature dependence variables resulted in correlation to viscosity changes. On the other hand, and as expected, devices with high temperature dependencies did not have enough sensitivity to viscosity changes. Table 27 shows the devices tested and their

characteristics along with their temperature sensitivities in air. This list is ordered from negative to positive values of frequency sensitivity to temperature. The devices with the lowest absolute values showed the best results when measuring viscosity. The devices with large sensitivities to temperature did not correlate to viscosity changes.

Table 27 LIST OF DEVICES TESTED IN HEATED OIL WITH THEIR TEMPERATURE SENSITIVITIES IN AIR.

ID	Heater	Heater Size	Pass	Metal	Linear Fo(T)	Linear Q(T)
4D21	Poly	16%	No	No	-7.04E-04	2.10E-03
D43	**Poly**	**35%**	Yes	No	**-8.75E-04**	**-5.22E-03**
4D10	**Poly**	**35%**	No	No	**-4.5E-05**	**3.76E-02**
4D7	**Poly**	**35%**	No	Yes	**8.36E-04**	**-2.27E-04**
4D29	Poly	16%	Yes	Yes	1.23E-03	-1.89E-03
D25	**Poly**	**35%**	No	Yes	**1.44E-03**	**4.51E-03**
4D34	**P**	**16%**	Yes	No	**1.44E-03**	**2.08E-03**
4D15	**Poly**	**16%**	No	Yes	**8.76E-03**	**1.80E-02**
D43	**Poly**	**35%**	Yes	No	**-8.75E-04**	**-5.22E-03**
4D22	**Poly**	**16%**	Yes	Yes	**1.17E-02**	**4.30E-03**

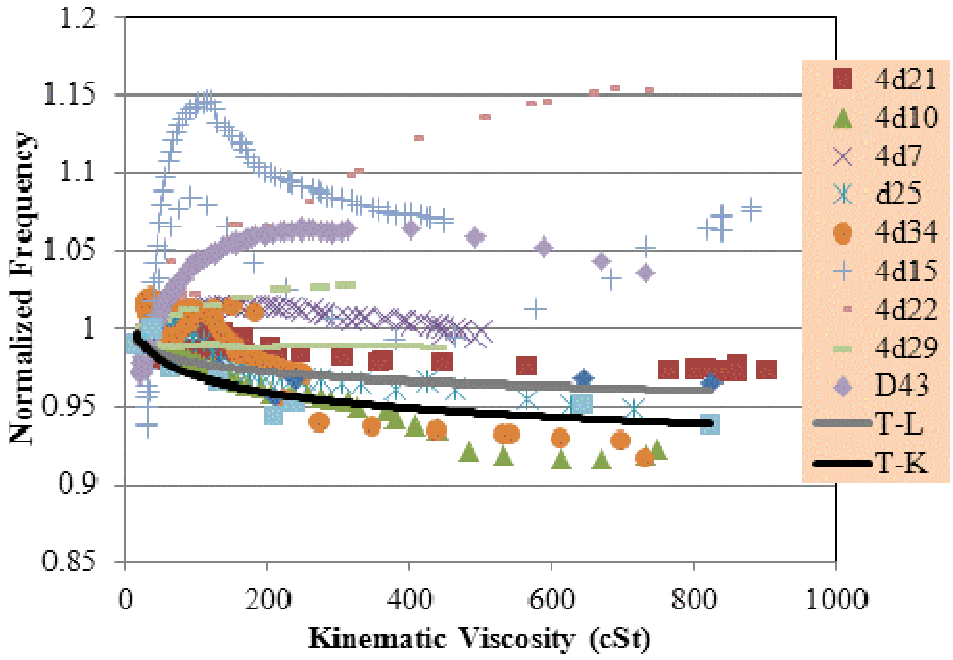

Figure 83. Summary of normalized frequency with changing viscosity.

Figure 83 shows the normalized response of the frequency of vibration to viscosity when the temperature effect has been removed for the devices listed in Table 27 The response has been normalized to 40 cSt. As can be seen, several devices show a decrease in frequency with increasing viscosity as predicted by Kozlovsky's theory. On the other hand, we can also observed some devices with very little variation and others which actually increase in frequency. The devices with very little variation could be responding to only changes in density, which are small and predicted by Lamb's theory. The devices with increasing frequency could be responding to other factors such sensor defects, sensor postioning or other factors.

Devices 4D7, D43, 4D15 and 4D22 increase in frequency with increasing viscosity. 4D15 and 4D22 have a range of frequencies of 2,000 Hz and lower. D43 has a complex membrane with large poly plate and additional passivation. It shows a quadratic effect where the frequency starts to incrase and the decreases as the viscosity is increased.

Additional thermal effects could have not been taken into effect or the mebrane could have been stress from the test in air to the test in oil and changed its intrinsic stress and interaction between the materials in contact.

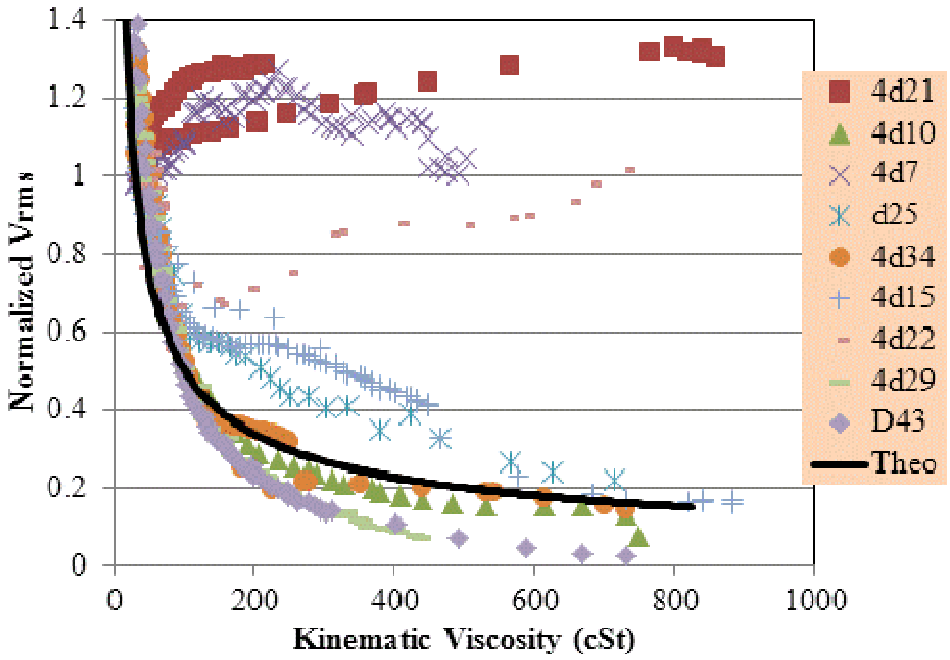

Figure 84. Summary of normalizedVrms–a function of Q – with changing viscosity.

Figure 84 shows the response of these same devices for the FFT **Vrms** factor, which is an indication of the quality factor, as described above. Two general behaviors can be observed.

4D7 and D25 are identical devices, but one shows an increase in **Vrms** while the other shows the predicted behavior. 4D7 has also showed a frequency increase with viscosity which could have indicated a change in membrane behavior and possibly damage or change on the device intrinsic stress and conditions. The FFT sequence of 4D7 is show in Figure 85. It can be observed that the amplitude initially increases with temperature but then decreases. This behavior is due to material interaction within the

membrane as it is heated. This strong temperature effect seems to lead to permanent changes in the internal stress of the membrane and makes it difficult to predict in order to extract the effect of viscosity alone.

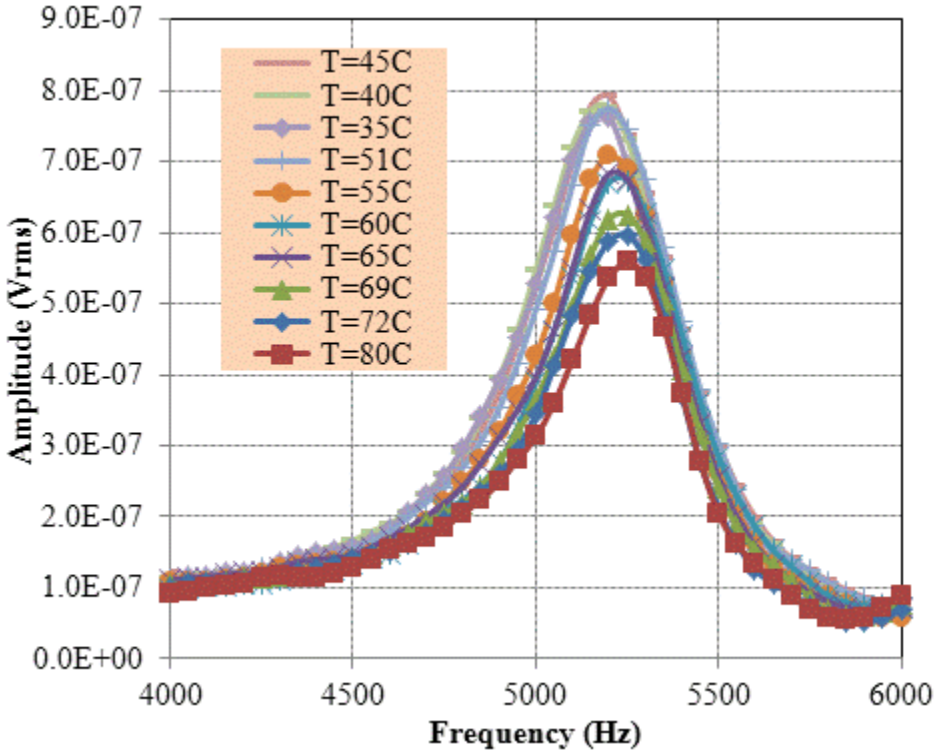

Figure 85. FFT progression with increased temperature of 4D7 in 10W40.

4D21 shows a similar behavior where the frequency had also shown a quadratic behavior. 4D21 could have also been damaged since it shows a non-linear response to temperature and also as significant hysteresis as it is heated and cooled down but especially at elevated temperatures as shown in Figure 86, indicating structural change due to the heating process. As a contrasting result device 4D29 shows a linear response to change in temperature as shown in Figure 87.

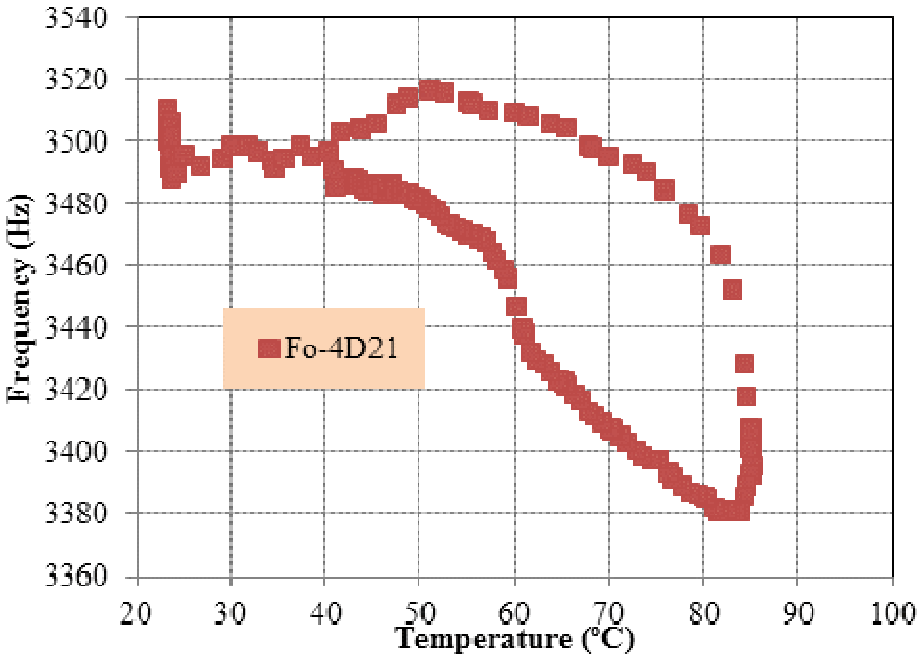

Figure 86. 4D21 hystheresis

Reliability concerns have been raised on vibrating MEMS cantilevers in liquid media. Recent publications have looked at this issue and concluded that liquid interaction can lead to structural changes of the vibrating elements even at room temperature [115]. The results obtained here seem to support this notion that the vibrating membranes are being changed during test especially at elevated temperatures. Some devices seem more susceptible than others although no clear trend has been established. Further analysis of this subject has been carried out in the next Chapter in which long term measurements were performed. The results seem to agree with the literature and indicate a frequency variation over time. This variation has been explained as structural change or liquid/surface interactions on the membrane.

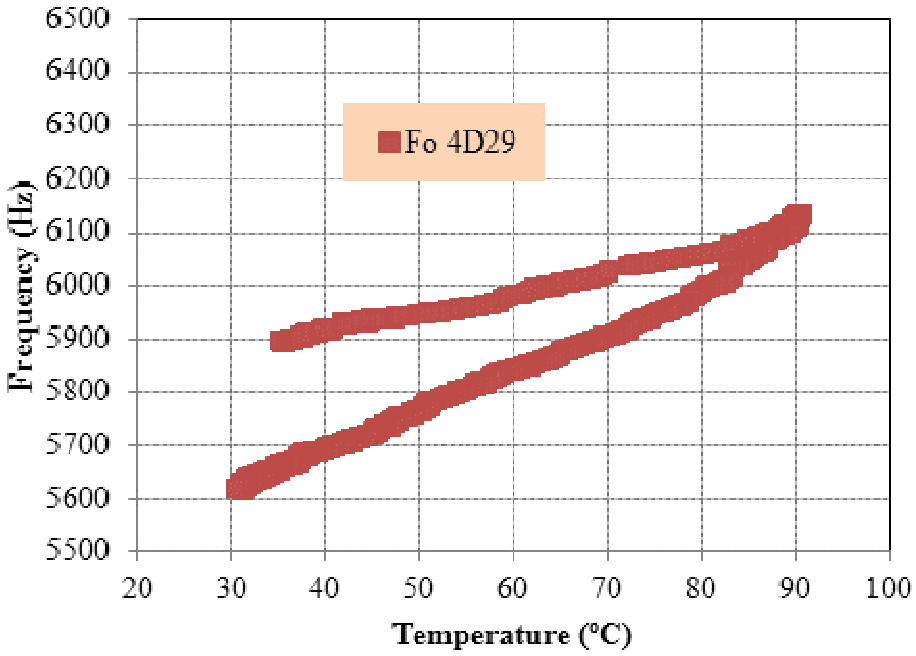

Figure 87. 4D29 hystheresis.

9.4 Multi-oil testing and correlation.

To assess the sensitivity range and repeatability of the sensors, the devices showing the best restuls were tested with two or more motor oils of different formulation. Plotting the behavior of the membrane over the different viscosity ranges should results in a single continous line with some overlap in the regions where the oil viscosity overlaps. How well this overlap takes place will give us an indication of the repeatability and accuracy of the sensors.

The analysis in this case is simpler. It is not necessary to remove the temperature effect as the sensor will be affected the same way in all oils. The sensors that show no differences between the oils will indicate that the sensor only responds to temperature.

The results of 4D10 are shown in Figure 88, Figure 89 and Figure 90. The data for the three different oils tested are displayed as different colors. Their overlap indicates the

repeatability of the measurement as the sensors were tested sequentialy and the temperature of the oils increased to change their viscosity. A power law fit has been applied to the resulting data. The fit-equation and the Rsquare are shown for frequency, quality factor and Vrms amplitude in each plot. The fit for frequency seems to be best around the middle of the range, deviating at higher viscosities and showing some error for the rapid increase that is seen at the lower viscosity values. The best fit is found to be for the Vrms amplitude measurement.

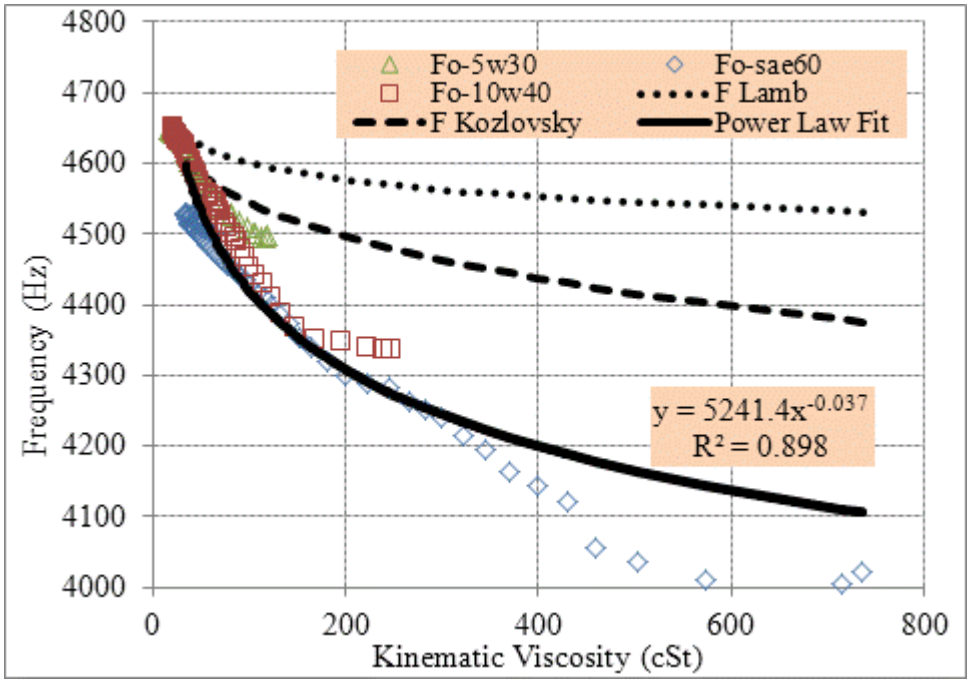

Figure 88. Frequency response of sensor 4D10 in three different heated oils with a power fit and compared to Lamb's and Kozlovsky's predictions.

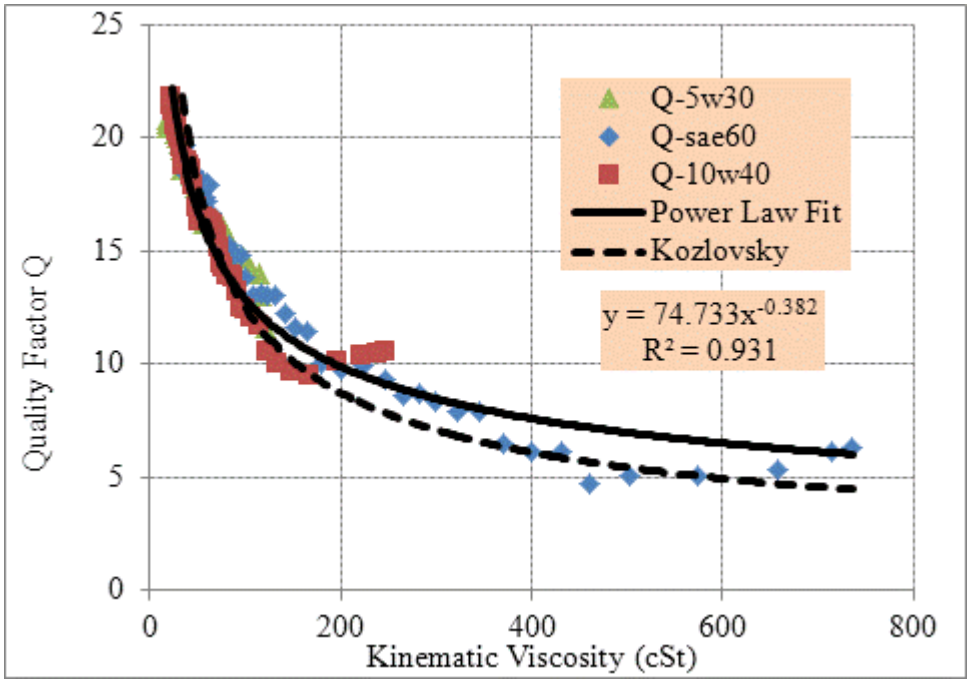

Figure 89. Q response of sensor 4D10 in three different heated oils with a power fit and compared to Kozlovsky's prediction.

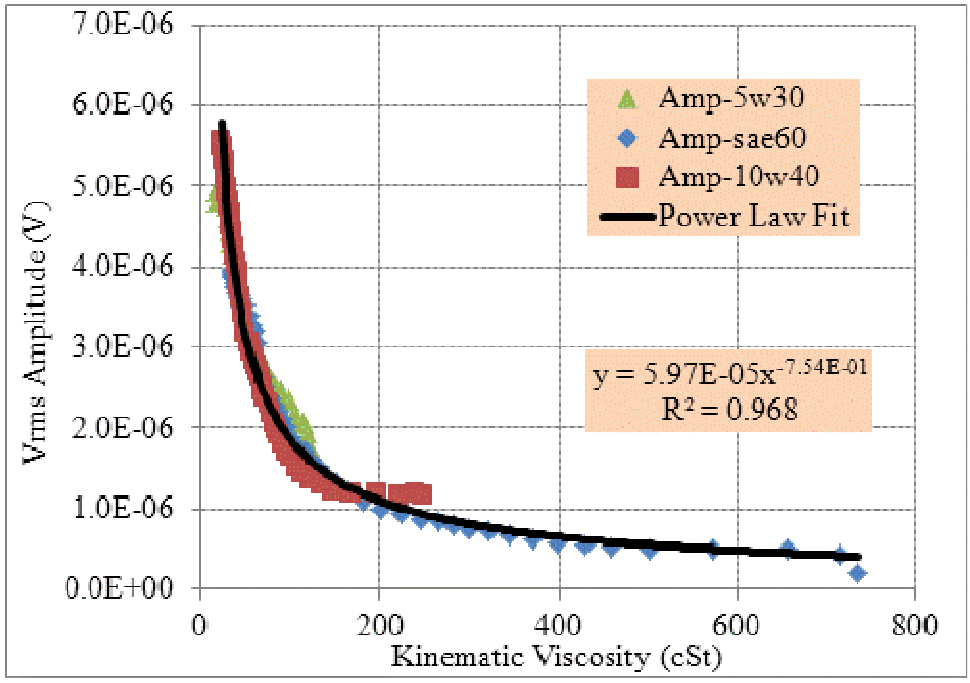

Figure 90. Amplitude Vrms response of sensor 4D10 in threee different oils.

Analyzing the error observed between the value predicted by the fit equation and the actual experimental values will indicate the measurement error of each of the three

methods used to determine viscosity. The frequency method seems to provide the better fit with a maximum of 4% error at the highest viscosity values as seen in Figure 91.

Using the quality factor to predict viscosity would result in an error of over 20% at the higher viscosity values as indicated in Figure 92. On the other hand, for viscosities lower than 200 cSt, the error is reduced below 20%. Similar variation results are shown in Figure 93, where the Vrms value of the FFT amplitude is used to predict the kinematic viscosity of a liquid with this particular device: 4D10.

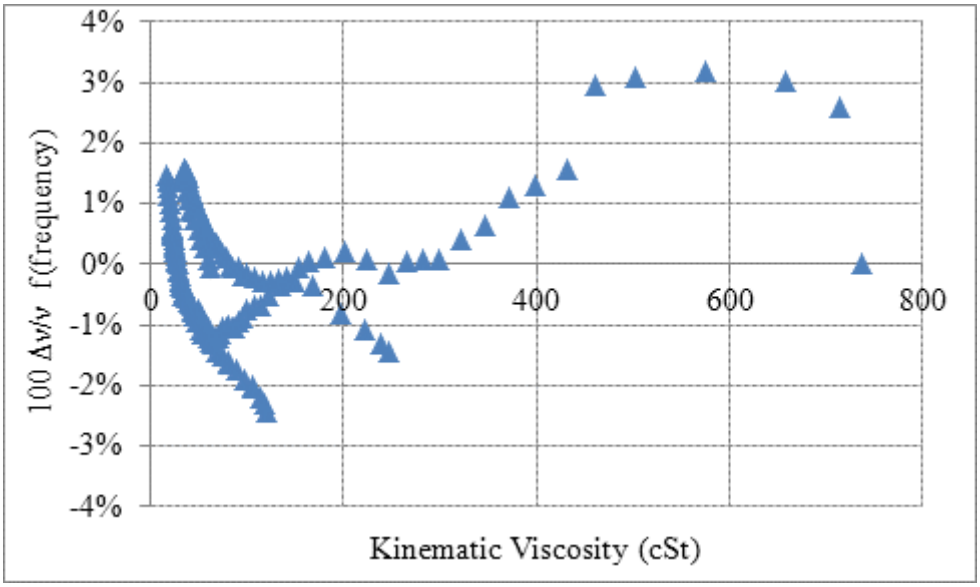

Figure 91. Error estimate to experimental fit based on the frequency variation of device 4D10.

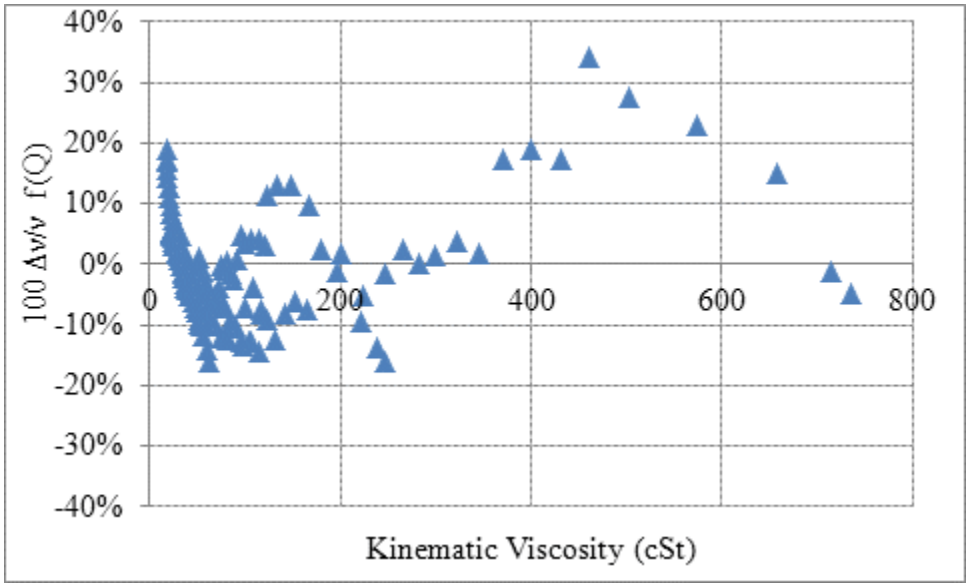

Figure 92. Error estimate to experimental fit on the quality factor variation of device 4D10.

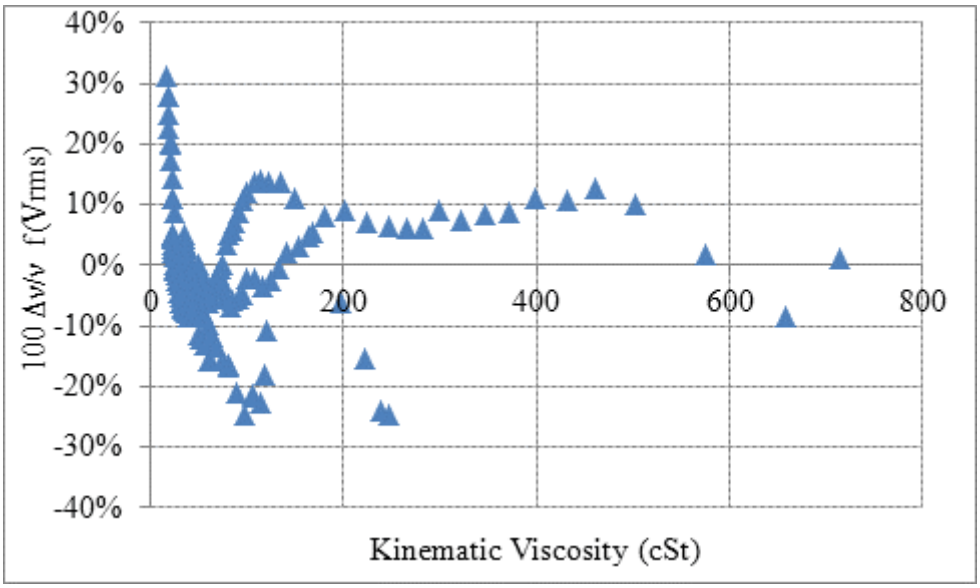

Figure 93. Error estimate to experimental fit on the amlitude Vrms variation of device 4D10.

Chapter 11.

LONG TERM TESTING

This Chapter focuses on the vibration behavior of the sensors with respect to long-term testing. The results presented in the previous Chapters were obtained during tests that varied from just a few minutes for the measurements at room temperature to a maximum of 2 hours for those that required temperature cycling. Effects such as frequency drifting and stability are studied in some selected samples for different viscosities. The following sensors were actuated in excess of 1 million times. The membranes were actually vibrated 10^7 times, as both sensors tested showed quality factors around 10. These measurements were taken at room temperature to avoid premature failure.

Devices D11 and 4D27 were used during this study. Next Chapter presents results of scaled down devices which were also tested in this manner for comparison. D11 is a 2.5mm membrane with a p+-diffused heater, which is 16% of the membrane area, an additional layer of passivation and a metal plate. 4D27 is a 2.5mm membrane with a polysilicon heater, which is 2% of the membrane area, an additional layer of passivation and a metal plate.

Figure 94, Figure 95 and Figure 96 show the frequency, Vrms amplitude and quality factor of device 4D27 vibrating in 5W30 oil at room temperature – which has a viscosity of 133 cSt. The frequency displays a linear drift, increasing by about 6.25 % over the first 8 hours, and then leveling off and remaining fairly consistent with a variation of +/- 1.2

%. The Vrms amplitude response follows a similar response, decreasing for the first 8 hours by about 37% of its original value and then leveling off. The measurement repeatability error remains constant at about +/- 10%. The quality factor shows the same behavior and the same amount of variation. The change in magnitude of the factors that characterized the vibration behavior has been observed by other researches in cantilever beams PZT-actuated in liquids for over 10^9 cycles [115]. This variation is explained by either surface absorption or liquid corrosion leading to either an increase on effective mass or structural damage. The large variation that is observed during our test is typical of our structures for this device and level of viscosity.

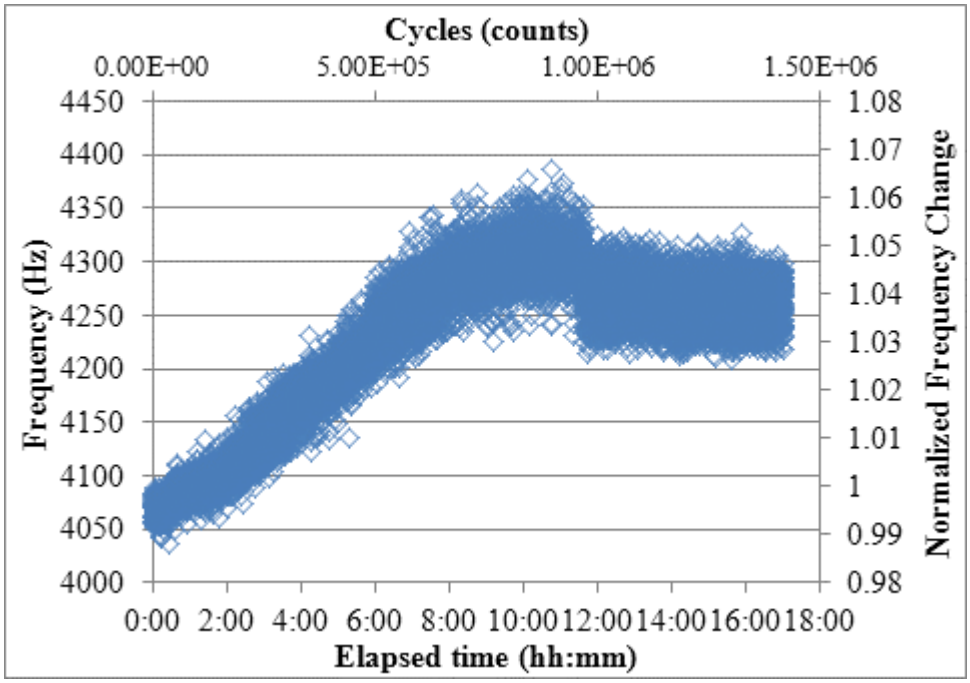

Figure 94. Frequency drift of 4D27 tested in 5W30 for 17 hours.

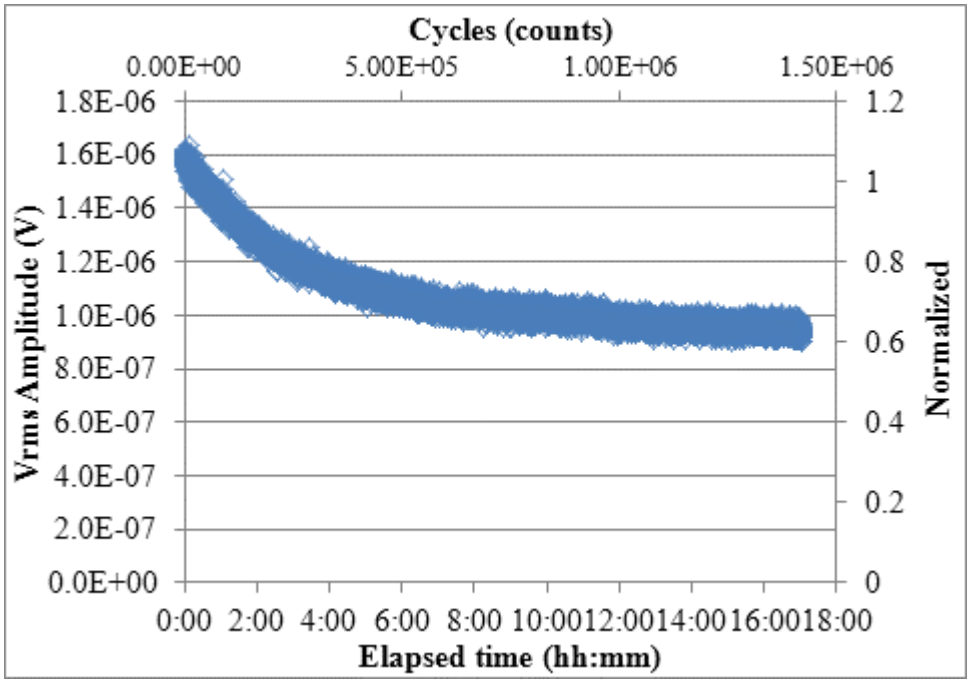

Figure 95. Vrms drift of 4D27 tested in 5W30 for 17 hours.

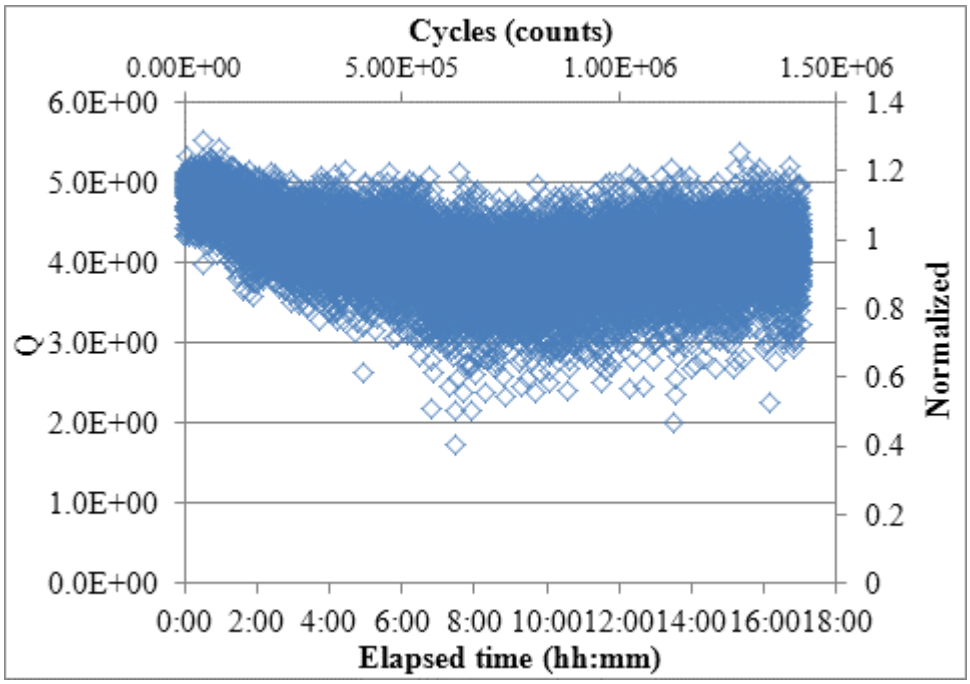

Figure 96. Q drift of 4D27 tested in 5W30 for 17 hours.

Device D11 was also tested in a similar manner in N350 oil, with a room temperature viscosity of 824 cSt. The results, presented in Figure 97, Figure 98 and Figure 99, show both less drift and lower measurement variation. The frequency seems to gradually increase but by less than 1%. The measurement error is much lower than before, +/- 0.5%.

For sensor D11, both Vrms amplitude and quality factor also show less variation and error than 4D27. There is no appreciable change in magnitude and the measurement variation is less than +/ 5%.

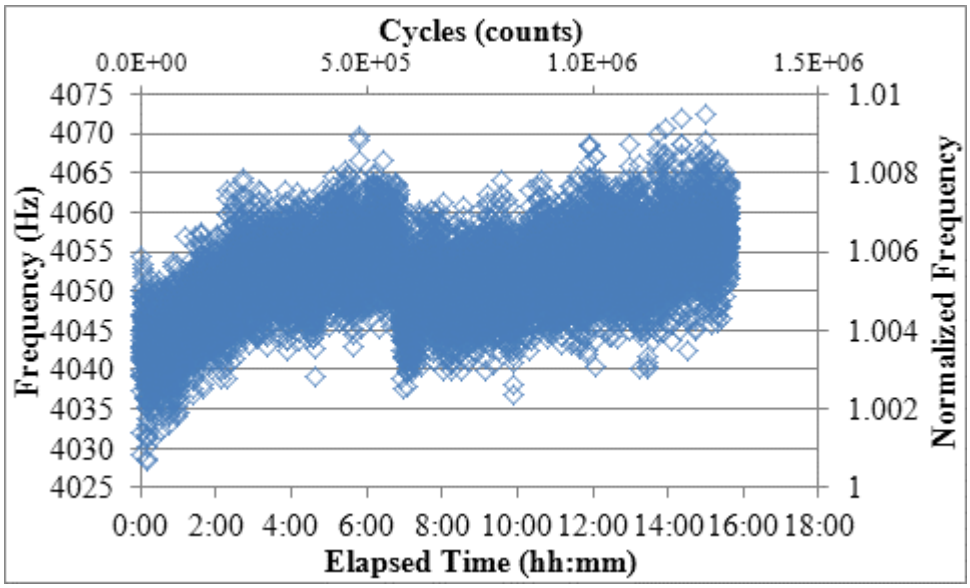

Figure 97. Frequency vibration drift of D11 tested in N350 for 15 hours.

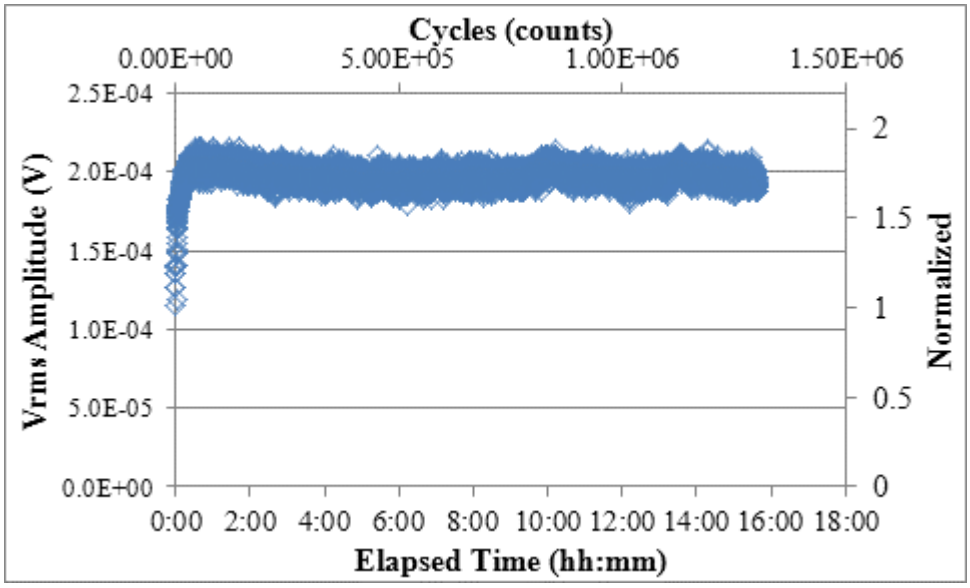

Figure 98. Vrms drift of D11 tested in N350 for 15 hours.

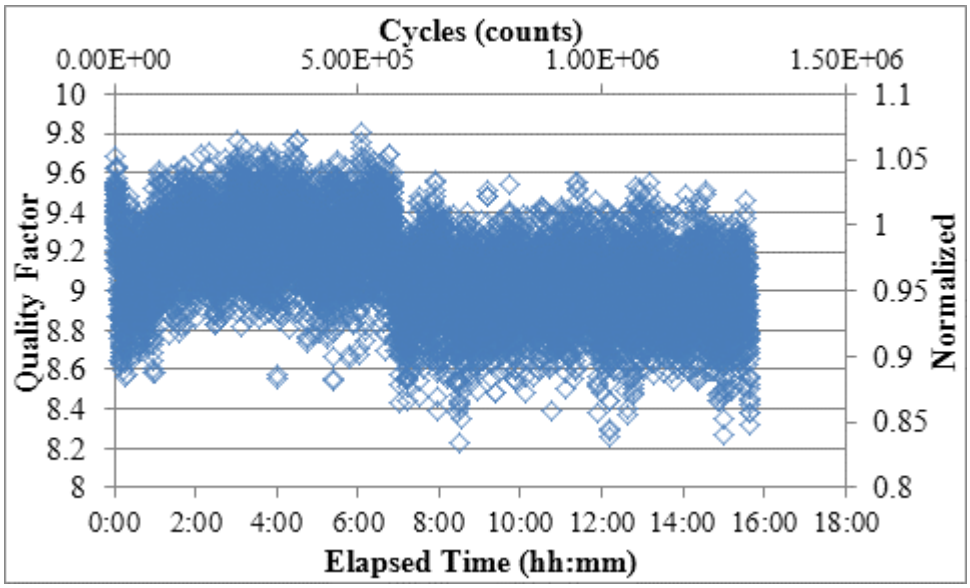

Figure 99. Q drift of D11 tested in N350 for 15 hours.

The results presented in this Chapter show about 1 order of magnitude better performance for a device with a p+-diffused heater when compared to a similar device with a polysilicon heater. The polysilicon heater is isolated both from the bulk of the membrane and the liquid being tested. On the other hand, the device with the p+-diffused

heater is buried directly into the silicon membrane. Repeatedly actuating the polysilicon heater leads to structural changes of the heater itself. As the polysilicon heater is heated and cooled over many cycles, the LPCVD-deposited film undergoes quick expansion and relaxation cycles which lead to a structural change which is observed in its free vibration behavior.

On the other hand, the heater which is buried in the silicon membrane directly seems to be less susceptive to significant structural change of the main silicon membrane. Surface absorption, as suggested by [115], could explain the drift that is commonly experienced by both devices since both have similar membrane compositions on top of the heater.

The measurement variation is much better for the device with the p+-diffused heater. This again could be due to the structural changes that the polysilicon heater undergoes during the heating cycles.

Chapter 12.

SCALING

This final Chapter studies the response characteristics as the size of the sensor is scaled down. The previous results were all taken on sensors with a square membrane length of 2.5 mm and a thickness of 15 micrometer. The results reported in this Chapter compare the vibration behavior in air of devices with a membrane length of 1.75 mm and 1 mm and membrane thickness of 10 μm and 7 μm respectively. Measurements were taken at room temperature. The advantages and disadvantage of scaling is also discussed. Long term tests were also performed for over 10^7 cycles.

11.1 Vibration in air – scaled devices

Based on the result from the previous section and keeping the ***a/h*** ratio consistent at 166, we studied the reduction of both the thickness and the length of the diaphragm in order to obtain a much-compacted device that will suffer from less uniformity issues.

For the vibration analysis of the devices with membranes with a length of 2.5 mm, we simplified the structure and only accounted for the 15 μm of silicon. We used the following equation to estimate the frequency of the first mode of vibration.

$$f = \frac{19.74}{2\pi a^2}\left[\frac{Eh^3}{12\rho h\left(1-\nu^2\right)}\right]^{1/2} \qquad (66)$$

This simple equation assumes a membrane of uniform material and it does not accurately represent the complex structures with multiple materials that compose our sensors. It is important to consider that the original silicon thickness, which is specified

by the silicon on insulator wafers, starts up at 15, 10 or 7 μm. Even though these thicknesses are used as the nominal membrane thickness, the actual membrane thicknesses are much different. First, the starting thickness of this silicon is reduced through oxidation: a total of 1.7 μm of SiO2 is grown through high temperature oxidation, leading to a silicon consumption of 0.75 μm. A 1-μm- dielectric layer of oxide is also deposited on the membrane. Another 1-μm-thick aluminum layer is used as the interconnection material. The 1-μm buried oxide is also left partially-etched under the silicon. Some devices will also include: polysilicon heaters, 0.5 μm thick, aluminum plates to enhance actuation, 1 μm thick and an additional passivation layer of 1 μm. For the thickest starting silicon membranes of 15 μm, the addition of these layers is less significant and (66) still provides a good estimate of the vibration frequency. On the other hand, for the thinner starting silicon membranes of 10 μm and 7 μm, the addition of all these layers leads away from the single-material equation.

This equation can still be used to understand the behavior and obtain a rough estimate of the order of magnitude of the expected natural frequency. Keeping this in mind and examining this equation we conclude that the frequency of oscillation will increase as both the membrane thickness is increased and the membrane size is decreased.

This is what is observed in Figure 100 where the vibration frequency increases from around 25,000 Hz to 75,000 Hz and 135,000 Hz as the membrane length and thickness is decreased from ($\boldsymbol{a}$ = 2.5 mm, 15 μm) to ($\boldsymbol{a}$ = 1.75 mm, h = 10 μm) and ($\boldsymbol{a}$ = 1 mm, h = 7 μm). Interestingly enough, the quality factor seems to be unaffected by the thickness of this starting substrate. Quality factor seems to remain at around 30 for most of the devices tested.

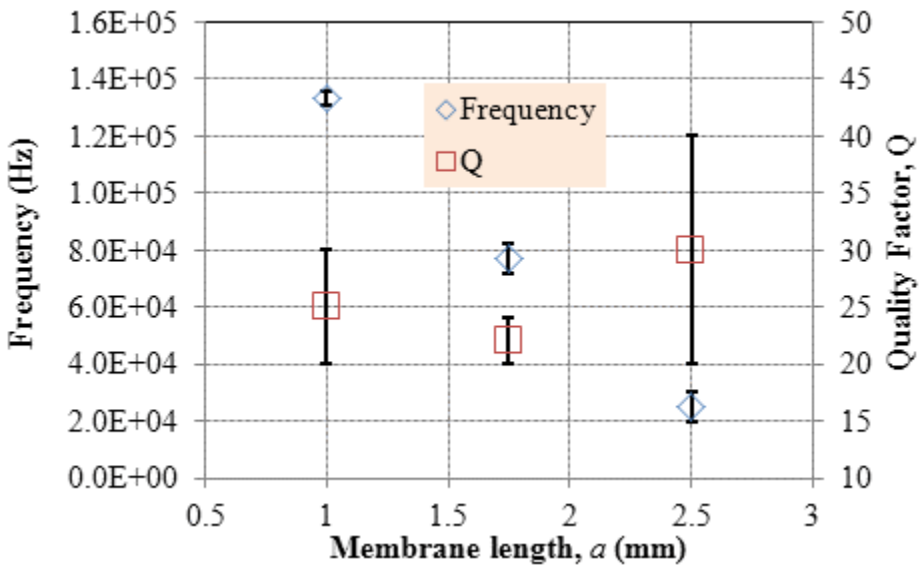

Figure 100. Free vibration characteristics versus membrane length. With silicon membrane thicknesses of 15 µm for a = 2.5 mm, 10 µm for a = 1.75 mm and 7 µm for a = 1 mm.

As their natural frequency of oscillation increased the excitation period needed to be reduced. Whereas for a 2.5 mm a 30 microsecond pulse of 15 V would set the membrane to vibrate, for a 1.75 mm membrane this pulse period was reduced to 10 µs and for a 1 mm membrane to 5 µs.

11.2 Viscosity at room temperature – scaled devices

Two sensors were tested at room temperature with varying viscosity oils with the same methodology as described in Chapter 9. Table 28 describes the characteristics of these two sensors. It is important to notice the larger vibration frequency observed when compared to the 2.5 mm devices analyzed in the previous chapters.

Table 28 SCALED DOWN DEVICE TESTED WITH VARYING VISCOSITY AT ROOM TEMPERATURE.

ID	Size	Heater	Heater Size	Passivation	Metal	F-air(Hz)	Q-air	F-oil (4cSt)
5D2	1.75	Poly	16%	Yes_P	No_M	80,630	20	13,000
6D3	1	Poly	16%	Yes_P	No_M	131,558	25	24,195

When tested in oil their frequency of vibration drops according to Lamb's model in relation to the density of the liquid and the size of membrane as in Equations 66 and 67:

$$\omega_{fluid} = \frac{\omega_{vacuum}}{\sqrt{1+\beta}} \tag{67}$$

where β

$$\beta = 0.669 \frac{\rho_{fluid} a}{\rho_{plate} h} \tag{68}$$

As such, the membranes will be vibrating at around 13,000 Hz and 24,000 Hz respectively while immersed in oil. This frequency will decrease as the viscosity is increased as predicted by Kozlovsky and shown in Figure 101. Sensor 5D2 shows a typical correlation to viscosity, its response being more significant than that predicted by Kozlovsky. On the other hand, device 6D3 does not follow this trend. This was also seen on some of the devices previously tested and could be due to sensor damage or fabrication defects. No clear correlations to size or membrane composition can be made based on this data. As explained before, many factors seem to affect frequency and care must be taken to ensure consistency during fabrication and testing.

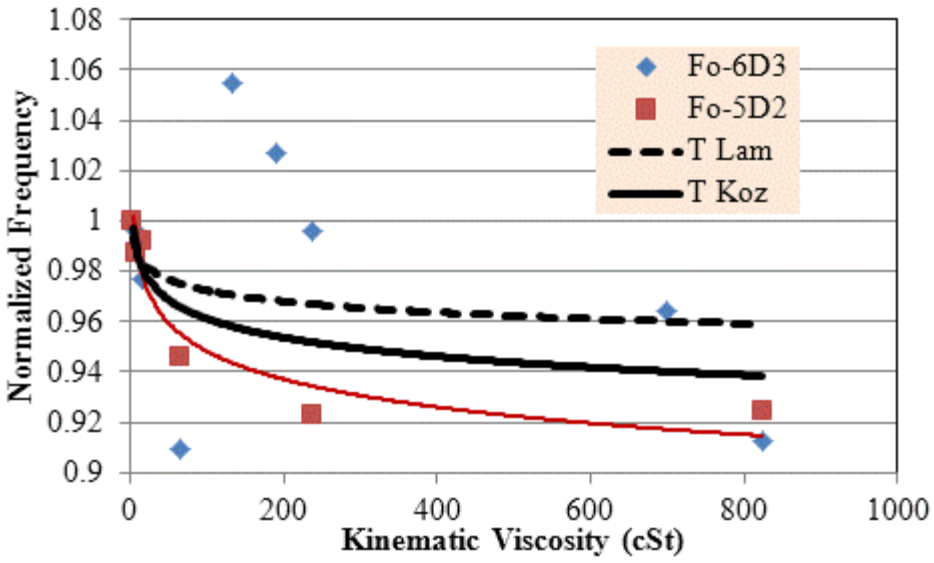

Figure 101. Frequeny decrease with increaing viscosity at room temperature for devices with (***a***=1.75 mm, h = 10 um – 5D2) and (***a*** = 1mm, h=7 um – 6D3).

Similar conclusions can be taken from Figure 102 where Q does not seem to correlate to viscosity for device 6D3, but it does for device 5D2. On the other hand, as shown in Figure 103, the Vrms amplitude of the oscillation indicates a good correlation of both sensors with the predicted model by Kozlovsky's. As described before, this method for determining viscosity leads to a larger error as the values for Q change more significantly than those for frequency.

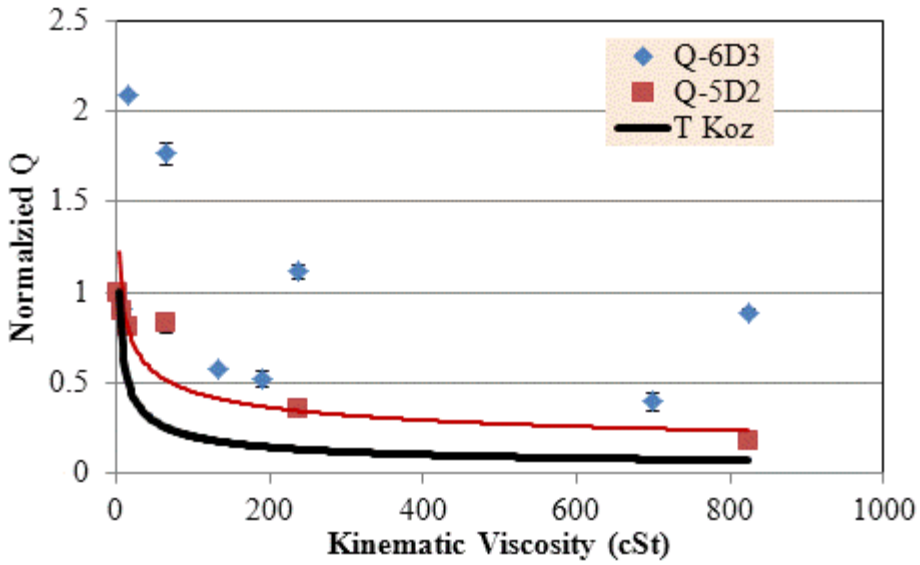

Figure 102. Frequeny decrease with increaing viscosity at room temperature for devices with (***a***=1.75 mm, h = 10 um – 5D2) and (***a*** = 1mm, h=7 um – 6D3).

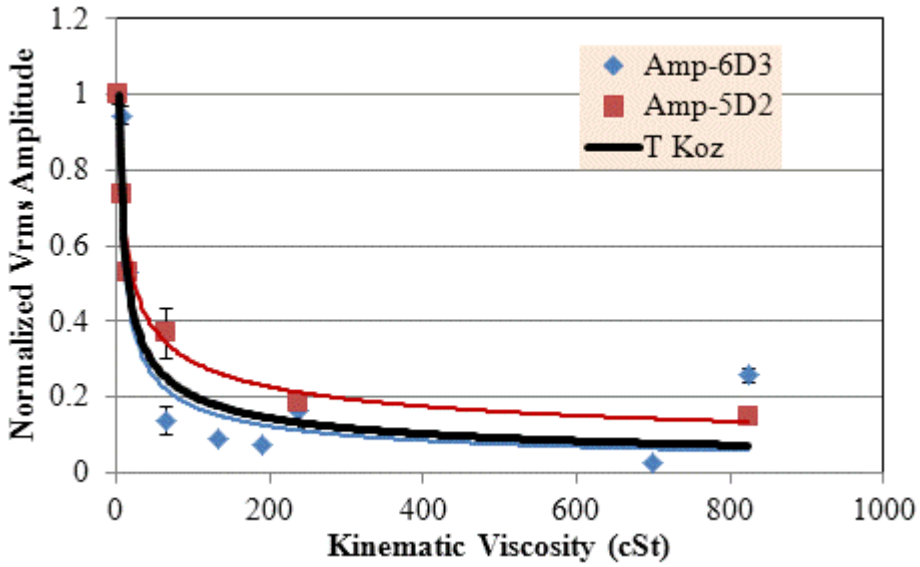

Figure 103. Frequeny decrease with increaing viscosity at room temperature for devices with (***a***=1.75 mm, h = 10 um – 5D2) and (***a*** = 1mm, h=7 um – 6D3).

The results presented here are encouraging and seem to arrive to the same conclusions as those drawn in Chapter 9. No clear correlation can be seen with respect to membrane composition or size but it seems that size scaling should not affect the

performance of these devices. As such, a smaller device is preferred as it reduces the real state and allows for more sensors to be fabricated. Having said this, it is important to provide a more consistent fabrication and testing methodology so that frequency can be used as the viscosity indicator as it provides a response with less variation.

11.3 Long term testing – scaled devices

Finally, 6D3 was long-term tested in 5W30 motor oil (133 cSt) overnight for a total of 12 hours. During the 10^6 cycles of thermal actuation, the membrane vibrated a total of 5 million times. The natural frequency of vibration in oil for sensor 6D3 remained at about 25,900 Hz and only varied by +/- 1% (+/- 250 Hz) over the 12 hours of testing as shown in Figure 104. The measurement variation was kept under 0.5% (+/- 50 Hz). This frequency drift and measurement repeatability values are similar to the one observed in larger sensors. In this particular case, the fact that polysilicon is used as the heater, does not seem to result in the large drift and measurement repeatability variation that was observed previously. As such, it remains unclear whether that could be the culprit to the large variation observed on an earlier device (4D27).

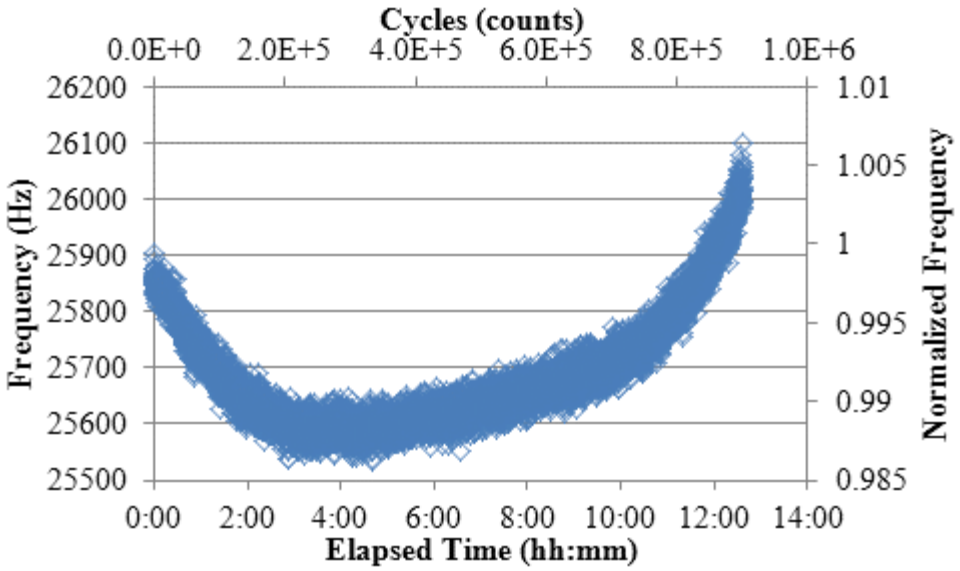

Figure 104. Frequency drift and repeatability measurements for device 6D3 in 5W30 oil.

The quality factor and amplitude Vrms show again larger variations than the frequency measurement, varying by approximately +/- 10% and +/- 5% respectively. This can be seen in Figure 105 and Figure 106. This is again similar to the results obtained with the 2.5 mm sensor D11 and presented in Chapter 11.

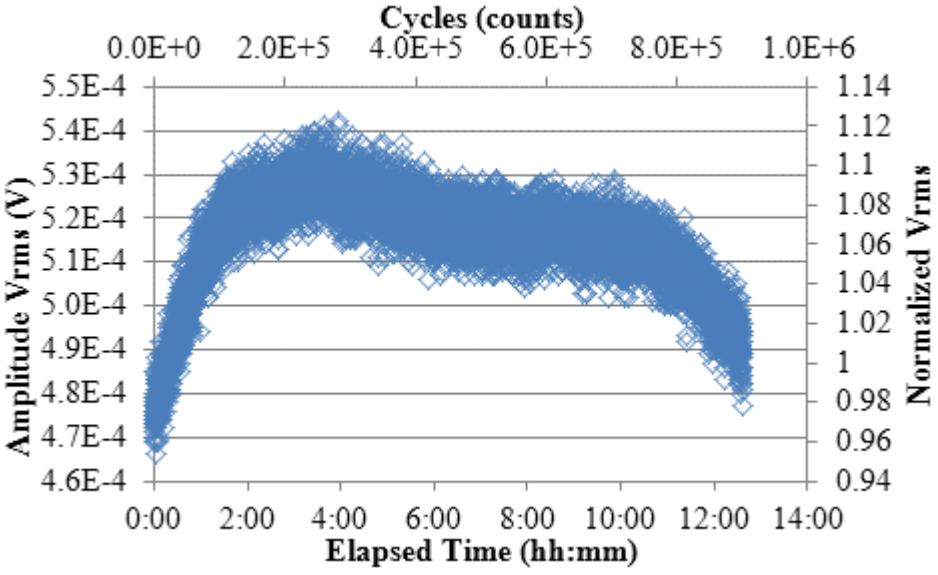

Figure 105. Vrms Amplitude drift and repeatability measurements for device 6D3 in 5W30 oil.

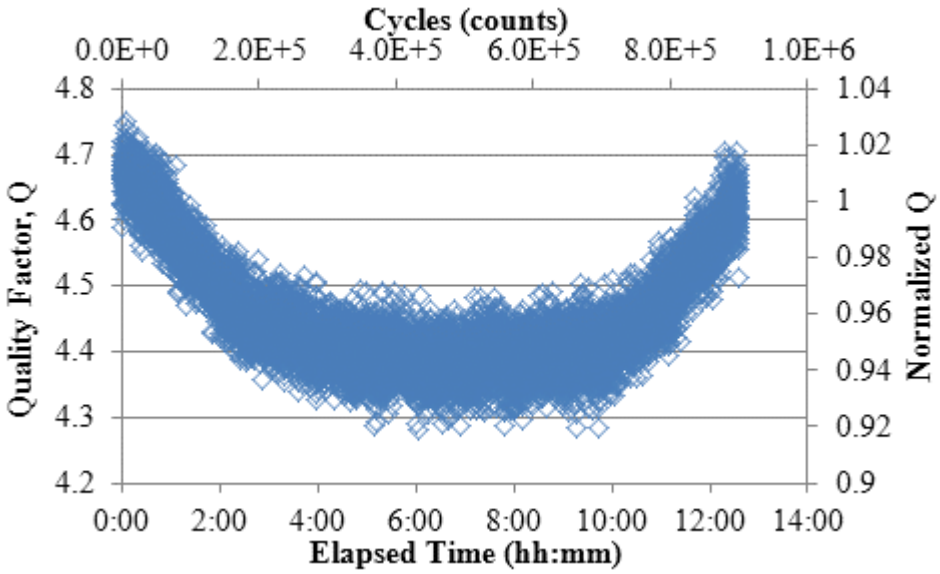

Figure 106. Quality factor drift and repeatability measurements for device 6D3 in 5W30 oil.

As concluded in the previous sections the frequency measurement is preferred since it leads to lower measurement error when the test conditions can be kept constant throughout the measurements. If the sensor is manipulated in any way or not position in the same exact condition as before, it will be difficult to correlate the frequency changes to viscosity changes. The quality factor or the Vrms measurements are much more forgiven when the sensor has to be placed in different vessels with different holding mechanism or sensor positioning, but it will result in larger errors.

Chapter 13.

CONCLUSION

This dissertation work is a multidisciplinary study combining different engineering disciplines. Mechanical engineering principles were used to describe the thermal vibration of a silicon plate as well as its interaction with the fluid. Microelectronic engineering principles were used to accurately fabricate and characterize the actuator and sensor structures. Finally, electrical engineering principles were employed to actuate, monitor and manipulate the electrical signal of the sensor based on rheology principles.

The actuation of this device was accomplished with the use of rapid heating applied to one of the faces of a silicon plate or membrane. This thermal impact set the membrane to vibrate at its natural frequency due to the inertial effects. The theory of operation of these kinds of structures, which originally developed for the aerospace industry back in the late 1960's for the design of high-speed aircraft and projectiles, was analyzed and confirmed both through simulation and experimental data. The temperature of the thermal impact was determined to affect the amplitude of the vibration but actually has little impact on the vibration frequency.

The proposed device includes both an in-situ actuator and sensing element, which makes it advantageous to other types of MEMS viscosity sensors. The proposed device is based on a thin silicon membrane but includes other layers to accomplish actuation and sensing. The in-situ actuation is accomplished through either a diffused silicon layer or a

polysilicon layer. The sensing elements are based on either diffused or polysilicon piezoresistive gauges.

A designed experiment was carried out to study the vibration behavior of these complex MEMS membranes. The size of the heaters and the material composition of the heater and membrane were varied in order to assess their effects on frequency of vibration, amplitude and quality factor. It was concluded that the membranes with a polysilicon heater have a lower vibration frequency when compared to those with the p+-diffused heater. The presence of metal and passivation also increases this frequency of vibration. Quality factor is highest for the devices with p+-diffused heaters that included passivation and metal layers. The more complex membranes, which include polysilicon heaters, show lower Q values.

This frequency of vibration of the membrane was proven to change not only due to the density of the fluid, according to the classical theory, but also to be proportional to the viscosity of the fluid, according to Kozlovsky's model, which is adjusted for microelectromechanical membrane structures. This change in frequency is a more accurate indication of viscosity than the classical quality factor measurement. Room temperature measurements with liquids of varying viscosity were performed. Care must be taken to make this frequency measurement as accurate as possible and avoid any uncontrolled factor that could affect the free vibration frequency.

The effect of temperature on the vibration characteristics of this type of membranes was performed. The membranes with a larger amount of silicon show an expected decrease in vibration frequency with increasing temperature due to the negative temperature coefficient of the Young’s modulus of silicon. Membranes with additional

SiO_2 passivation show an increase in vibration frequency with increasing temperature. This indicates compensation on the vibration frequency due to the positive temperature coefficient of the Young's modulus of SiO_2. Some devices show a quadratic dependence to temperature which indicates more complex interactions between the membrane materials. The quality factor of the vibration increased with temperature for those devices which also showed increasing mechanical vibration frequency with temperature, while it decreased for the devices which were dominated by the negative temperature coefficient of the Young's modulus of silicon. Device packaging increased the temperature effect on vibration frequency but decreased the quality factor dependence also due to the increase on the vibration frequency with temperature on devices with additional SiO_2.

Temperature dependent viscosity measurements were performed on several devices with heated oil. The results indicate a good correlation of viscosity to both frequency and quality factor when the devices are not damaged due to temperature cycling. Evidence of device damage is seen by the large hysteresis effects of the most inconsistent devices. This damage could be due to mechanical cycling, heat effects or both. Long term testing at room temperature indicated significant frequency and quality factor drift for large devices with polysilicon heaters at room temperature, which could be an indication of mechanical damage. Thus, it is reasonable to assume that at elevated temperatures this effect would be more significant.

Frequency correlation to viscosity was shown to be the best indicator for the range of viscosities tested (+/- 5%), with lower error and lower variation than that of quality factor (+/- 20%). On the other hand and even though quality factor showed larger errors overall,

it was more reliable to device damage and when test conditions and set up were less controlled.

These results scaled with membrane size. Devices with equal aspect ratio but reduced membrane size (1 mm x 1 mm) were tested to show similar results and behaviors to those with larger size (2.5 mm x 2.5 mm). No significant difference in actuation power, vibration behavior or sensitivity to viscosity was observed. On the other hand, better long term stability was observed. The main difference was found to be in the frequency of vibration, this being much larger for the smaller devices. Concerns arise when the frequency of vibration is too large as the device may not be able to predict viscosity degradation of multi-grade oils accurately (macro vs. micro effects). These effects were not evaluated.

In conclusion, the proposed thermally actuated MEMS viscosity sensor presents a cheap and reliable viscosity sensor which can be utilized in the field and in reduced spaces. Further system integration can easily be carried out to obtain real time measurements of viscosity in many critical industrial and automotive applications. Biological application can also be explored if a reliable isolation of the electrically active components of the membrane is further developed.

REFERENCES

[1] M.M.D. Lara and C. Atkinson, "Theoretical model on the interaction of a vibrating beam and the surrounding viscous fluid with applications to density and viscosity sensors," *Proceedings of IEEE Sensors, 2004.*, 2004, pp. 828-831.

[2] N. Belmiloud, I. Dufour, L. Nicu, A. Colin, and J. Pistre, "Vibrating Microcantilever used as a viscometer and microrheometer," *IEEE Sensors 2006, EXCO*, EXCO, eds., Daegu, Korea: IEEE, 2006, pp. 753-756.

[3] C. Harrison, A. Fornari, C. Hua, S. Ryu, A.R.H. Goodwin, K. Hsu, F. Marty, and B. Mercier, "A microfluidic MEMS sensor for the measurement of density and viscosity at high pressure," *Proceedings of SPIE*, vol. 6465, 2007, pp. 64650U-1-13.

[4] A. Ramkumar, X. Chen, and A. Lal, "Silicon Ultrasonic Horn Driven Microprobe Viscometer," *2006 IEEE Ultrasonics Symposium*, Oct. 2006, pp. 1449-1452.

[5] C. Ayela and L. Nicu, "Micromachined piezoelectric membranes with high nominal quality factors in Newtonian liquid media: a Lamb's model validation at the microscale," *Sensors and Actuators B*, vol. 123, 2007, pp. 860-868.

[6] I. Goubaidoulline, J. Reuber, F. Merz, and D. Johannsmann, "Simultaneous determination of density and viscosity of liquids based on quartz-crystal resonators covered with nanoporous alumina," *Journal of Applied Physics*, vol. 98, 2005, pp. 0143051-0143054.

[7] B.A. Martin, "Viscosity and density sensing with ultrasonic plate waves," *Sensors and Actuators A: Physical*, vol. 22, 1990, pp. 704-708.

[8] H.A. Barnes, J.F. Hutton, and K. Walters, *An Introduction to Rheology*, Amsterdam: Elsevier Science Pulbisher B. V., 1989.

[9] S.S. Wang, "Road tests of oil condition sensor and sensing technique," *Sens. Actuators B*, vol. 73, 2001, pp. 106-111.

[10] Mobil, "Mobil 1 5W-30," *http://www.mobil.com/USA-English/Lubes/PDS/GLXXENPVLMOMobil1_5W-30.aspx*, pp. 1-2.

[11] D.S. Viswanath, T.K. Ghosh, D.H.L. Prasad, N.V.K. Dutt, and K.Y. Rani, "Chapter 2 VISCOMETERS," *Viscosity of Liquids*, Springer Netherlands, 2007, pp. 9-107.

[12] K.K. Kanazawa and J.G. Gordon II, “Frequency of a quartz microbalance in contact with liquid,” *Analytical Chemistry*, vol. 57, Jul. 1985, pp. 1770-1771.

[13] B. Jakoby, M. Scherer, M. Buskies, and H. Eisenschmid, “An automotive engine oil viscosity sensor,” *IEEE Sensors Journal*, vol. 3, Oct. 2003, pp. 562-568.

[14] H. Muramatsu, E. Tamiya, and I. Karube, “Computation of equivalent circuit parameters of quartz crystals in contact with liquids and study of liquid properties,” *Analytical Chemistry*, vol. 60, Oct. 1988, pp. 2142-2146.

[15] L.F. Matsiev, “Application of flexural mechanical resonators to high throughput liquid characterization,” *2000 IEEE Ultrasonics Symposium. Proceedings. An International Symposium (Cat. No.00CH37121)*, 2000, pp. 427-434.

[16] F. Herrmann, D. Hahn, and S. Buttgenback, “Separate determination of liquid density and viscosity with sagittally corrugated Love-mode sensors,” *Sensors and Actuators A: Physical*, vol. 78, Dec. 1999, pp. 99-107.

[17] S.J. Martin, R.W. Cernosek, and L. Casaus, “Measuring liquid properties with smooth- and textured-surface resonators,” *1993 ieee international frequency control symposium*, 1993, pp. 603-8.

[18] K. Durdag, “Solid state acoustic wave sensors for real-time in-line measurement of oil viscosity,” *Sensor Review*, vol. 28, 2008, pp. 68-73.

[19] J.D. Turner and L. Austin, “Electrical techniques for monitoring the condition of lubrication oil,” *Measurement Science and Technology*, vol. 14, Oct. 2003, pp. 1794-1800.

[20] A. Agoston, C. Otsch, and B. Akoby, “Viscosity sensors for engine oil condition monitoring—Application and interpretation of results,” *Sensors and Actuators A: Physical*, vol. 121, Jun. 2005, pp. 327-332.

[21] S.S. Wang, “Engine oil condition sensor: method for establishing correlation with total acid number,” *Sensors and Actuators B: Chemical*, vol. 86, Sep. 2002, pp. 122-126.

[22] Y. Jiménez, R. Fernández, R. Torres, and A. Arnau, “A Contribution To Solve the Problem of Crystal Microbalance Applications,” *IEEE transactions on ultrasonics, ferroelectrics, and frequency control*, vol. 53, 2006.

[23] M.J. van der Werff, Y.J. Yuan, E.R. Hirst, W.L. Xu, H. Chen, and J.E. Bronlund, “Quartz Crystal Microbalance Induced Bond Rupture Sensing for Medical Diagnostics,” *IEEE Sensors Journal*, vol. 7, May. 2007, pp. 762-769.

[24] P.I. Reyes, Z. Zhang, H. Chen, Z. Duan, J. Zhong, G. Saraf, Y. Lu, O. Taratula, E. Galoppini, and N.N. Boustany, "A ZnO Nanostructure-Based Quartz Crystal Microbalance Device for Biochemical Sensing," *IEEE Sensors Journal*, vol. 9, Oct. 2009, pp. 1302-1307.

[25] S.W. Wenzel, B.A. Martin, and R.M. White, "Generalized Lamb-wave multisensor," *IEEE 1988 Ultrasonics Symposium Proceedings.*, 1988, pp. 563-567.

[26] S. Wolf and R.N. Tauber, *Silicon Processing for the VLSI Era*, Sunset Beach, California: Lattice Press, 1986.

[27] D.E. Angelescu, H. Chen, J. Jundt, H. Berthet, B. Mercier, and F. Marty, "Highly integrated microfluidic sensors," *Proceedings of SPIE*, vol. 6886, 2008, pp. 688607-688607-9.

[28] P. Galambos and F. Forster, "An optical micro-fluidic viscometer," *Micro-Electro-Mechanical Systems (MEMS) - 1998. ASME International Mechanical Engineering Congress and Exposition*, vol. 66, 1998, pp. 187-191.

[29] M.T. Blom, E. Chmela, F.H.J.V.D. Heyden, R.E. Oosterbroek, R. Tijssen, M. Elwenspoek, and A.V.D. Berg, "A differential viscosity detector for use in miniaturized chemical separation systems," *Journal of Microelectromechanical Systems*, vol. 14, Feb. 2005, pp. 70-80.

[30] T. Tschan and N.D. Rooij, "Oil-damped piezoresistive silicon accelerometers," *TRANSDUCERS '91: 1991 International Conference on Solid-State Sensors and Actuators. Digest of Technical Papers*, 1991, pp. 112-114.

[31] M. Andrews and P. Harris, "Damping and gas viscosity measurements using a microstructure," *Sensors & Actuators: A. Physical*, vol. 49, 1995, pp. 103-108.

[32] J.E. Sader, "frequency response of cantilever bemas immersed in viscous fluids with applications to the atomic force microscope," *Journal of Applied Physics*, vol. 84, 1998, pp. 64-76.

[33] S. Weigert, M. Dreier, and M. Hegner, "Frequency shifts of cantilevers vibrating in various media," *Applied Physics Letters*, vol. 69, 1996, p. 2834.

[34] P.I. Oden, G.Y. Chen, R. a Steele, R.J. Warmack, and T. Thundat, "Viscous drag measurements utilizing microfabricated cantilevers," *Applied Physics Letters*, vol. 68, 1996, p. 3814.

[35] J.W.M. Chon, P. Mulvaney, and J.E. Sader, "Experimental validation of theoretical models for the frequency response of atomic force microscope

cantilever beams immersed in fluids," *Journal of Applied Physics*, vol. 87, 2001, pp. 3978-3988.

[36] W.Y. Shih, X. Li, H. Gu, W.-H. Shih, and I. a Aksay, "Simultaneous liquid viscosity and density determination with piezoelectric unimorph cantilevers," *Journal of Applied Physics*, vol. 89, 2001, p. 1497.

[37] T. Naik, E.K. Longmire, and S.C. Mantell, "Dynamic response of a cantilever in liquid near a solid wall," *Sensors and Actuators A*, vol. 102, 2003, pp. 240-245.

[38] G. Rezazadeh, M. Ghanbari, and I. Mirzaee, "Simultaneous Measurement of Fluids viscosity and density using a microbeam," *2009 Vth International Conference on Perspective Technologies and Methods in MEMS Design. MEMSTECH'2009*, 2009, pp. 36-44.

[39] X. Huang, S. Li, J. Schultz, Q. Wang, and Q. Lin, "Mems sensor for continuous monitoring of glucose in Subcutaneous Tissue," *IEEE 22nd International Conference on Micro Electro Mechanical Systems, 2009. MEMS 2009*, 2009, pp. 352-355.

[40] A. Agoston, F. Keplinger, and B. Jakoby, "Evaluation of a Vibrating Micromachined Cantilever Sensor for Measuring the Viscosity of Complex Organic Liquids," *Sensors and Actuators A*, vol. 123-124, 2005, pp. 82-86.

[41] E.K. Reichel, C. Riesch, F. Keplinger, B. Jakoby, I. Microelectronics, and J. Kepler, "Remote electromagnetic excitation of miniaturized in-plane plate resonators for sensing applications," *2008 IEEE International Frequency Control Symposium*, May. 2008, pp. 144-147.

[42] K. a Ronaldson, a D. Fitt, a R.H. Goodwin, and W. a Wakeham, "Transversely Oscillating MEMS Viscometer: The 'Spider'," *International Journal of Thermophysics*, vol. 27, 2006, pp. 1677-1695.

[43] A.R.H. Goodwin, A.D. Fitt, K.A. Ronaldson, and W.A. Wakeham, "A Vibrating Plate Fabricated by the Methods of Microelectromechanical Systems (MEMS) for the Simultaneous Measurement of Density and Viscosity: Results for Argon at Temperatures Between 323 and 423K at Pressures up to 68 MPa," *International Journal of Thermophysics*, vol. 27, Oct. 2006, pp. 1650-1676.

[44] A.R.H. Goodwin, E.P. Donzier, O. Vancauwenberghe, A.D. Fitt, K.A. Ronaldson, W.A. Wakeham, M.M.D. Lara, F. Marty, and B. Mercier, "A Vibrating Edge Supported Plate, Fabricated by the Methods of Micro Electro Mechanical System for the Simultaneous Measurement of Density and Viscosity: Results for Methylbenzene and Octane at Temperatures Between (323 and 423) K and Pressures in the Ran," *J. Chem. Eng. Data*, vol. 51, 2006, pp. 190-208.

[45] C. Harrison, S. Ryu, A.R.H. Goodwin, K. Hsu, E.P. Donzier, F. Marty, and B. Mercier, "A MEMS sensor for the measurement of density-viscosity for oilfield applications," *Proceedings of SPIE*, vol. 6111, 2006, p. 61110D-61110D-11.

[46] C. Harrison, E. Tavernier, O. Vancauwenberghe, E. Donzier, K. Hsu, A.R.H. Goodwin, F. Marty, and B. Mercier, "On the response of a resonating plate in a liquid near a solid wall," *Sensors and Actuators A: Physical*, vol. 134, Mar. 2007, pp. 414-426.

[47] W.A. Wakeham, M.A. Assael, J.K. Atkinson, J. Bilek, J.M.N.A. Fareleira, A.D. Fitt, A.R.H. Goodwin, and C.M.B.P. Oliveira, "Thermophysical Property Measurements: The Journey from Accuracy to Fitness for Purpose," *International Journal of Thermophysics*, vol. 28, Jun. 2007, pp. 372-416.

[48] W.A. Wakeham, A.D. Fitt, K.A. Ronaldson, and A.R.H. Goodwin, "A review of vibrating objects for the measurement of density and viscosity in oilfields including devices fabricated by the method of MEMS," *High temperatures-high pressures*, vol. 37, 2008, pp. 137-151.

[49] I. Etchart, H. Chen, P. Dryden, J. Jundt, C. Harrison, K. Hsu, F. Marty, and B. Mercier, "MEMS sensors for density–viscosity sensing in a low-flow microfluidic environment," *Sensors and Actuators A: Physical*, vol. 141, Feb. 2008, pp. 266-275.

[50] A.R.H. Goodwin, C.V. Jakeways, and M.M.D. Lara, "A MEMS Vibrating Edge Supported Plate for the Simultaneous Measurement of Density and Viscosity: Results for Nitrogen, Methylbenzene, Water, 1-Propene,1,1,2,3,3,3-hexafluoro-oxidized-polymd, and Polydimethylsiloxane and Four Certified Reference Materials," *Journal of Chemical and Engineering Data*, vol. 53, 2008, pp. 1436-1443.

[51] A.R.H. Goodwin, "A MEMS Vibrating Edge Supported Plate for the Simultaneous Measurement of Density and Viscosity: Results for Argon, Nitrogen, and Methane at Temperatures from (297 to 373) K and Pressures between (1 and 62) MPa †," *Journal of Chemical & Engineering Data*, vol. 54, Sep. 2008, pp. 536-541.

[52] A.D. Fitt, K.A. Ronaldson, and W.A. Wakeham, "A fractional differential equation for a MEMS viscometer used in the oil industry," *Journal of Computational and Applied Mathematics*, vol. 229, 2009, pp. 373-381.

[53] A.D. Fitt, A.R.H. Goodwin, K.A. Ronaldson, and W.A. Wakeham, "A fractional differential equation for a MEMS viscometer used in the oil industry," *Journal of Computational and Applied Mathematics*, vol. 229, Jul. 2009, pp. 373-381.

[54] O. Brand, J.M. English, S.A. Bidstrup, and M.G. Allen, "Micromachined viscosity sensor for real-time polymerization monitoring," *Proceedings of the 1997*

International Conference on Solid-State Sensors and Actuators, vol. 1, 1997, pp. 121-124.

[55] O. Brand, M. Hornung, D. Lange, and H. Baltes, "CMOS Resonant Microsensors," *SPIE conference on Micromachined Devices and Components*, SPIE, eds., Santa Clara: 1998, pp. 238-250.

[56] O. Brand, H. Baltes, and U. Baldenweg, "Thermally excited silicon oxide bridge resonators in CMOS technology," *Journal of Micromech. Microeng.*, vol. 2, 1992, pp. 208-210.

[57] M. Hornung, O. Brand, O. Paul, and H. Baltes, "Long-term stability of membrane transducers for proximity sensing," *Proceedings of SPIE on Micromachined Devices and Components*, Santa Clara: Spie vol 3514, 1998, pp. 251-259.

[58] O. Brand, M. Hornung, H. Baltes, and C. Hafner, "Ultrasound barrier microsystem for object detection based on micromachined transducer elements," *Journal of Microelectromechanical Systems*, vol. 6, Jun. 1997, pp. 151-160.

[59] K. Naeli and O. Brand, "An iterative curve fitting method for accurate calculation of quality factors in resonators.," *The Review of scientific instruments*, vol. 80, Apr. 2009, p. 045105.

[60] K. Naeli and O. Brand, "Dimensional considerations in achieving large quality factors for resonant silicon cantilevers in air," *Journal of Applied Physics*, vol. 105, 2009, pp. 014908-1-10.

[61] O. Brand, H. Baltes, and U. Baldenweg, "Thermally excited silicon oxide bean and bridge resonators in CMOS technology," *IEEE Transactions on Electron Devices*, vol. 40, 1993, pp. 1745-1753.

[62] O. Brand, H. Baltes, and U. Baldenweg, "Ultrasound-transducer using membrane resonators realized with bipolar IC technology," *IEEE Int. Workshop on Micro Electro Mechanical* , vol. 94pp, 1994, pp. 33-38.

[63] Y. Kozlovsky, "Vibration of plates in contact with viscous fluid: Extension of Lamb′s model," *Journal of Sound and Vibration*, vol. 326, Sep. 2009, pp. 332-339.

[64] J. Meyer and T. Giesler, "Micromachined acousto-gravimetric transducer with applications to biomedical sensing," *Proceedings of the Annual Conference on Engineering in Medicine and Biology*, vol. 15, 1993, pp. 987-988.

[65] P. Enoksson, G. Stemme, and E. Stemme, "Fluid density sensor based on resonance vibration," *Sensors & Actuators: A. Physical*, vol. 46-47, 1995, pp. 327-331.

[66] Y. Hirai, R. Mori, H. Kikuta, N. Kato, K. Inoute, and Y. Tanaka, "Resonance Characteristics of Micro Cantilever in Liquid," *Jpn. Journal of Applied Physics*, vol. 37, 1998, pp. 7064-7069.

[67] S. Boskovic, J. Chon, P. Mulvaney, and J.E. Sader, "Rheological measurements using microcantilevers," *Journal of Rheology*, vol. 46pp, 2002, pp. 891-899.

[68] Y.J. Zhao, A. Davidson, J. Bain, S.Q. Li, Q. Wang, and Q. Lin, "A MEMS viscometric glucose monitoring device," *Tranducers '05*, 2005, pp. 1816-1819.

[69] E.K. Reichel, B. Jakoby, and C. Riesch, "A Novel Combined Rheometer and Density Meter Suitable for Integration in Microfluidic Systems," *2007 IEEE Sensors*, 2007, pp. 908-911.

[70] N. Belmiloud, I. Dufour, A. Colin, and L. Nicu, "Rheological behavior probed by vibrating microcantilevers," *Applied Physics Letters*, vol. 92, 2008, pp. 041907-1-3.

[71] N. Belmiloud, I. Dufour, A. Colin, and L. Nicu, "Vibrating Microcantilevers : Tools for Microrheology," *AIP Conference Proceedings*, vol. 1027, 2008, pp. 1159-1161.

[72] A. Ebisui, Y. Taguchi, and Y. Nagasaka, "Novel optical viscosity sensor based on laser-induced capillary wave," *Proceedings of SPIE, MOEMS and Miniaturized Systems VII*, vol. 6887, 2008, p. 68870G-68870G-10.

[73] H. Zeng and Y. Zhao, "On-Chip Blood Viscometer Towards Point-of-Care Hematological Diagnosis," *2009 IEEE 22nd International Conference on Micro Electro Mechanical Systems*, Jan. 2009, pp. 240-243.

[74] D. Sparks, R. Smith, V. Cruz, N. Tran, A. Chimbayo, D. Riley, and N. Naja, "Dynamic and kinematic viscosity measurements with a resonating microtube," *Sensors and Actuators A: Physical*, vol. 149, Jan. 2009, pp. 38-41.

[75] J. Andle, R. Haskell, R. Sbardella, G. Morehead, M. Chap, J. Columbus, and D. Stevens, "Design, Optimization and Characterization of an Acoustic Plate Mode Viscometer," *2007 IEEE Sensors*, 2007, pp. 864-867.

[76] K.K. Kanazawa and J.G. Gordon II, "The oscillation frequency of a quartz resonator in contact with liquid," *Analytica Chimica Acta*, vol. 175, 1985, pp. 99-105.

[77] V.M. Mecea, J.O. Carlsson, and R.V. Bucur, "Extensions of the quartz-crystal-microbalane technique," *Sensors and Actuators A*, vol. 53, 1996, pp. 371-378.

[78] A.J. Ricco, “Acoustic wave viscosity sensor,” *Applied Physics Letters*, vol. 50, 1987, pp. 1474-6.

[79] A.J. Ricco, S.J. Martin, and G.C. Frye, “Acoustic plate mode devices as liquid phase sensors,” *1988 Solid State Sensor and Actuator Workshop. Technical Digest*, 1988, pp. 23-26.

[80] R. Schumacher, “The Quartz Microbalance: A Novel Approach to the In-Situ Investigation of Interfacial Phenomena at the Solid/Liquid Junction[New Analytical Methods(40)],” *Angewandte Chemie International Edition in English*, vol. 29, 1990, pp. 329-343.

[81] M.G. Schweyer, J.A. Hilton, J.E. Munson, J.C. Andle, J.M. Hammond, and R.M. Lec, “A novel monolithic piezoelectric sensor,” *1997 IEEE International Frequency Control Symposium*, Ieee, 1997, pp. 33-40.

[82] R. Thalhammer, S. Braun, B. Devcic-Kuhar, M. Groschl, F. Trampler, E. Benes, H. Nowotny, and P. Kostal, “Viscosity sensor utilizing a piezoelectric thickness shear sandwich resonator.,” *IEEE transactions on ultrasonics, ferroelectrics, and frequency control*, vol. 45, Jan. 1998, pp. 1331-40.

[83] C. Atkinson and M. Manriquedelara, “Fluid reaction on a vibrating disc in a viscous medium,” *International Journal of Engineering Science*, vol. 44, Sep. 2006, pp. 973-995.

[84] L.D. Landau and E.M. Liftshitz, *Fuid Mechanics*, London: Pergamom, 1959.

[85] S. Inaba, K. Akaishi, T. Mori, and K. Hane, “Analysis of the resonance characteristics of a cantilever vibrated photothermally in a liquid,” *Journal of Applied Physics*, vol. 73, 1993, pp. 2654-2659.

[86] A. Maali, C. Hurth, R. Boisgard, C. Jai, T. Cohen-Bouhacina, and J.-P. Aimé, “Hydrodynamics of oscillating atomic force microscopy cantilevers in viscous fluids,” *Journal of Applied Physics*, vol. 97, 2005, p. 074907.

[87] B. Boley and J. Weiner, “Theory of Thermal Stresses,” Malabar, Florida: Robert E. Kreiger Publishing Company, 1985, p. v.

[88] B. Boley and J. Weiner, “Theory of Thermal Stresses,” Malabar, Florida: Robert E. Kreiger Publishing Company, 1985, pp. 379-409.

[89] B. Boley and J. Weiner, “Theory of Thermal Stresses,” Malabar, Florida: Robert E. Kreiger Publishing Company, 1985, p. 339.

[90] B. Boley and J. Weiner, “Theory of Thermal Stresses,” Malabar, Florida: Robert E. Kreiger Publishing Company, 1985, p. 407.

[91] B. Boley and J. Weiner, "Theory of Thermal Stresses," Malabar, Florida: Robert E. Kreiger Publishing Company, 1985, p. 54.

[92] B. Boley and A.D. Barber, "Dynamic response of beams and plates to rapid heating," *Journal of Applied Mechanics*, vol. 24, 1957, pp. 413-416.

[93] H. Lamb, "On the vibrations of an elastic plate in contact with water," *Proceedings of the Royal Society of London. Series A, Containing Papers of a Mathematical and Physical Character*, vol. 98, 1920, p. 205–216.

[94] J.H. Powell and J.H.T. Roberts, "On the Frequency of Vibration of Circular Diaphragms," *1922 Proc. Phys. Soc. London*, vol. 35, 1923, pp. 170-182.

[95] Y. Kerboua, A.A. Lakis, M. Thomas, and L. Marcouiller, "Vibration analysis of rectangular plates coupled with fluid," *Applied Mathematical Modelling*, vol. 32, Dec. 2008, pp. 2570-2586.

[96] T.P. Chang and M.F. Liu, "On the Natural Frequency of a Rectangular Isotropic Plate in Contact With Fluid," *Journal of Sound and Vibration*, vol. 236, Sep. 2000, pp. 547-553.

[97] Q. Zou, U. Sridhar, and R. Lin, "A study on micromachined bimetallic actuation," *Sensors and Actuators A: Physical*, vol. 78, Dec. 1999, pp. 212-219.

[98] R. Puers, A. Cozma, and D.D. Bruyker, "On the mechanisms in thermally actuated composite diaphragms," *Sensors and Actuators: A. Physical*, vol. 67, 1998, pp. 13-17.

[99] R.J. Roark, *Roark's Formulas for Stress and Strain*, New York: McGraw-Hill, 2002.

[100] B. Boley and J. Weiner, "Theory of Thermal Stresses," Malabar, Florida: Robert E. Kreiger Publishing Company, 1985, pp. 432-445.

[101] R. Arya, M.M. Rashid, D. Howard, S.D. Collins, and R.L. Smith, "Thermally Actuated, bistable, oxide/silicon/metal membranes," *Journal of Micromechanics and Microengineering*, vol. 16, 2006, pp. 40-47.

[102] V. Djakov, E. Huq, and P. Vernon, "Fluid Probe," , 2008.

[103] N. Noda, R.B. Hetnarski, and Y. Tnaigawa, *Thermal Stresses*, New York: Taylor & Francis, 2003.

[104] K. Bongsang, C.M. Jha;, T. White;, R.N. Candler;, M. Hopcroft;, M. Agarwal;, K.K. Park;, R. Melamud;, S. Chandorkar;, and W. Kenny, "Temperature dependence of quality factor in MEMS resonators," *Micro Electro Mechanical*

Systems, 2006. MEMS 2006 Istanbul. 19th IEEE International Conference on, 2006, pp. 590 - 593.

[105] R.D. Blevins, *Formulas for Natural Frequency and Mode Shape*, New York: Van Nostrand Reinhold Company, 1979.

[106] K.E. Petersen, "Silicon as a mechanical material," *Proceedings of the IEEE*, vol. 70, 1982, pp. 420-457.

[107] J. Dolbow and M. Gosz, "Effect of out-of-plane properties of a polyimide film on the stress fields in microelectronic structures," *Mechanics of Materials*, vol. 23, Aug. 1996, p. 311–321.

[108] B. Bhushan and X. Li, "Micromechanical and tribological characterization of doped single-crystal silicon and polysilicon films for microelectromechanical systems devices," *Journal of Materials Research*, vol. 12, 1997, pp. 54-63.

[109] N.S. Al-Huniti and M.A. Al-Nimr, "Behavior of Thermal Stresses in a Rapidly Heated Thin Plate," *Journal of Thermal Stresses*, vol. 23, May. 2000, pp. 293-307.

[110] M.A. Hopcroft, "TEMPERATURE-STABILIZED SILICON RESONATORS FOR FREQUENCY REFERENCES," Stanford University, CA, 2007.

[111] V. Pradeep and N. Ganesan, "Thermal buckling and vibration behavior of multi-layer rectangular viscoelastic sandwich plates," *Journal of Sound and Vibration*, vol. 310, Feb. 2008, pp. 169-183.

[112] C. Bourgeois, E. Steinsland, N. Blanc, and N.D. Rooij, "Design of resonators for the determination of the temperature coefficients of elastic constants of monocrystalline silicon," *IEEE International Frequency Control Symposium*, 1997.

[113] K. Bongsang, R. Melamud, M. a Hopcroft, S. a Chandorkar, G. Bahl, M. Messana, R.N. Candler, G. Yama, and T. Kenny, "Si-SiO2 Composite MEMS Resonators in CMOS Compatible Wafer-scale Thin-Film Encapsulation," *2007 IEEE International Frequency Control Symposium Joint with the 21st European Frequency and Time Forum*, May. 2007, pp. 1214-1219.

[114] T. Mang and W. Dresel, *Lubricants and Lubrication*, Wiley-VCH; 2 edition (March 16, 2007), .

[115] S.M. Ali, S.C. Mantell, and E.K. Longmire, "Mechanical Performance of Microcantilevers in Liquids," *Microelectromechanical Systems, Journal of*, vol. 20, 2011, p. 441–450.

Appendix A

Thermal Resonators – May 2010
MEMS PROCESS FLOW
P+, Poly , Metal, Passivation

Step	Instructions	Review/Sign
1	Obtain qty 10, 4" n-type wafers	
2	Grind wafer to 300um 200rpm Confirm pressure for rate of about 25um/min	
3	CMP back side Slurry: pH=12, 15-20min per wafer Drip rate: 1drip/second Down Pressure: 8psi Quill speed: 70rpm Oscillation speed: 6 per min Table speed: 50Hz Front and back of wafer should look the same visually Clean wafers with soap and water to remove excess slurry before it dries.	
4	CMP Clean 5:1:1 H2O:H2O2:HCL, at 70 C for 20 min 10 min DI Water rinse	
5	RCA Clean 10 min SC1, 15:3:1 H20:H2O2:NH4OH 5 min DI water rinse 60 sec 50:1 HF 5 min DI water rinse 10 min SC2 15:3:1 H2O:H2O2:HCL 5 min DI water rinse SRD	
6	Grow P+ masking oxide 5000 Å, Recipe 353 Enter Nanospec thickness: 1_____, 2_____, 3_____, 4_____, 5_____	
7	Photo 1: P+ diffusion Coat in wafer track – recipe 1 (HMDS vapor prime, coat S1813 resist_4500rpm_60sec, softbake_90C_60sec) Expose using KS55 aligner with 14 sec exposure. Develop in wafer track – recipe 1 (peb_115C_60sec, develop_CD26_50sec,hard_bake_125C_60sec) Enter minimum resolution line:	

	_____ um **Alternate:** Hand coat with CEE spinner – Dehydration bake_120C_60sec, HMDS spin_4500rpm_60sec, coat S1813 resist_4500_rpm_60sec, softbake_90C_60sec) Expose using KS55 aligner with 14 sec exposure. Hand develop (peb_115C_60sec, develop_CD26_50sec, DI water rinse and air-gun dry, hard_bake_125C_60sec) Enter minimum resolution line: _____ um	
8	Etch Oxide ~7 min in 5.2:1 BOE, ER should be about 900Å/min DI water rinse SRD Verify thickness of oxide is <100Å in nanospec	
9	Strip Resist Branson asher, 4-inch standard recipe **Alternate:** 5 min solvent clean + 10 min DI water rinse + SRD	
10	Spin-on Glass Borofilm 100, include dummy 3000 rpm 30sec Blue oven bake at 200C for 20 minutes in air ambient	
11	Dopant Diffusion Recipe 110 Soak: 20min N2 at 1000C + 30min wetO2 at 1000C	
12	Etch SOG and Masking Oxide 20min (5.2:1) BOE Wafer should look clean, like bare Silicon. Nanospec <100Å	
13	Four Point Probe Dummy Wafer (manual or RESMAP) Rs should be around 100 ohm/sq Voltage= _____, Current=_____ Rs: _____ ohm/sq	
14	RCA Clean 10 min SC1, 15:3:1 H20:H2O2:NH4OH 5 min DI water rinse 60 sec 50:1 HF 5 min DI water rinse	

	10 min SC2 15:3:1 H2O:H2O2:HCL 5 min DI water rinse SRD	
15	Grow 500 Å pad oxide, Recipe 250 Soak: 54min dryO2 at 1000C Enter Nanospec thickness: 1_____, 2_____, 3_____, 4_____, 5_____	
16	Deposit 1500 Å Nitride LPCVD 810C Factory Nitride recipe Soak time from log sheet= _____ Enter Nanospec thickness: 1_____, 2_____, 3_____, 4_____, 5_____	
17	Coat back of wafer by hand and protect edge	
18	Plasma Etch Nitride on front of wafer, Lam-490 Use FACNITRIDE recipe, endpoint detection may not work due to smaller 4" wafer area. (Expect ~2'30'') Etch through nitride and stop on SiO2. Time/wafer = _____	
19	Strip Resist Hard Ash or solvent strip	
20	Wet etch of pad oxide, Rinse, SRD (10:1 BOE 2 minutes)	
21	RCA Clean 10 min SC1, 15:3:1 H20:H2O2:NH4OH 5 min DI water rinse 60 sec 50:1 HF 5 min DI water rinse 10 min SC2 15:3:1 H2O:H2O2:HCL 5 min DI water rinse SRD	
22	Grow 5000Å oxide recipe 353 Enter Nanospec thickness: 1_____, 2_____, 3_____, 4_____, 5_____	
23	Photo 2: for backside diaphragm See http://people.rit.edu/lffeee/backside alignment.pdf	

24	Spin coat Resist on front side of wafer and protect edge Use CEE coater, S1813 resist, recipe 0 Bake at 130C for 1 min with pins to protect backside pattern	
25	Etch oxynitride off backside, 1 min in 10:1 BOE	
26	Plasma Etch Nitride on back of wafer, Lam-490 Use FACNITRIDE recipe, endpoint detection may not work due to smaller 4" wafer area. (Expect ~2'45'') Etch through nitride and SiO2. Silicon should look cloudy/rough. Time/wafer = _____	
27	Wet etch of pad oxide if still remains, Rinse, SRD 1.5 min 10:1 BOE	
28	Remove resist Solvent strip 5min+5min rinse	
29	RCA Clean 10 min SC1, 15:3:1 H20:H2O2:NH4OH 5 min DI water rinse 60 sec 50:1 HF 5 min DI water rinse 10 min SC2 15:3:1 H2O:H2O2:HCL 5 min DI water rinse SRD	
30	Deposit 6000 Å poly LPCVD Use 610C Poly recipe Soak time from log sheet= _____ Enter Nanospec thickness: 1_____, 2_____, 3_____, 4_____, 5_____	
31	Spin on Glass, N-250 3000 rpm 30sec Blue oven bake at 200C for 20 minutes in air ambient	
32	Poly Diffusion, Recipe 120 15 min in N2 at 1000C	
33	Etch SOG 7 min 5.2:1 BOE	
34	4 pt Probe on edge of wafer with manual 4pt probe Voltage= _____, Current=_____ Rs= _____ ohm/sq	
35	Photo 3, Poly	

	Coat in wafer track – recipe 1 (HMDS vapor prime, coat S1813 resist_4500rpm_60sec, softbake_90C_60sec) Expose using KS55 aligner with 14 sec exposure. Develop in wafer track – recipe 1 (peb_115C_60sec, develop_CD26_50sec,hard_bake_125C_60sec) Enter minimum resolution line: _____ um **Alternate:** Hand coat with CEE spinner – Dehydration bake_120C_60sec, HMDS spin_4500rpm_60sec, coat S1813 resist_4500_rpm_60sec, softbake_90C_60sec) Expose using KS55 aligner with 14 sec exposure. Hand develop (peb_115C_60sec, develop_CD26_50sec, DI water rinse and air-gun dry, hard_bake_125C_60sec) Enter minimum resolution line: _____ um	
36	Etch poly, LAM490 Use FACPOLY? recipe, endpoint detection may not work due to smaller 4” wafer area. (Expect ~1’05’’) Time/wafer = _____	
37	Strip Resist 5 min solvent clean + 10 min DI water rinse + SRD	
38	RCA Clean 10 min SC1, 15:3:1 H20:H2O2:NH4OH 5 min DI water rinse 60 sec 50:1 HF 5 min DI water rinse 10 min SC2 15:3:1 H2O:H2O2:HCL 5 min DI water rinse SRD	
39	Oxidize Poly Recipe 250 Soak: 54min dryO2 at 1000C Enter Nanospec thickness: 1_____, 2_____, 3_____, 4_____, 5_____	

40	Deposit 1μm LTO LPCVD 410C LTO, include bare-Si dummy wafer Soak time from log sheet= _____ Enter Nanospec thickness of bare-Si dummy wafer: 1_____, 2_____, 3_____, 4_____, 5_____	
41	Photo 4, Contact Cut Coat in wafer track – recipe 1 (HMDS vapor prime, coat S1813 resist_4500rpm_60sec, softbake_90C_60sec) Expose using KS55 aligner with 14 sec exposure. Develop in wafer track – recipe 1 (peb_115C_60sec, develop_CD26_50sec,hard_bake_125C_60sec) Enter minimum resolution line: _____ um **Alternate:** Hand coat with CEE spinner – Dehydration bake_120C_60sec, HMDS spin_4500rpm_60sec, coat S1813 resist_4500_rpm_60sec, softbake_90C_60sec) Expose using KS55 aligner with 14 sec exposure. Hand develop (peb_115C_60sec, develop_CD26_50sec, DI water rinse and air-gun dry, hard_bake_125C_60sec) Enter minimum resolution line: _____ um	
42	Etch Contact Cut in BOE, Rinse, SRD 5.2:1 BOE, determine etch time based on LTO thickens. Etch rate is ~2000Å/min???? Enter etch time: _____ min Enter approximate delta CD after etch. ____ um	
43	Strip Resist 5 min solvent clean + 5 min DI water rinse + SRD	
44	RCA Clean, include extra HF 10 min SC1, 15:3:1 H20:H2O2:NH4OH 5 min DI water rinse 60 sec 50:1 HF 5 min DI water rinse 10 min SC2 15:3:1 H2O:H2O2:HCL 5 min DI water rinse 20 sec 50:1 HF 5 min DI water rinse SRD	

45	Deposit Aluminum, 10,000Å Al/Si 8" target, 2000 Watts, Argon, 5 mTorr dep pressure Dep time from logsheets: _____ min (33min in 20062) Use dummy wafer with tape to measure step height. Alpha-step Al thickness = _____ Å	
46	Photo 5, Metal Coat in wafer track – recipe 1 (HMDS vapor prime, coat S1813 resist_4500rpm_60sec, softbake_90C_60sec) Expose using KS55 aligner with 9 sec exposure Develop in wafer track – recipe 1 (peb_115C_60sec, develop_CD26_50sec,hard_bake_125C_60sec) Enter minimum resolution line: _____ um **Alternate:** Hand coat with CEE spinner – Dehydration bake_120C_60sec, HMDS spin_4500rpm_60sec, coat S1813 resist_4500_rpm_60sec, softbake_90C_60sec) Expose using KS55 aligner with 9 sec exposure Hand develop (peb_115C_60sec, develop_CD26_50sec, DI water rinse and air-gun dry, hard_bake_125C_60sec) Enter minimum resolution line: _____ um	
47	Etch Aluminum, Wet Etch Use agitation or dunking technique to ensure that Al etches in smaller spaces. Time should be 4-5 minutes. Run one wafer first and inspect carefully, then the rest of wafers.	
48	Strip Resist 5 min solvent clean + 10 min DI water rinse + SRD	
49	Deposit 1µm LTO – Passivation LPCVD 410C LTO, include bare-Si dummy wafer Soak time from log sheet= _____ Enter Nanospec thickness of bare-Si dummy wafer: 1_____, 2_____, 3_____, 4_____, 5_____	

50	Photo 6, Passivation Via Coat in wafer track – recipe 1 (HMDS vapor prime, coat S1813 resist_4500rpm_60sec, softbake_90C_60sec) Expose using KS55 aligner with 9 sec exposure Develop in wafer track – recipe 1 (peb_115C_60sec, develop_CD26_50sec,hard_bake_125C_60sec) Enter minimum resolution line: _____ um **Alternate:** Hand coat with CEE spinner – Dehydration bake_120C_60sec, HMDS spin_4500rpm_60sec, coat S1813 resist_4500_rpm_60sec, softbake_90C_60sec) Expose using KS55 aligner with 9 sec exposure Hand develop (peb_115C_60sec, develop_CD26_50sec, DI water rinse and air-gun dry, hard_bake_125C_60sec) Enter minimum resolution line: _____ um	
51	Etch LTO-Passivation 1um in Pad Etch, Rinse, SRD Pad ETCH, determine etch time based on LTO thickens. Etch rate is ~2300Å/min???? Enter etch time: _____ min	
52	Strip Resist 5 min solvent clean + 10 min DI water rinse + SRD	
53	Spin Coat PROTEK on front of wafer – See Spec Sheet Primer 1500rpm, 30sec Hot plate 140C, 30sec Coat 1500rpm, 60sec HP 140C, 120sec Oven 200C, 30min	
54	Etch Diaphragm in KOH Measure etch rate ~1.2um/min in 20062 For 270um → 225min (<4hours)	
55	Strip PROTEK	

	Clean	
56	Test	

Appendix B

Response Fo

Actual by Predicted Plot

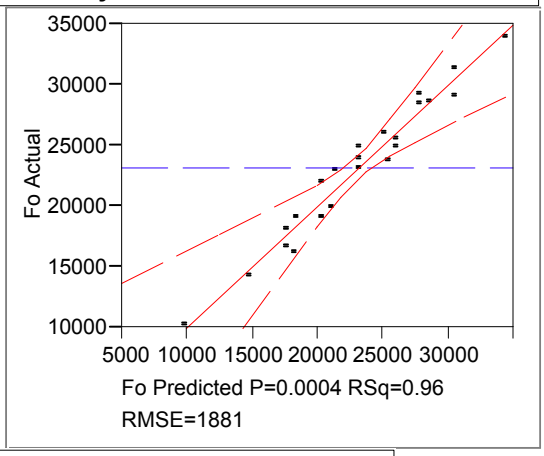

Summary of Fit

RSquare	0.961913
RSquare Adj	0.89526
Root Mean Square Error	1881.025
Mean of Response	23132.43
Observations (or Sum Wgts)	23

Effect Tests

Source	Nparm	DF	Sum of Squares	F Ratio	Prob > F
Heater	1	1	861	0.0002	0.9879
Rsize	2	2	18545291	2.6207	0.1332
Heater*Rsize	2	2	9055154	1.2796	0.3295
Pass	1	1	41079896	11.6102	0.0093
Heater*Pass	1	1	8095771	2.2881	0.1688
Rsize*Pass	2	2	9326623	1.3180	0.3201
Metal	1	1	8177782	2.3112	0.1669
Heater*Metal	1	1	124465377	35.1770	0.0003
Rsize*Metal	2	2	86958137	12.2883	0.0036
Pass*Metal	1	1	47867	0.0135	0.9103

Response Fo

Prediction Profiler

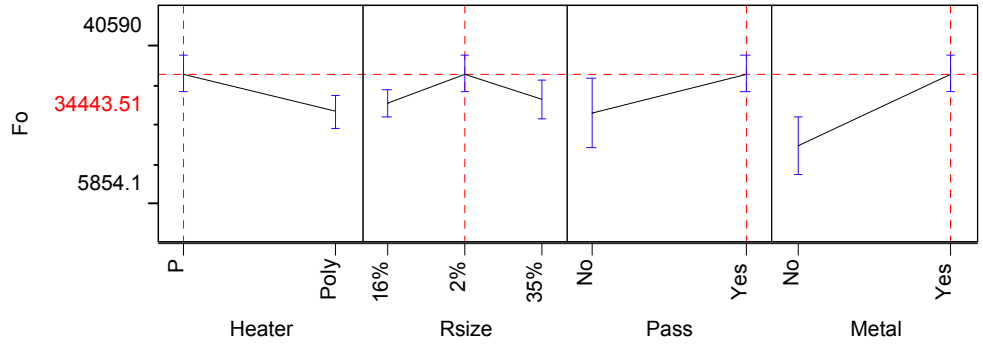

Response Norm Amp

Actual by Predicted Plot

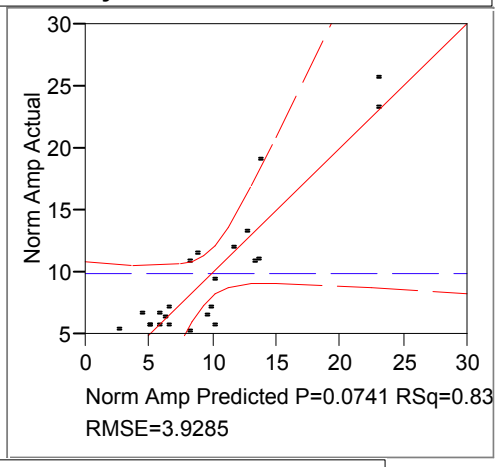

Summary of Fit

RSquare	0.830063
RSquare Adj	0.532672
Root Mean Square Error	3.928483
Mean of Response	9.881739
Observations (or Sum Wgts)	23

Effect Tests

Source	Nparm	DF	Sum of Squares	F Ratio	Prob > F
Heater	1	1	102.21052	6.6229	0.0329
Rsize	2	2	26.03358	0.8434	0.4652
Heater*Rsize	2	2	33.63111	1.0896	0.3815
Pass	1	1	4.86048	0.3149	0.5900
Heater*Pass	1	1	12.23338	0.7927	0.3993
Rsize*Pass	2	2	77.06566	2.4968	0.1437
Metal	1	1	0.46375	0.0300	0.8667
Heater*Metal	1	1	11.00363	0.7130	0.4230
Rsize*Metal	2	2	6.53810	0.2118	0.8135
Pass*Metal	1	1	2.33670	0.1514	0.7073

Response Norm Amp

Prediction Profiler

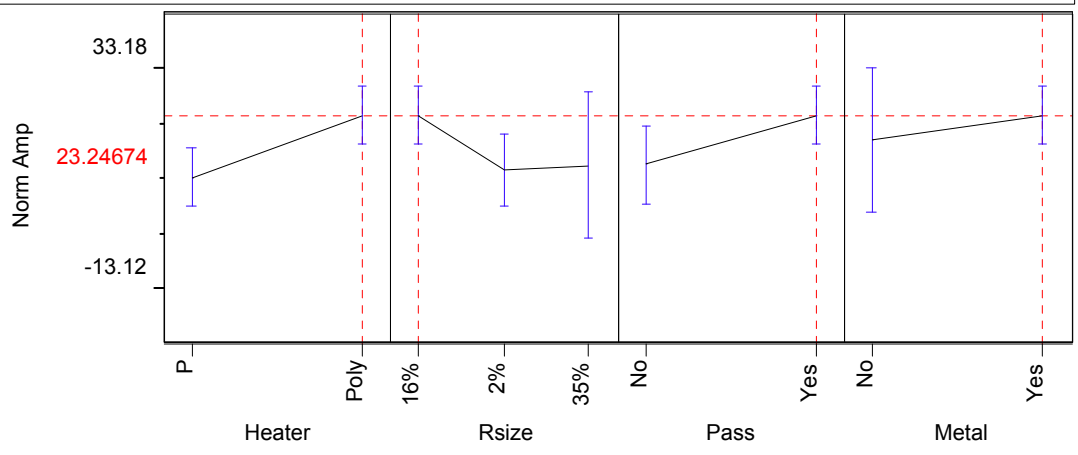

Response Norm Q

Actual by Predicted Plot

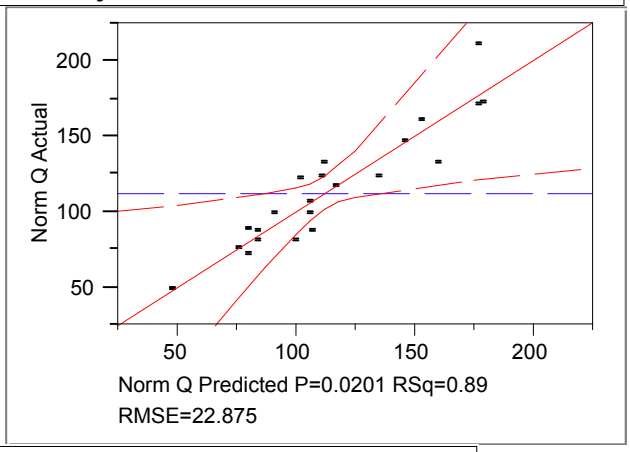

Summary of Fit

RSquare	0.88609
RSquare Adj	0.686746
Root Mean Square Error	22.87538
Mean of Response	112.6435
Observations (or Sum Wgts)	23

Effect Tests

Source	Nparm	DF	Sum of Squares	F Ratio	Prob > F
Heater	1	1	213.3631	0.4077	0.5410
Rsize	2	2	4967.9779	4.7469	0.0437
Heater*Rsize	2	2	631.0050	0.6029	0.5703
Pass	1	1	39.2410	0.0750	0.7911
Heater*Pass	1	1	3506.9250	6.7018	0.0322
Rsize*Pass	2	2	968.1196	0.9250	0.4351
Metal	1	1	2098.1711	4.0096	0.0802
Heater*Metal	1	1	747.5683	1.4286	0.2662
Rsize*Metal	2	2	1437.4981	1.3735	0.3070
Pass*Metal	1	1	3902.9588	7.4586	0.0258

Response Norm Q

Prediction Profiler

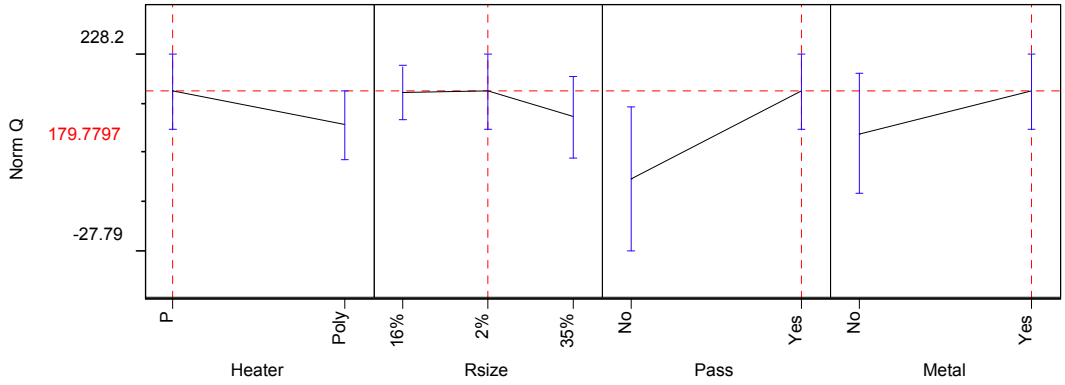

Least Squares Fit

Prediction Profiler